12-2016

Vanadium Diselenide: On the Verge of Charge Density Wave

Menghan Zhou
Clemson University

VANADIUM DISELENIDE: ON THE VERGE OF CHARGE DENSITY WAVE

A Dissertation
Presented to
the Graduate School of
Clemson University

In Partial Fulfillment
of the Requirements for the Degree
Doctor of Philosophy
General Physics

---

by
Menghan Zhou
Dec 2016

Accepted by:
Dr. Jian He, Committee Chair
Dr. Feng Ding
Dr. Donald Liebenberg
Dr. Terry M. Tritt

Abstract

Charge density wave (CDW) is a many-body state of matter in which both lattice and electron density are modulated by a new periodicity. CDW features discrete translational symmetry breaking, and mostly occurs in low-dimensional materials. Although CDW behaviors have been found in many materials, the underlying mechanism and the driving forces of CDW transition are still unclear. In particular, the origin of CDW in two-dimensional materials, especially in layered transition metal dicalchogenides (TMDCs), may be distinct from that in one-dimensional materials.

In this dissertation, the CDW transition in VSe_2, a layered TMDC material, is explored. Density functional theory (DFT) calculations were performed on bulk VSe_2, and the calculated results of spin-polarized band structure, density of states (DOS) and Fermi surface, along with phonon dispersion relation and phonon DOS are presented. Experimentally, both single- and poly-crystalline VSe_2 samples were investigated by means of electrical resistivity, Seebeck coefficient, Hall coefficient/Hall angle, magnetic susceptibility, heat capacity and thermal conductivity measurements. The anomalies of these physical properties across CDW transition temperature are studied and discussed. The experimental results indicate that the CDW in VSe_2 is weak, and only a small portion of Fermi surface is gapped during the transition. The comparison with three other CDW materials sheds light on the different origins of CDW formation in TMDCs.

Additionally, anomalies are found at very low temperatures in the heat capacity and electrical resistivity measurements of both single- and poly-crystalline VSe_2. The anomaly in heat capacity is presumably due to Schottky heat capacity caused by the nuclear spin of V atoms.

Acknowledgments

First of all, I would like to thank my advisor and friend, Dr. Jian He. He is such a passionate, energetic and knowledgeable person that is so enjoyable to work with, and I think everyone who ever has the opportunity of working with him would agree with me. Through these years, I have been enlightened for so many times by his comprehensive knowledge and wisdom, not only in physics, but also in history and life. I would also like to thank him for giving me this project. This work could not been done without his instructions and encouragement. As the tradition of He group, a graduate student needs to complete 6-10 projects before working on a new topic towards his/her Ph.D in 2 years. This dissertation is the outcome of my primary research project in the past sixteen months.

Second, I am also very grateful for the valuable time, help and guidance from other committee members: Dr. Tritt, Dr. Liebenberg and Dr. Ding. Dr. Tritt, thank you for generously letting me use your apparatuses, teaching me solid state physics, bring me to conferences and inviting me to your Christmas parties. Dr. Liebenberg, thank you for providing me valuable comments and advice on my dissertation, and being so kind and nice to me all these years.

I'm also very grateful for the helps from all the co-workers involved in this work. I want to express my gratitude to Mr. Yufei Liu, for his help on all aspects. I would also like to thank Mr.Dongwang Yang and Dr. Xinfeng Tang at Wuhan University of Technology for measuring the high resolution X-ray powder diffraction, Hall coefficient and low temperature heat capacity on my samples. Thanks go to Dr. Tsu-Lien Hung, Dr. Yang-Yuan Chen and Dr. Pai-Chun Wei at Institute of Physics, Academia Sinica for measuring the heat capacity at temperatures down to 0.3K. Thanks also go to Fanchen Meng for the density functional theory calculations in this work; Dr. Colin McMillen for the single crystal X-ray diffraction measurements; Ms. Jingyi Zhu for the Raman spectrum measurements; Dr. Xiaoyu Zeng and Mr. Chongze Hu for their valuable suggestions and

assistance in this project.

Last but not the least, I want to thank all the colleagues and friends that I have opportunities to meet at Clemson University. Many of them are current and former students in Dr. He and Dr. Tritt groups: Sriparna Bhattacharya, Dr. Dale Hitchcock, Dr. Song Zhu and his wife Meilan Zheng, Dr. Pooja Puneet, Dr. Jennifer Graff, Dr. Arash Mehdizadeh Dehkordi, Dr. Tim Holgate, Dr. Wenjie Xie, Ms. Yamei Liu, Mr. Gezhou Zhang, Ms. Yamin Liu, Dr. Tianwei Wang and his wife Ms. Shasha Wang, Dr. Tianhong Yu, Dr. Yang Gao and his wife Ms. Weiwei Wang, Dr. Lin Li and his wife Ms. Dan Du, Mr. Yunhui Peng and Dr. Keqin Yang. My memorials at Clemson could not be so pleasant without them.

This research is funded by National Science Foundation of the United States (DMR-1307740).

Table of Contents

List of Tables

List of Figures

Chapter 1

Introduction

At the core of condensed matter physics is the exchange of energy and (both linear and angular) momentum quanta between the charge, lattice, spin and orbital degrees of freedom in the spatial and temporal domain. In particular, electron is the fundamental particle of utmost importance for condensed matter physics. The interplay among electrons and the interplay between electrons and other quantum particles (quasi-particles) give rise to a wide variety of exotic behaviors, such as charge density waves (CDW) [1–4], spin density waves [5, 6], the Kondo effect [7], superconductivity [8–12], polarons [13, 14], and polaritons [15–17]. This dissertation will be focused on the study of CDW, which is generally a ground state of material that consists of a periodic charge density modulation as well as a periodic lattice distortion (PLD) [18].

CDW, along with many collective many-body quantum states, can be regarded as a result of spontaneous symmetry breaking. For instance, liquid to solid phase transition involves infinitesimal translational symmetry breaking; ferromagnets break rotational symmetry; and the superfluidity as well as superconductivity are related with the U(1) symmetry breaking. CDW is no different, where original discrete translational symmetry is broken with the formation of superstructures. In this dissertation, the CDW transition in a layered transition metal dichacogenides (TMDCs) material, VSe_2, is studied. Firstly, in this chapter, the concept and origin of CDW will be briefly introduced.

1.1 The Peierls Transition and the Kohn Anomaly

The origin of CDW is still controversial and under debate. Nevertheless, the concept itself originates from R. Peierls' prediction [19] of the instability in the electronic ground state of an ideal one-dimensional (1-D) metallic chain, namely the Peierls instability. Peierls pointed out that, a 1-D linear chain of atoms with periodic atomic spacing a is unstable at low temperatures, and will undergo a lattice distortion. The resulted new periodicity ra then creates energy gaps in the electronic band structure at the wavevectors $k = \frac{\rho\pi}{ra}$, which is analog to the energy gaps at Brillouin zone boundaries. Here $\rho = \pm 1, \pm 2, ..., \pm(r-1)$ and r is an arbitrary positive number, and could be either non-integers (for incommensurate CDW) or integers (for commensurate CDW). Fig. 1.1 illustrates the atom chain and electronic band structure before and after the distortion. The average of the energies across the idstortion induced gap is still the same as the original. Therefore, only in the case that the band below the gap is filled and above the gap is empty, there will be a net reduction in the total energy. This condition is satisfied in electronic band structure of metals, in which the band across the Fermi wave vector $\mathbf{k}_F$ is always filled with electrons on the side with lower energy while empty on the other. Thus, the metallic state of an ideal 1-D metal chain is unstable, and a ground state with opened gap at $\mathbf{k}_F$ is energetically preferred. Consequently, there will be a PLD, and the new period is $\lambda = 2\pi/2k_F = \pi/k_F$.

Independently, H. Fröhlich [3] suggested that in the 1-D model, interactions between free electrons and lattice displacement can lead to periodic lattice displacement (of wavevector $2\mathbf{k}_F$), which further gives rise to the periodic fluctuation in the electronic density with the same period. Additionally, at non-zero temperature, the lattice distortion and magnitude of the gap will be reduced by the electron excitations across the gap [3, 20]. The electron excitions eventually lead to the (Peierls) transition temprature T_{CDW}, across which the material will experience a transition from the high temperature normal state to the low temperatures semiconductor/insulator ground state [1] with temperature dependent energy gap.

The CDW state is stable only when the energy reduction in the electron subsystem (due to the reformation of band structure) overwhelms the potential increase in the lattice strain (due to the lattice distortion). Here the energy gain due to band reformation δE_{band} is proportional to the non-interacting electronic susceptibility $\chi(\mathbf{q})$, as $\delta E_{band} \propto -\chi(\mathbf{q})$, where the negative sign here is only an indication of energy reduction. The electronic susceptibility, also called Lindhard response

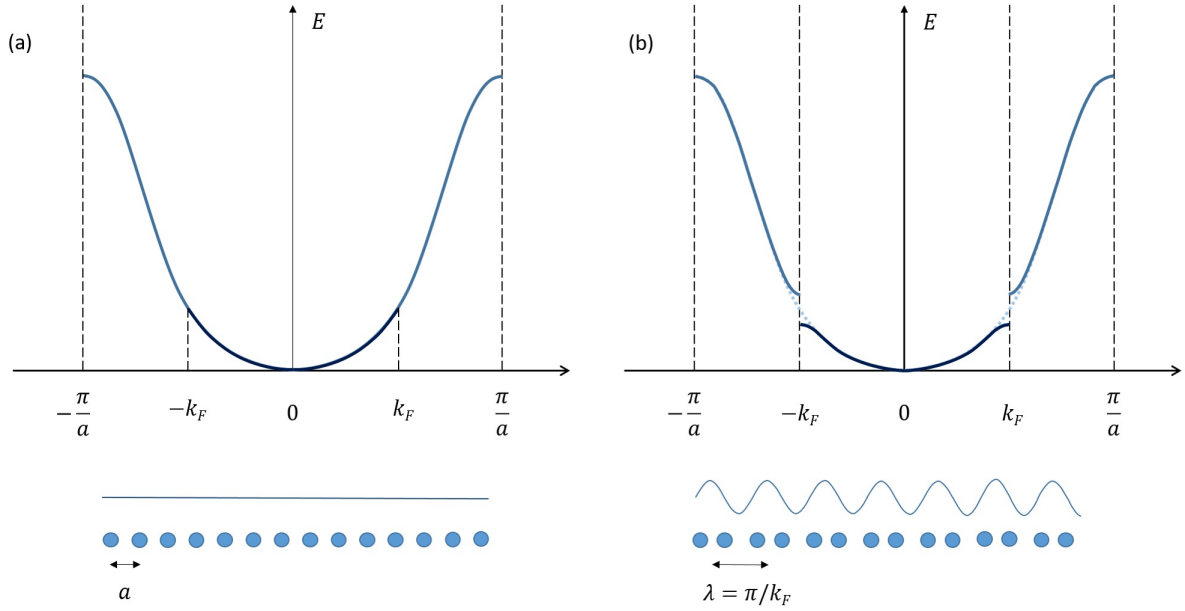

Figure 1.1: A 1-D system, in (a) normal state, and (b) CDW state. The lattice of the material distorts and the modulation has a wavelength of π/k_F and thus leads to an energy gap at the Fermi surface $\mathbf{k} = \pm\mathbf{k}_F$.

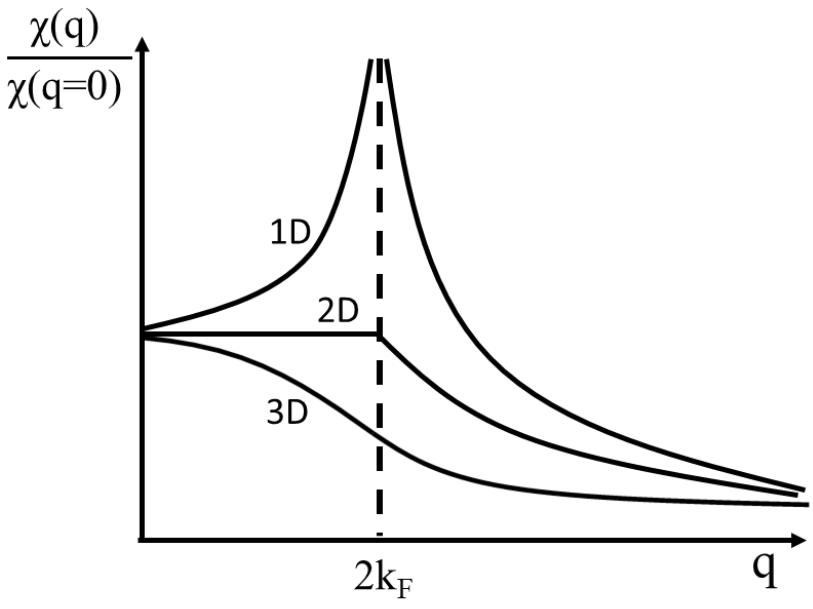

Figure 1.2: Electronic susceptibility for 1-D, 2-D and 3-D systems.

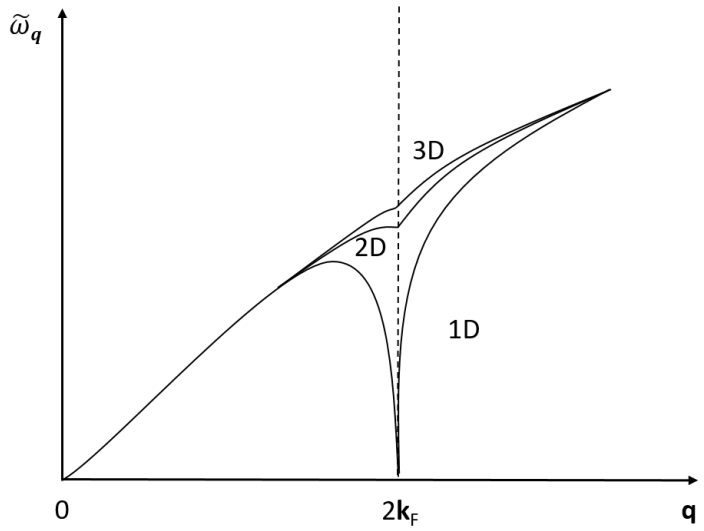

Figure 1.3: Kohn anomaly in the acoustic phonon branch in 1-D, 2-D and 3-D systems.

function or Lindhard susceptibility, is the parameter that relates the time independent potential $\phi(\mathbf{q})$ to the rearrangement of the charge density $\rho(\mathbf{q})$, as $\rho(\mathbf{q}) = \chi(\mathbf{q})\phi(\mathbf{q})$. The electronic susceptibility is defined as

$$\chi(\mathbf{q}) = \int \frac{d\mathbf{k}}{2\pi^d} \frac{f_{\mathbf{k}} - f_{\mathbf{k+q}}}{\varepsilon_{\mathbf{k}} - \varepsilon_{\mathbf{k+q}}},$$

where $\epsilon_{\mathbf{k}}$, $\epsilon_{\mathbf{k+q}}$ and $f_{\mathbf{k}}$, $f_{\mathbf{k+q}}$ denote the energy and Fermi distribution function at wavevectors $\mathbf{k}$ and $\mathbf{k}+\mathbf{q}$, respectively. d is the dimensionality of the system.

Mathmatically, the stability condition can be expressed as $\delta E_{band} + \delta E_{lattice} < 0$. Considering the effects of Coulomb interaction and the Screened exchange interaction, this inequality can be modified as $\delta E_{band} + \delta E_{lattice} - 2U_{\mathbf{q}} + V_{\mathbf{q}} \leq 0$, and eventually further written as [21, 22]:

$$\frac{4{g_{\mathbf{q}}}^2}{\hbar\omega_{\mathbf{q}}} - 2U_{\mathbf{q}} + V_{\mathbf{q}} \geq \frac{1}{\chi(\mathbf{q})}.$$

Here $-2U_{\mathbf{q}}$ and $V_{\mathbf{q}}$ are the energy changes considering direct Coulomb interaction and screened exchange interaction, $g_{\mathbf{q}}$ denotes a constant associated with electron-phonon coupling, and $\omega_{\mathbf{q}}$ is the phonon frequency at state $\mathbf{q}$.

From the CDW stability condition given above, it is clear that both a large electron-phonon interaction constant $g_{\mathbf{q}}$, and/or a large electronic susceptibility $\chi(\mathbf{q})$ favor the occurence of CDW [22]. The electronic susceptibility is sensitive to the dimensionality d and the electron states in the vicin-

ity of Fermi level. Fig. 1.2 shows electronic susceptibility as a function of wavevector in different dimensionality [18]: In 1-D systems, it diverges at $\mathbf{q} = 2\mathbf{k}_F$; in two-dimensional (2-D) systems, it yields a step function; and for three-dimensional (3-D) systems, the function is smooth and continuous across $2\mathbf{k}_F$. In 1-D systems, the divergence of χ at $\mathbf{q} = 2\mathbf{k}_F$ would make $\frac{1}{\chi(\mathbf{q})} = 0$, ensuring the stability of CDW state. However, for 2-D materials, the peak at $2\mathbf{k}_F$ is not as pronounced as in the 1-D case. Therefore, one would expect the CDW formation in quasi-1-D materials to be easier to understand, while in 2-D CDW materials (CDWs), the underlying mechanisms will be more subtle.

Another major difference between 1-D and 2-D CDWs is the so-called Kohn anomaly effect. Pointed out by W. Kohn in 1959 [23], the divergence of χ in 1-D CDW will not only affect the distribution of charge density, but also affect phonon dispersion relation. A peak in χ at $2\mathbf{k}_F$ will consequently soften the phonon modes at the same wavevector, with the form of

$$\tilde{\omega}_{\mathbf{q}}^2 = {\omega_{\mathbf{q}}}^2 \left(1 - \frac{4{g_{\mathbf{q}}}^2}{\hbar\omega_{\mathbf{q}}}\chi\left(\mathbf{q}\right)\right).$$

It can be seen that as χ goes to infinity at $2\mathbf{k}_F$ in 1-D CDWs, the renormalized phonon frequency $\widetilde{\omega}_{\mathbf{q}}$ of phonon mode $2\mathbf{k}_F$ will drop to zero. However, for 2-D CDWs, as χ never reaches infinity, the phonon softening effect is much weaker. Fig. 1.3 shows the Kohn anomaly in systems with different dimensionality [18].

Hence, it seems that the CDW in 2-D materials is not as simple as its 1-D counterpart. In fact, the origin of CDW formation in 2-D systems is still controversial. Several models have been proposed, including Fermi surface nesting, saddle point model, electron-phonon coupling, and excitonic condensation. In section 1.3, these models will be briefly introduced. Before that, an interesting property of CDW, namely the CDW sliding, will be discussed in section 1.2.

1.2 Charge Density Wave (CDW) Sliding

The response of CDW state to an external DC electric field is different from conventional conductors. It is useful to adopt classical particle model to describe the behavior of density waves in CDW.

As the lattice distorts in CDW, it forms potential gaps that can be treated as impurities, those impurities would result in the pinning effect to the charge densities, i.e., the charge is difficult

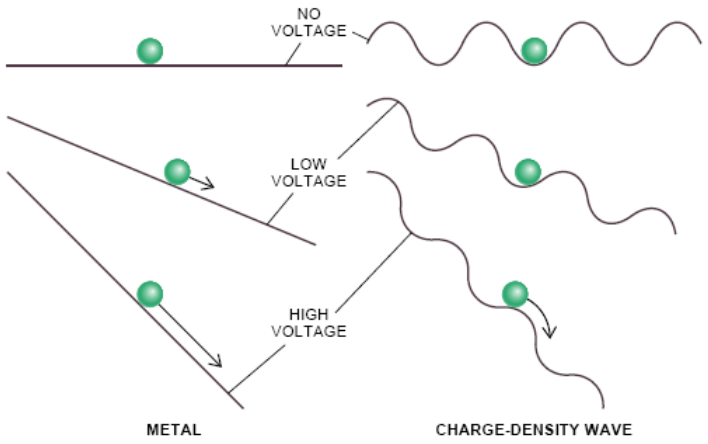

Figure 1.4: Comparision between charge particle model in normal metal and in the CDW state. The left figures illustrate the response of charge to electric field in a metal, while the right figures show the response in CDW state [24].

to move under an external electric field. The applied electric field tilts the potential, and for normal metals and CDWs, the effects are different.

Fig. 1.4 illustrates the effect of external DC electric field on a metal and a CDW material. For normal metal state, the electrical potential is flat, and the slope is proportional to the strength of applied field. Thus the resulting current increases linearly with the electric field. For CDWs, the potential is periodic, thus it requires an electric field that can overcome the potential barrier to generate the current. And moreover, the current is not linear with the increase in electric field, as depicited in Fig. 1.5. This non-linear conductivity is also known as the Fröhlich conductivity [25].

One notable feature of the sliding CDW is the broadband and narrow-band noise. It was first found in $NbSe_3$, which is a quasi-1-D CDW material, by Fleming and Grimes [26]. With an electric field higher than the threshold field strength, an abrupt increase in noise occurs. This phenomenon has been suggested to arise from turbulent motion of CDW, moving soliton lattice, or a drifting CDW [27], but no consensus has been reached. For instance, in 1988, Tritt et al. found that the narrow-band noise in $NbSe_3$ exists only in certain regions of magnetic-field strength, and it was suggested to at least partially due to the motion of the CDW instead of due to an increase in the carrier concentration [28].

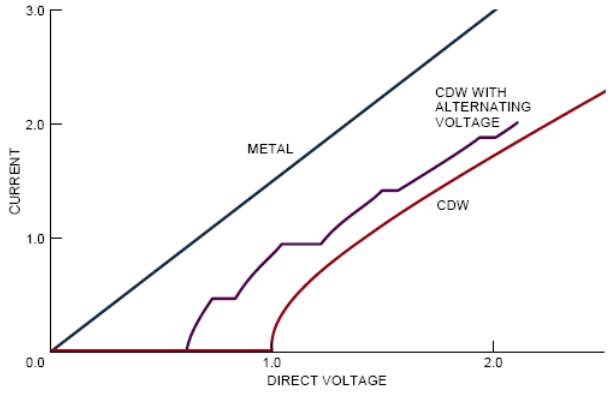

Figure 1.5: Current vs. Voltage curves of normal metal and CDW material. For metals, the current is proportional to applied voltage. For CDWs, there is no current until the voltage reaches a critical value, and the current vs. voltage is non-linear. The purple curve shows the behavior of current in CDW state when the applied external voltage is DC+AC field. The plateaus occurs when the density waves of CDW matches the AC frequency [24].

1.3 Controversies over the origin of CDW

In section 1.1, the theoretical model of CDW based on Peierls instability has been discussed. However, there has been controversies over the origin of CDW formation.

A classic explanation is that CDW is the result of the Fermi surface nesting. As discussed in section 1.1, CDW state is stable when χ is very large at a specific wave vector. In order to have a large χ, one needs a large numerator, a small denominator, and many such q-coupled states [22]. For a 1-D metal in 3-D space, this can be easily satisfied due to the fact that its Fermi surfaces are planar, and are parallel to each other and separated by a definite wave vector. Such a topology of Fermi surface is called Fermi surface nesting. But for 2-D materials, if there is no electron-electron and electron-phonon interactions, the Fermi surface is a circle, thus no nested surfaces could be found, and the divergence of χ at $2\mathbf{k}_F$ is non-existent. Therefore, one possible way to have CDW in 2-D systems is to distort its Fermi surface to mimic the 1-D planar topology, that is, to have two segments of Fermi surfaces that are parallel to each other and separated by a wave vector $\mathbf{q}$. Fig. 1.6 shows the Fermi surface nesting in 1-D, 2-D and distorted 2-D materials.

Indeed, Fermi surface nesting provides a good interpretation of the CDWs in quasi-1-D materials [18], and also works for some quasi-2-D solids such as layered rare earth tritellurides [29,30]. However, the model was found not able to well explain the CDW in many 2-D CDWs, especially in some TMDCs. Two notable examples are 2H-$TaSe_2$ and 2H-$NbSe_2$. Inosov et al. [31] report that for

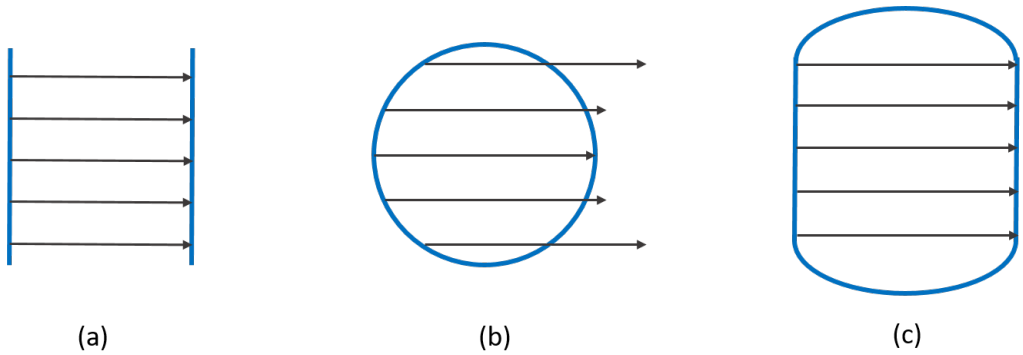

Figure 1.6: Schematic Fermi surface nesting of (a) 1-D system (b) 2-D system without nesting (c) 2-D with nesting due to Fermi surface distortion.

these two materials, although Fermi surface nesting was found in the spectra of high-resolution angle-resolved photoelectron spectroscopy (ARPES), the nesting vector and the CDW ordering vector do not exactly coincide [31]. Moreover, the calculations done by Johannes et al. [32] suggest that Fermi surface nesting contributes nothing to CDW instability in $NbSe_2$, and the main contribution comes from an energy range not near E_F. Moreover, Johannes et al. [33] demonstrates that even though the Fermi surface nesting in 1-D and 2-D (Fig. 1.6 (a)(c)) can lead to a logarithmic divergence in χ, the instability can be easily destroyed by a small deviation from perfect nesting conditions. Thus they argues that there is only a tiny fraction, if any, of the CDW phases that is true analogs of the Peierls instability.

Here the 2H-$NbSe_2$ is taken as an example to demonstrate that the conventional Fermi surface nesting picture is less likely to be the only cause of CDW in the material. Fig. 1.7 shows both experimental and theoretical evidences. In Fig. 1.7(a) [34, 35], it can be clearly seen that the $\mathbf{q}_{CDW}$ observed in 2H-$NbSe_2$ by neutron scattering does not correspond to any nested Fermi surface, although there are parts of Fermi surface nested. Panel (b) and (c) [32] illustrate the imaginary and real part of the electronic susceptibility $\chi(\mathbf{q})$ in 2H-$NbSe_2$. Again, there is no peak found at $\mathbf{q}_{CDW}$ in the $\chi(\mathbf{q})$ plot, indicating that the Fermi surface nesting description, i.e., $\chi(\mathbf{q}_{CDW})$ enhanced from Fermi surface nesting stabilizes CDW state, may not be valid in 2H-$NbSe_2$.

Therefore, Fermi surface nesting by itself is no longer valid in some, especially layered TMD CDWs, such as 2H-$NbSe_2$. Several models then have been proposed, including saddle point/van Hove singularity model, strong electorn-phonon coupling, and excitonic condensation model, etc.

Saddle point model was first proposed by Rice and Scott in 1975 [36]. In 2-D systems, the

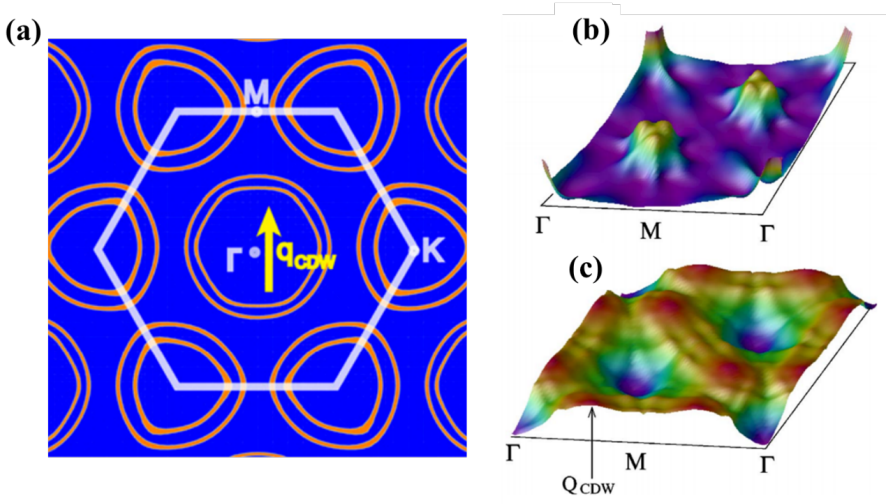

Figure 1.7: Experimental and theoretical results showing the difference between nesting and CDW vectors in $NbSe_2$. (a) Fermi surface contour of 2H-$NbSe_2$ [31], the arrow indicates observed q_{CDW} [34]. The graph is from report by Zhu et al. [35]. (b) Imaginary and (c) real part of the noninteracting susceptibility of $NbSe_2$. The arrow denotes the CDW vector [32].

electronic band structure features some saddle points below the Fermi level, and these lead to van Hove singularity which gives a divergence in electronic density of states. It is found that the saddle point can greatly enhance $\chi(\mathbf{q})$ if it is close to E_F, thus stabilizes CDW state even without Fermi surface nesting. However, layered CDWs are known for having only a weak peak at $\chi(q_{CDW})$, as shown in Fig. 1.7 (b) and (c). Besides, saddle points were only found in TMDCs that have more than one layers in a unit cell, such as 2H-$TaSe_2$ [36]. For materials of 1T structure, no saddle point was found [37].

Both Fermi surface nesting and saddle point model suggest that the CDW in layered TMDCs originates from the divergence in χ. However, several theoretical investigations [38, 39] predicted a CDW formation even without singularities in χ. There is another explanation suggests that CDW originates from strong electron-phonon coupling (EPC) [40, 41]. Indeed, from the CDW stability condition

$$\frac{4g_{\mathbf{q}}^2}{\hbar\omega_{\mathbf{q}}} - 2U_{\mathbf{q}} + V_{\mathbf{q}} \geq \frac{1}{\chi_{\mathbf{q}}},$$

it is clear that a strong electron-phonon interaction constant could make the inequality hold even without a divergence in $\chi(\mathbf{q})$. Zhu et al. [35] calculated the phonon dispersion from EPC constant, and the result is in good agreement with experiments. Band Jahn-Teller effect, which results from

EPC, can lower the overall energy with a geometrical distortion that removes degeneracy of electronic ground state. This effect has been proposed to account for the CDW in layered TMDCs [42].

Exciton condensation, a pure electronic effect, has also been suggested as a possible mechanism for some of the TMDCs such as TiS_2 and $TiSe_2$ [43, 44]. Exciton condensation is driven by electron-electron interaction. In low-carrier-density systems such as semimetal or semiconductor, when the binding energy of electron-hole pair, i.e. an exciton, exceeds the energy band gap, spontaneous formation of excitons will occur. Exciton condensation is usually accompanied with an electron density wave, a band structure change, and a lattice distortion [22]. Therefore, in exciton condensation systems, lattice distortion is merely a by-product. And the driving force of CDW is purely electronic. This explanation has been proposed for some of the layered TMDCs such as 1T-$TiSe_2$ [44].

The arguments about the origin of CDW has been long-standing, and most of the controversy is on the CDW in layered TMDCs. In fact, there could be more than one mechanism that drives CDW instability. For instance, Tonjes et al. [45] suggested a combination of Fermi surface nesting and saddle point mechanism would lead to CDW instability, and a cooperation of the band Jahn-Teller effect and exciton condensation was also proposed as a possible mechanism [46–48]. Although further experiments and theories are needed to resolve the controversy, it is unambiguous that the CDW state in layered TMDCs is peculiar and different from the classic 1-D metal chain model.

1.4 Layered Transition Metal Dichalcogenides (TMDCs): 2-D Materials

Unlike 3-D materials, in which the composition and structure (including crystal structure and microstructures) govern the physical and chemical properties, dimensionality plays a key role by adding another layer of control to the material properties in 2-D systems. Such a control is achieved via classical and quantum size effects, such as the reduction of mean free path and confinement induced change in the dispersion relations of relevant quasi-particles [49].

The 2-D materials are particularly interesting in their own right. A famous quote from Wolfgang Pauli is $'$*God made the bulk*; *surfaces were invented by the devil*$'$ [50]. While Pauli's remarks refer to the 2-D interface and the 2-D surface of 3-D bulk material, it nonetheless pointed toward the importance and intrigue of 2-D system. Among numerous 2-D materials, layered TMDCs have

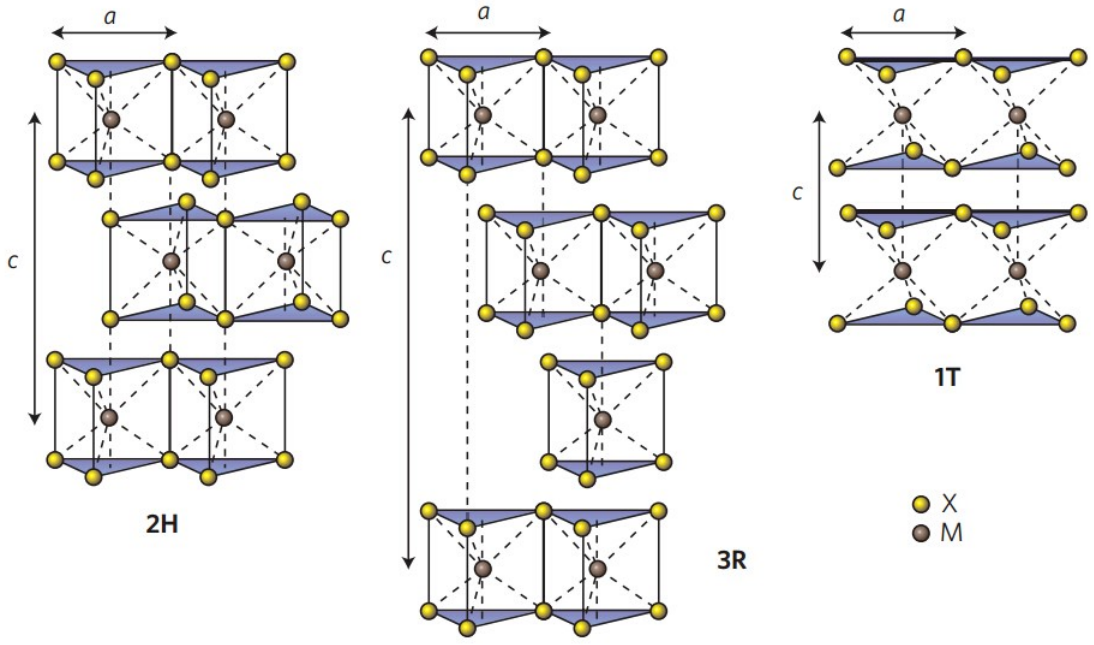

Figure 1.8: TMDC structures with different symmetries, namely, 2H, 3R and 1T. [52]

been extensively studied as they exhibit various intriguing properties such as superconductivity and the charge density wave.

The composition of TMDC family can be denoted as MX_2, where M denotes transition metal elements and X is chalcogene atoms. The M and X elements typically form atomic layers that are separated by the van der Waals (vdW) gap. So even in the bulk form (rather than monolayer or multilayer), TMDCs can be treated as quasi 2-D materials as their electrical and thermal transport are largely confined in the atomic layers separated by vdW gap.

The crystal structure of TMDC can be further categorized into: (a) one-layer trigonal form (1T), (b) two-layer hexagonal form (2H) and (c) three-layer rhombohedral (3R) form, as illustrated in Fig. 1.8. Despite the simple crystal structures, the physical properties of TMDCs greatly depend on the chemical compositions and the symmetry of crystal structure. For instance, the electronic properties of TMDCs vary from insulators (e.g HfS_2), semiconductors (e.g. MoS_2 and WS_2) to semi-metals (e.g. WTe_2 and $TiSe_2$) and true metals (e.g. NbS_2 and VSe_2) [51].

TMDCs are excellent material templates for research in many aspects. Firstly, this class of materials is binary compounds and has a relatively simple crystal structure. The small unit

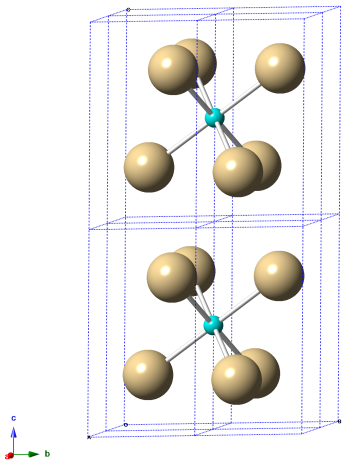

Figure 1.9: Crystal structure of 1T-VSe_2.

cell makes it easier for calculations of both electronic and phononic structure, so as to help us understand the physical properties of the material. Besides, another feature that TMDCs possess is the tunability, which arises from several aspects: (a) The vdW gap makes it feasible to intercalate guest atoms into the system, and there are many elements, even molecules, that could be used as intercalants. (b) Most TMDC materials are semiconductors, which makes it possible to dope the system to tailor the electronic band structure. (c) The phase diagrams of TMDCs are complicated, thus there are lots of control parameters, i.e. temperature, to intentionally manipulate the state of the system.

1.5 VSe_2: A TMDC Material With CDW

This dissertation is focused on a seldom studied TMDC material, the 1T-vanadium diselenides (VSe_2), and its CDW transition. Most of the previous studies on VSe_2 are done in 1970s-1980s, and mainly focus on its CDW behaviors and complex electronic structure. However, partly due to the difficulty in material synthesis, as VSe_2 has a natural tendency towards V rich, the studies on VSe_2 are much less numerous comparing with other widely studied TMDCs, such as MoS_2, $NbSe_2$ and TiS_2.

Similar to other TMDC family members, VSe_2 (which is a group VB TMDC) adopts a layered quasi 2-D structure. Contrast to the strong covalent bonding within each VSe_2 layer (i.e., ab

trigonal-prismatic			octahedral	
compd	c/a		compd	c/a
		d^0		
			TiS_2	1.67
			ZrS_2	1.59
			$TiSe_2$	1.70
		d^1		
NbS_2	1.80		TaS_2	1.75
$TaSe_2$	1.85[b]		VSe_2	1.82
		d^a		
MoS_2	1.94			
WSe_2	1.98			
		d^3		
			$ReSe_2$[c]	1.92

Figure 1.10: Coordinations and c/a ratios in TMDCs [53].

plane) is the weak vdW coupling between ab planes, which well explains the anisotropy in physical properties and also makes ionic or molecular intercalations in the vdW gap feasible. Even though the 2H form of VSe_2 exists theoretically, it is not stable in nature. Therefore, VSe_2 is typically in the 1T form (CdI_2 structure), with space group $P\bar{3}m1$, and each V atom is situated in a trigonally distorted Se octahedron, as illustrated in Fig. 1.9. However, as shown in Fig. 1.10, the c/a ratio of VSe_2 is larger than most typical 1T-TMDCs, and is close to that of the 2H-TMDCs. The large c/a ratio reveals that the 1T-VSe_2 is somehow similar to the 2H polytypes. Electronically, VSe_2 features a partially filled $3d$ band, which is much narrower than the $4d$ and $5d$ orbitals. The different d-bands can greatly affect the physical properties of the material. As illustrated in Fig. 1.11, in In 1T-TMDCs, octahedral coordination (T form) splits d-orbitals and the lowest energy level after splitting is $d_{xy}/d_{xz}/d_{yz}$ triplet, whereas the corresponding lowest energy level in trigonal prismatic coordination (H form) is d_{z^2}. However, the comparably larger c/a ratio of VSe_2 indicates a trigonal distortion of the octahedral field around V atoms, which makes d_{z^2} the lowest energy level among d-orbitals in 1T-VSe_2 [54]. The lowering of the d_{z^2} level can be regarded as the driving force of band Jahn Teller effect [40, 54] which is dependent on strong EPC.

The CDW transition(s) is one of the most studied topic in VSe_2, but it is still under many debates. Direct observations of the reduced wave vector $\mathbf{q}$ of PLD show inconsistent results:

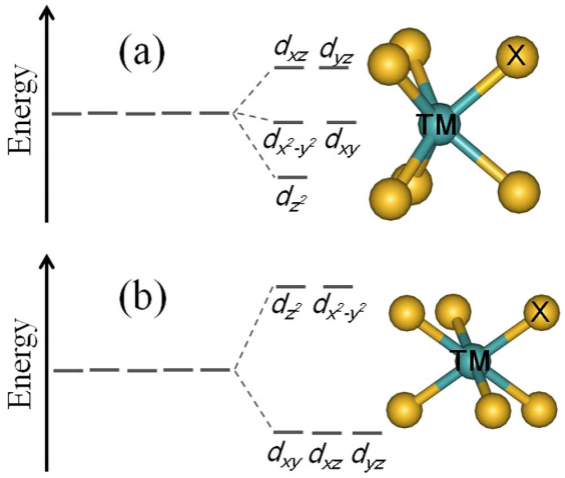

Figure 1.11: Schematic representation of d-orbital splittings of TMDCs with (a) trigonal prismatic coordination and (b) octahedral coordination [55].

In-plane component of $\mathbf{q}$ is 2% incommensurate at 140 K and commensurate $(1/4)\mathbf{a}^*$ at 40 K, while commensurate $(1/3)\mathbf{c}^*$ along $\mathbf{c}^*$, as reported by Williams [56]; $\mathbf{q} = 0.250\mathbf{a}^* + 0.305\mathbf{c}^*$ and is temperature independent, as reported by Moncton et al. [57]; $\mathbf{q} = (0.246\pm0.007)\mathbf{a}^*+(0.294\pm0.008)\mathbf{c}^*$ at 20 K, as reported by Tsutsumi et al. [58]; $\mathbf{q} = (0.250 \pm 0.003)\mathbf{a}^* + (0.307 \pm 0.003)\mathbf{c}^*$ below 85 K and $\mathbf{q} = (0.250 \pm 0.003)\mathbf{a}^* + (0.314 \pm 0.003)\mathbf{c}^*$ above 85 K, as reported by Tsutsumi [59]; $\mathbf{q} = (1/4)\mathbf{a}^* + (1/3)\mathbf{c}^*$ (possibly at 10.7 K), as reported by Strocov et al. [60]. The inconsistency in the literatures is likely to be due to the existence of excess V atoms in sample preparations, which is quite hard to avoid and will affect the CDW formation [61,62]. Nevertheless, it is generally accepted that there is a second-order [57,59,62,63] phase transition near 110 K (actual transition temperature depends on sample conditions), as suggested in the electrical resistivity measurements [59], and this transition temperature is sometimes refered as the onset transition temperature or T_{CDW} in the rest of the dissertation. This phase transition is attributed to the transition from normal state to the (commensurate in $\mathbf{a}^*$ direction and possibly incommensurate in $\mathbf{c}^*$ direction) CDW state. On the other hand, the existence of an incommensurate-commensurate CDW transition at a lower temperature (the lock-in transition temerature) in 1T-VSe_2, as in some other 1T-CDWs such as 1T-TaS_2 and 1T-$TaSe_2$ [4], is still under doubt. In 1979, A.H. Thompson and B.G. Silbernagel [64] studied VSe_2 with nuclear magnetic resonance (NMR) and observed a distinct change in the ^{51}V hyperfine coupling constant at 70K, and attributed it to the incommensurate to commensurate

CDW transition. However, some other group(s) [65] claimed there are no abrupt changes in the NMR parameters near 70 K, and X-ray diffraction measurements showed no further change after the 110 K transition down to low temperatures [57].

It is of great interest that the reduced wave vector of VSe_2 is 3-D, despite the 2-D nature of the crystal structure. Actually, the $\mathbf{q}_{CDW}$ in most 2-D CDWs are 2-D. To the best of the author's knowledge, VSe_2, TaS_2, $TiSe_2$ are the only three TMDCs that manifest 3-D CDW state [60, 66, 67]. Another rarely found feature in VSe_2 is its unusual pressure dependence. In contrast to all the 1T and 2H polytypes studied, the CDW formation in VSe_2 is enhanced under pressure [54]. Friend et al. [54] reported that the transition temperature in VSe_2 moves to higher temperatures as pressure increases, and they contributed the different pressure dependence between VSe_2 and other TMDC CDWs to the narrower d-band together with larger Coulomb repulsion. It was also noted by Friend et al. [54] that Coulomb repulsion opposes CDW formation which brings electrons closer on average, and since the 3d band in VSe_2 is about 3-5 times smaller than 4d Nb and 5d Ta, the CDW formation in VSe_2 can be stabilized by applying pressure which broadens the d-band.

For the origin of the CDW in VSe_2, some groups attributed it to the Fermi surface nesting of the V $3d_{z^2}$ band [60, 68], while electronic susceptibility calculated by Yoshida and Motizuki only gave a weak enhancement at the nesting vector [69]. Johannes and Mazin also argued that even the Fermi surface is perfectly nested, it could be easily destroyed by even small deviations [33]. Therefore, as in many other layered TMDCs, the origin of CDW in VSe_2 is still unclear.

The primary goal of this work is to investigate the nature of CDW in VSe_2 via density functional theory (DFT) calculations and experimental measurements. Most experiments conducted in this work are transport properties measurements. While there are some other techniques that can probe the CDW formation more directly (cf. Appendix A), transport properties still contain substantial information on the nature of the CDW transition in VSe_2. In this work, it is found that VSe_2 exhibits some interesting features comparing with other CDWs. The most intriguing observation is the weak anomaly across CDW temperature, indicating only a small number of electrons are involved in CDW formation.

Chapter 2

Density Function Theory (DFT) Calculations

DFT calculations were performed on bulk 1T-VSe_2 to serve as a guidance for the expected experimental results (cf. Chapter 4). The calculations include spin polarized electronic band structure, density of states (DOS) and Fermi surface topology, along with phonon dispersion relation and phonon DOS. From the Fermi surface topology, the percentage of nested Fermi surface was plotted as a function of wave vector, and the results were compared with experimental observed reduced wave vector $\mathbf{q}$ of PLD ($\mathbf{q}_C DW$) [57].

By employing DFT as implemented in Quantum ESPRESSO [70], the equilibrium structure of bulk VSe_2 was fully optimized and the corresponding band structure was calculated. Generalized gradient approximation (GGA) [71] of Perdue-Burke-Ernzerhof (PBE) was used for the exchange-correlation function, and the interaction between electrons and ions was modeled by using the ultrasoft pseudopotential. Considering the influence of vdW gaps in bulk VSe_2, the Grimme-D2 method [72] with the inclusion of dispersion energy correction was adopted in this calculation. The kinetic energy cutoff was set to 60 Ry (1Ry=13.606 eV) for the plane-wave expansion of the electronic wave functions, and the charge-density cutoff was kept at 600 Ry, while the Methfessel-Paxton [73] smearing size was fixed at 0.002 Ry. The Brillouin zone integration was performed using the Monkhorst-Pack scheme [74] with $19 \times 19 \times 9$ meshes. The lattice constant of VSe_2 was optimized, until the total energy converged to at least 10^{-6} Ry and the forces between atoms became

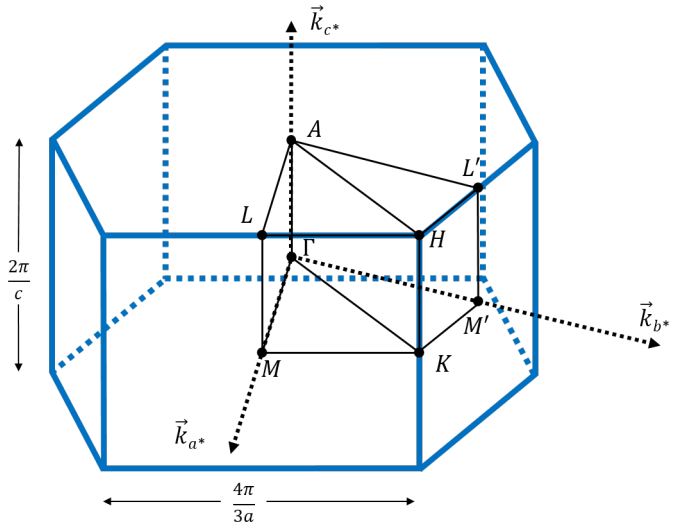

Figure 2.1: High symmetry directions in the first Brillouin zone of 1T-VSe_2.

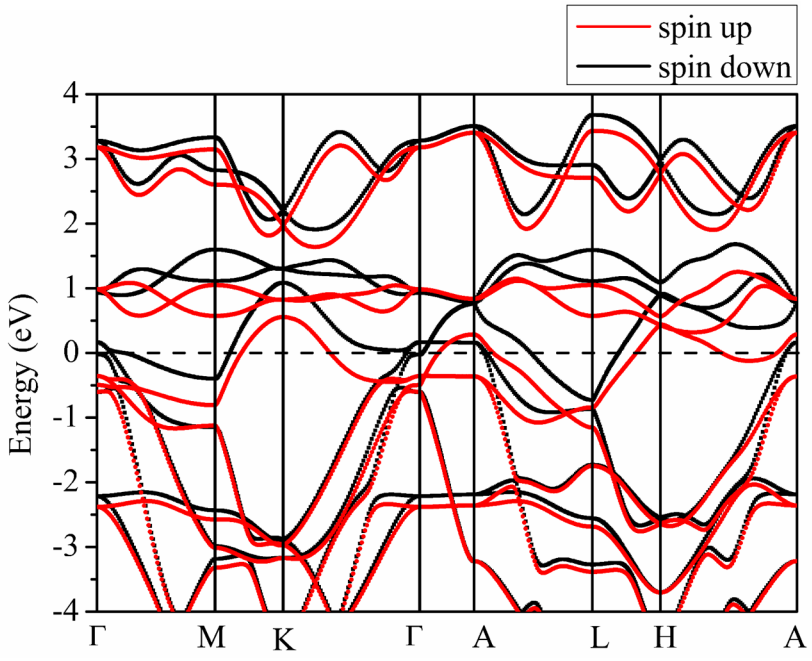

Figure 2.2: Electronic band structure of 1T-VSe_2.

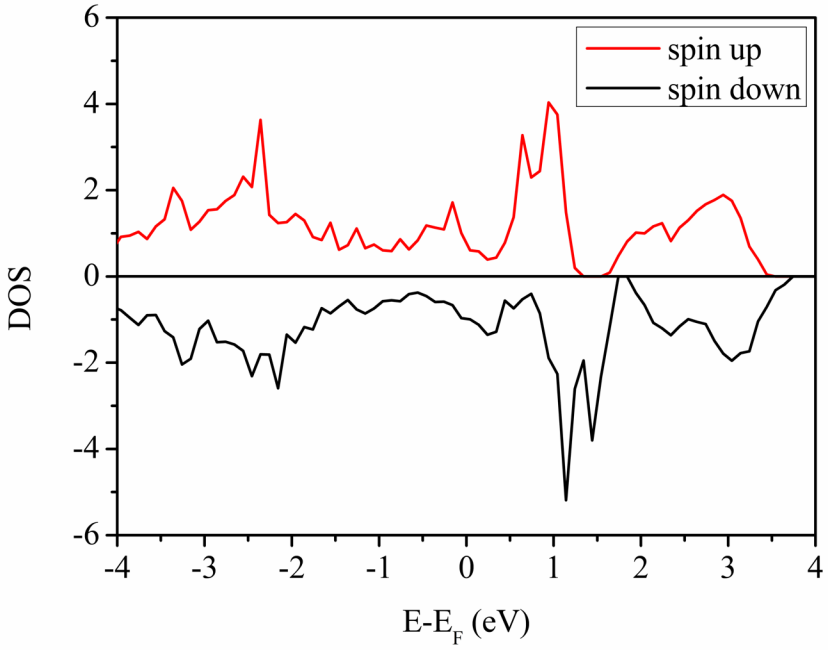

Figure 2.3: Electronic DOS of 1T-VSe_2

smaller than 10^{-4} Ry/bohr.

The calculated structure of VSe_2 is of 1T form, with space group $P\bar{3}m1$, and the lattice constants a and c are 3.322$\mathring{A}$ and 6.261$\mathring{A}$, respectively. The structure is reasonable and consistent comparing with results solved from refinements based on X-ray diffraction data (cf. Section 3.2), while only the value of c is slightly larger.

The corresponding band structure of 1T-VSe_2 in high symmetry directions (as illustrated in Fig. 2.1), is shown in Fig. 2.2. Metallic behavior with multi-band conduction in VSe_2 is demonstrated, with the Fermi level of -7.58 eV. Energy levels of spin up electrons are considerably lower than those of spin-down electrons, giving a spin polarized band structure. A net magnetic moment of 0.429 μ_B is calculated, with the magnetic moments possessed by V atom and Se atom are 0.483 μ_B and -0.027 μ_B, respectively. The energies at ferromagnetic state and non-magnetic state are compared, and the ferromagnetic state is 5.7 meV lower in energy, and this value is very close to that calculated by Fang et al. (5 meV) [75]. Even though the ferromagnetic state is energetically favored, the energy difference is too subtle to conclude that the ground state of the system is ferromagnetic.

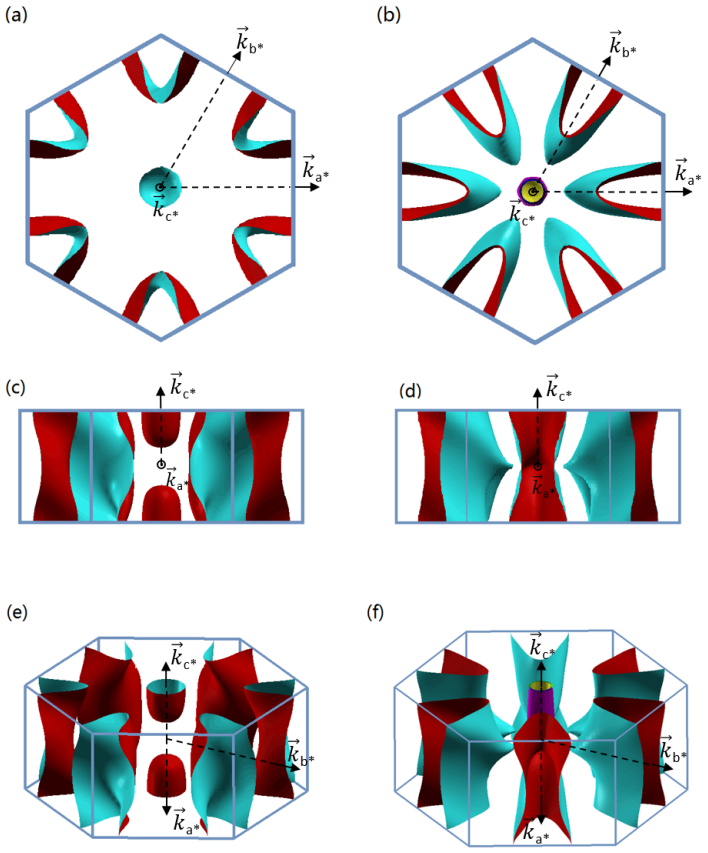

Figure 2.4: Fermi surface of 1T-VSe_2. Fermi surface along for spin up bands are shown in (a),(c) and (e), along different direction. Spin down Fermi surface along the same directions are shown in (b),(d) and (f), correspondingly.

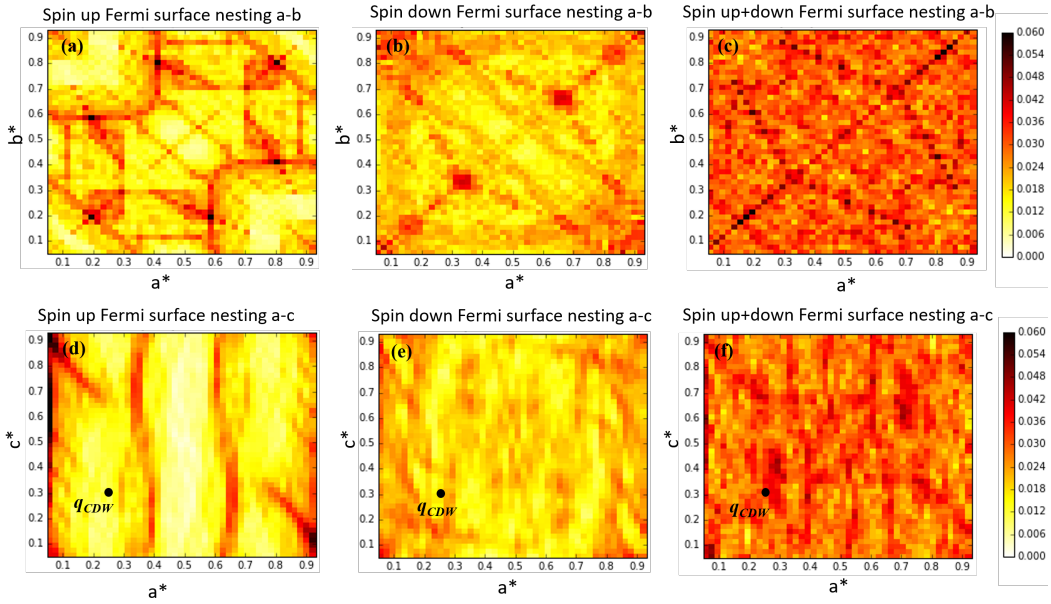

Figure 2.5: Amount of Fermi surface nested at different wave vectors, in both in-plane and out-of-plane directions. The color bar indicates the percentage of nesting, and the black dots are the observed q_{CDW}.

For the spin polarized electronic density of state (DOS) calculation, tetrahedron method with $31 \times 31 \times 31$ denser k-point mesh was used, and the results is given in Fig. 2.3. The gapless nature across Fermi level confirms the metallic behavior of VSe_2. Additionally, it is found that spin up electrons have larger DOS at Fermi surface.

3-D Fermi surfaces of both polarizations were obtained using the Wannier 90 program [76], which is also packed in Quantum Espresso, and the result is shown in Fig. 2.4. Compared with the VSe_2 Fermi surface probed by ARPES [60, 68], it is found that the calculated Fermi surface with spin up polarization in this work is very like the experimental observed Fermi surface in the MKM' plane, except that the six ellipsoids are of smaller size. On the other hand, the calculated Fermi surface of spin down polarization is in good agreement with the observed Fermi surface in the LHL' plane. From the calculated band structure and Fermi surface topology, it can be seen that: (1) the ellipsoidal Fermi surface across Brillouin zone boundaries is attributed to the V $3d_{z^2}$ band (electron-like); (2) the entire spin up Fermi surface is from V $3d_{z^2}$ band, whereas for spin down Fermi surface, S 4p band (hole-like) contributes to the intensity at $\Gamma(A)$ point. This agrees with the ARPES result done by Terashima et al. [68].

Some earlier reports attributed the CDW formation in VSe_2 to Fermi surface nesting. The ARPES measurment by Terashima et al. [68] suggested that the V 3-d Fermi surface had a straight portion that satisfies nesting condition. However, neither the spin up nor the spin down Fermi surface from the DFT calculations in this work reproduces the straight portion. Moreover, since CDW in VSe_2 is 3-D, so the $\mathbf{c}^*$ direction must be taken into consideration. Strocov et al. claimed that the nesting vector was in the $MLL'M'$ plane based on the ARPES measurement [60], and they found the $\mathbf{q}_C DW$ was near a $\mathbf{q}$ spot with maximum Fermi surface nesting percentage.

Fig. 2.5 shows the relationship between nesting vector and the percentage of nested Fermi surface in two directions. The observed $\mathbf{q}_{CDW}$ [57] is marked as a black dot. It is apparent that $\mathbf{q}_{CDW}$ doesn't correspond to the maximum in the correlation map. The color bar shows the amount of Fermi surface nested, so there is at most only a few percent of Fermi surface involved in the nesting effect excluding $\mathbf{q}_{CDW} = 0$. It is worth noting that the spin up result (Fig. 2.5(d)) is similar to the correlation map between Fermi suface nesting intensity and wave vector based on the ARPES result by Strocov et al. [60], but with an offset in a^* direction. The spin down result doesn't show a specific maximum at particular position. As shown in Fig. 2.5(f), the observed $\mathbf{q}_{CDW}$ [57] does not match the wave vector of maximum Fermi surface nesting, and this result is in contradict with the conclusion made by Strocov et al. [60]. However, it is worth noting that no specific percentage of Fermi surface nesting was given by Strocov et al., while the results of this work suggests that even at the maximum point of Fermi Surface nesting, the percentage of nesting is still very low. Therefore, based on the results of this work, it is questionable to solely attribute the CDW in bulk 1T-VSe_2 to Fermi surface nesting.

Aside from electronic band structures, phonon dispersion relation was also calculated. The phonon frequencies, dynamical matrices were obtained using density-functional perturbation theory (DFPT) [77] with a $4 \times 4 \times 4$ q-point grid, which is also as implemented in QUANTUM-ESPRESSO. That's the first time phonon dispersion relation of 1T-VSe_2 is calculated to the best of the author's knowledge. The results are shown in Fig. 2.6 and 2.7. There is no optical phonon modes below wave number of $\sim 100 cm^{-1}$.

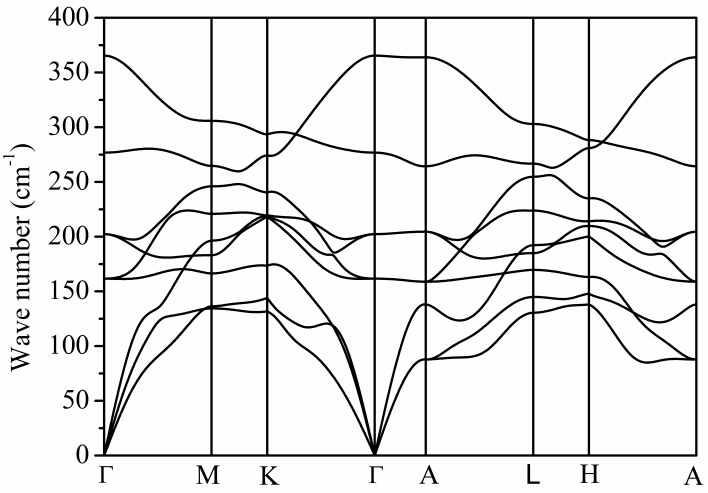

Figure 2.6: Phonon dispersion relation of VSe_2.

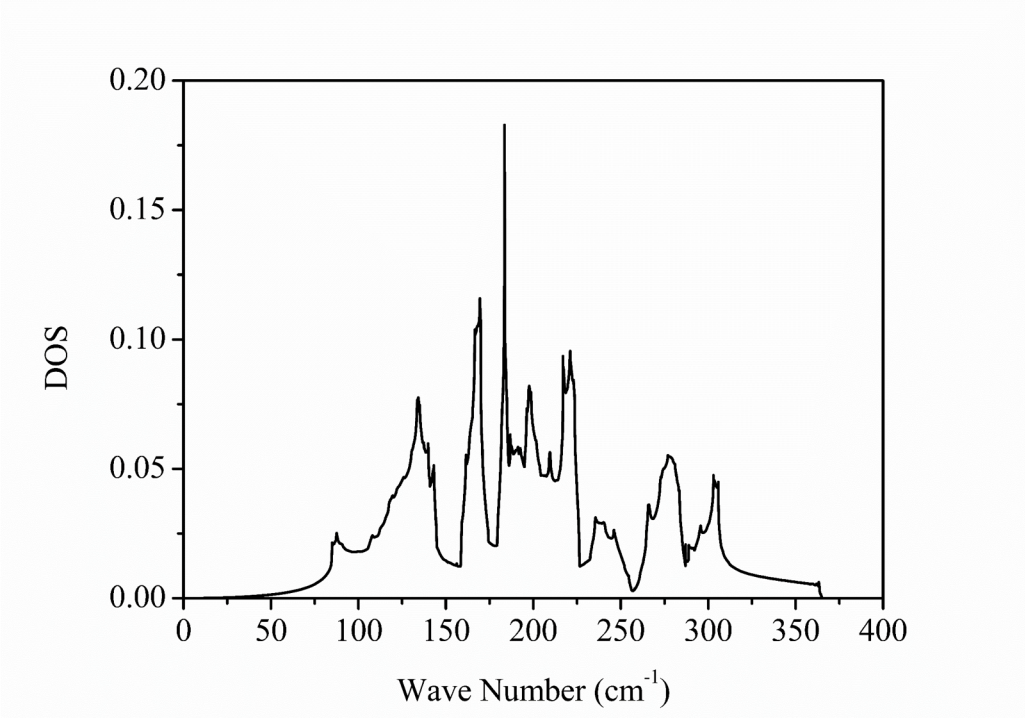

Figure 2.7: Phonon DOS of VSe_2.

Chapter 3

Material Synthesis, Processing and Characterizations

3.1 Material Synthesis and Processing

3.1.1 Single-Crystalline VSe_2 Samples

In this work, VSe_2 single crystals were prepared using a vapor transport technique. Stoichiometric fine powder of V (99.5%, Alfa Aesar) and Se (99.999%, Alfa Aesar) , with a few micro grams iodine (99.9985%, Alfa Aesar) was thoroughly mixed and sealed in an evacuated quartz tube. The quartz tube was then placed in a Lindberg/Blue M single zone tube furnace (Model TF 53055A), and was heated at 700°C for 5 days. Most of the as-grown products were formed at the cold end of the quartz tube, in the form of black shiny thin flakes. Size of the flakes range from $7 \times 4mm$ to less than $0.5 \times 0.5mm$. The flakes were then heated at 100°C for a few minutes to remove the residual iodine. Finally, the single crystals were again sealed in an evacuated quartz tube with pure Se powder, and heated at 550°C for 3 days, to minimize the off-stoichiometry. Fig. 3.1 is a picture of as prepared VSe_2 single crystals.

Due to the different dimension requirements of apparatus and the brittle nature of single crystals, it is not feasible to perform measurements on the same sample, but all samples measured were from the same batch. Raman spectrum measurements (with Witec alpha 300R, Germany) were performed on multiple samples, and there were no noticeable changes among different samples,

which is an indication of good composition consistency, even though slight difference may exist among samples and lead to inconsistency in physical properties.

Dimensions of sample were measured by looking through optical microscope with a scale and known magnification. As the thickness of the single crystal is very samll, it could only be roughly estimated. The largest piece of sample, with size around $7 \times 4 \times 0.01$ mm, was cut down to $3 \times 0.2 \times 0.01$ mm needle-like pieces, which was used for electrical resistivity (with Quantum Design PPMS-6000), Seebeck coefficient (with home made resistivity and Seebeck coefficient measuring system (R&S) [78]), thermal conductivity (with home made parallel thermal conductivity measurement apparatus [79]) and Hall coefficient measurements (with Quantum Design physical property measurement system (PPMS) 6000).

It should be noted that uncertainty in the thickness estimation of single-crystalline VSe_2 is quite large and couldn't be ignored. The accuracy of the magnitude measurements of electrical resistivity, thermal conductivity, Hall coefficient and Hall angle are all influenced, while their temperature trends remain unaffected. That's why some earlier works only reported electrical resistance instead of resistivity [80].

The sample used for X-ray diffraction measurement (with Bruker D8 Venture diffractometer) is of smaller size, which is around 0.33×0.31 mm. About a dozen of different samples with length 2-0.5 mm were used for heat capacity measurements (with Quantum Design PPMS-6000), and magnetic susceptibility was measured with Quantum Design Magnetic Property Measurement System (MPMS) on a sample around 1×2 mm.

3.1.2 Poly-crystalline VSe_2 samples

Poly-crystalline VSe_2 powder was prepared by chemical reaction in a sealed quartz tube inside a box furnace. Selenium shots (Alfa Aesar, amorphous, 2-4 mm, 99.999%) were firstly ground into powder, and then mixed with vanadium powder (-325 mesh, 99.5%, Alfa Aesar) at the stoichiometric 2:1 ratio. The mixed powder was sealed in an evacuated quartz tube and placed in a box furnace (Carbolite CWF1300). The tube was then heated up to 650°C in 24 hrs, then kept at 650°C for 3 days, and finally cooled to room temperature in 40 hrs. The as prepared VSe_2 powder was mostly found at the bottom of the quartz tube, with charcoal grey color.

The as-grown powder was then examined with X-ray powder diffraction (XRD) (on Rigaku Ultima IV X-ray diffractometer with Cu $K\alpha$ radiation) and details of the result will be given in

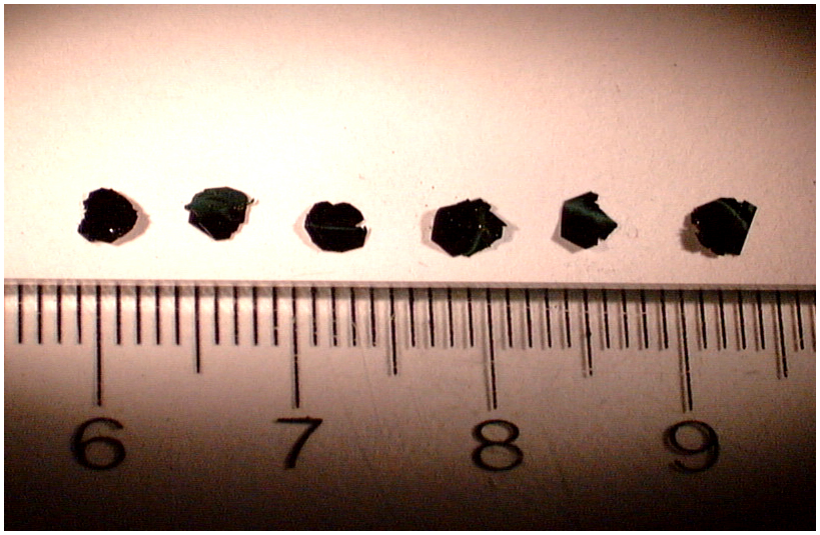

Figure 3.1: Picture of the as-grown VSe_2 single crystals.

section 3.2.1.2. To obtain a solid bulk sample, the synthesized powder was further hand ground in an agate mortar, and then densified into a solid disk disk (with diameter = 12.7 mm and thickness = 1.93 mm) at 630°C, using (DR.SINTER 515S) spark plasma sintering (SPS) system. Density of the sintered disk was measured with the Archimedes method and the result is 5.31 g/cm^3, which is about 92% of the theoretical value.

The disk was cut into a $8.5 \times 2.5 \times 1.8mm$ bar for low temperatures thermal conductivity (with homemade thermal conductivity measuring system [81]), electrical resistivity and Seebeck coefficient measurements (with homemade resistivity/Seebeck-coefficient apparatus [78]). A portion of the cut off pieces was ground into powder for XRD measurements (Rigaku Ultima IV X-ray diffractometer, Cu α-line; Empyrean, Cu α-line, PANalytical, Holland), and the other parts were used for specific heat (with NETZSCH-DSC 404 & PPMS-9 Quantum Design & ^{3}He cryostat) and Raman spectrum (Witec alpha 300R, Germany) measurements, respectively.

3.2 Characterizations

3.2.1 X-Ray Diffraction and Structure Solution/Refinement

X-ray diffraction measurements were conducted on both single- and poly-crystalline VSe_2 samples. The results are not only crucial for phase purity analysis, but they also provide useful

	VSe_2 at 100K	VSe_2 at 300K
Crystal System	trigonal	trigonal
Space Group	$P\bar{3}m1$	$P\bar{3}m1$
Unit Cell Parameters	$\alpha = \beta = 90°, \gamma = 120°$ $a = b = 3.3491\mathring{A}$ $c = 6.1064\mathring{A}$	$\alpha = \beta = 90°, \gamma = 120°$ $a = b = 3.3630\mathring{A}$ $c = 6.1119\mathring{A}$
Calculated Density (g/cm^3)	5.847	5.794
Goodness-Of-Fit on F^2	1.123	1.157

Table 3.1: Results of crystal structure refinement of VSe_2 at 100K and 300K, respectively.

Atom		Wyckoff	x/a	y/b	z/c	U_{eq}
Se	100K	2d	0.6667	0.3333	0.2572	0.0023
	300K		0.6667	0.3333	0.2567	0.0090
V	100K	1a	0.0000	0.0000	0.5000	0.0044
	300K		0.0000	0.0000	0.5000	0.0077

Table 3.2: Atomic positions and displacement parameters of VSe_2 at 100K and 300K, respectively. The z-parameter of Se varies slightly with temperatures.

information about crystal structures.

3.2.1.1 Single-Crystalline VSe_2

Single crystal X-ray diffraction data were collected on a single crystal VSe_2 flake at room temperature and 100 K respectively, using phi and omega scans on a Bruker D8 Venture diffractometer equipped with a Mo microfocus X-ray tube and a Photon 100 CMOS detector, at the Chemistry Department of Clemson University. The collected data were processed using SAINT and SADABS algorithms, as part of the Apex3 software package. Further structure solutions and refinements were performed using the SHELXTL software suite [82].

The onset CDW transition temperature in VSe_2 is generally regarded as 110 K [59, 62, 65]. However, in practical, the temperature varies in different samples [64, 80, 83–88]. Unfortunately, 100 K is the lowest temperature the single crystal X-ray diffraction measurement could reach, even though it can not be guaranteed that the single-crysal VSe_2 sample is under CDW state at this temperature.

The results solved are presented in Table 3.1 and Table 3.2, and there is no distinct structure changes observed on the single crystal VSe_2 at 300K and 100K. Structures at both temperatures can be well indexed to a space group $P\bar{3}m1$, and the change in unit cell parameters are considered

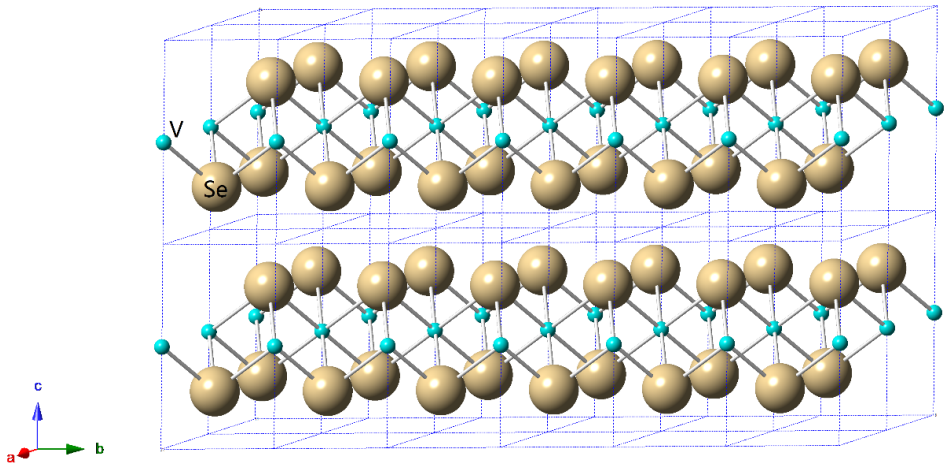

Figure 3.2: Solved crystal structure of VSe_2 at room temperature.

due to thermal expansion. Fig. 3.2 represents the crystal structure of VSe_2 at 300K based on the solved structure parameters.

X-ray powder diffraction (XRD) patterns of VSe_2 at room temperature and 100K were generated by Mercury software, as shown in Fig. 3.3. It can be seen that, to the limit of resolution, crystal structures of single crystal VSe_2 at 300 K and 100 K are identical to each other. The patterns will be further used to compare with the measured XRD patterns of poly-crystalline VSe_2 in the following section.

3.2.1.2 Poly-crystalline VSe_2

The XRD measurement of poly-crystalline VSe_2 samples before and after SPS was firstly performed with a benchtop X-ray diffraction instrument (Rigaku Ultima IV X-ray diffractometer,Cu α-line) at room temperature. Data points were taken from 10° to 90°, with a scan speed of 2.5°/min. The XRD patterns are presented in Fig. 3.4. To further investigate the fine structure of poly-crystalline VSe_2, a higher resolution X-ray powder diffractometer (Model: Empyrean, Cu α-line, PANalytical, Holland) was adopted, with Data points taken from 10° to 120° at a scan speed 0.1°/min. The corresponding XRD pattern is shown in Fig. 3.5.

From the results in Fig. 3.3 - Fig. 3.5, it is concluded that the main phase of poly-crystalline sample is VSe_2, and there is no discernible secondary phase observed in the XRD patterns (Fig. 3.4) measured at Department of Chemistry of Clemson University. Two peaks ((003) at 44.5° and (113)

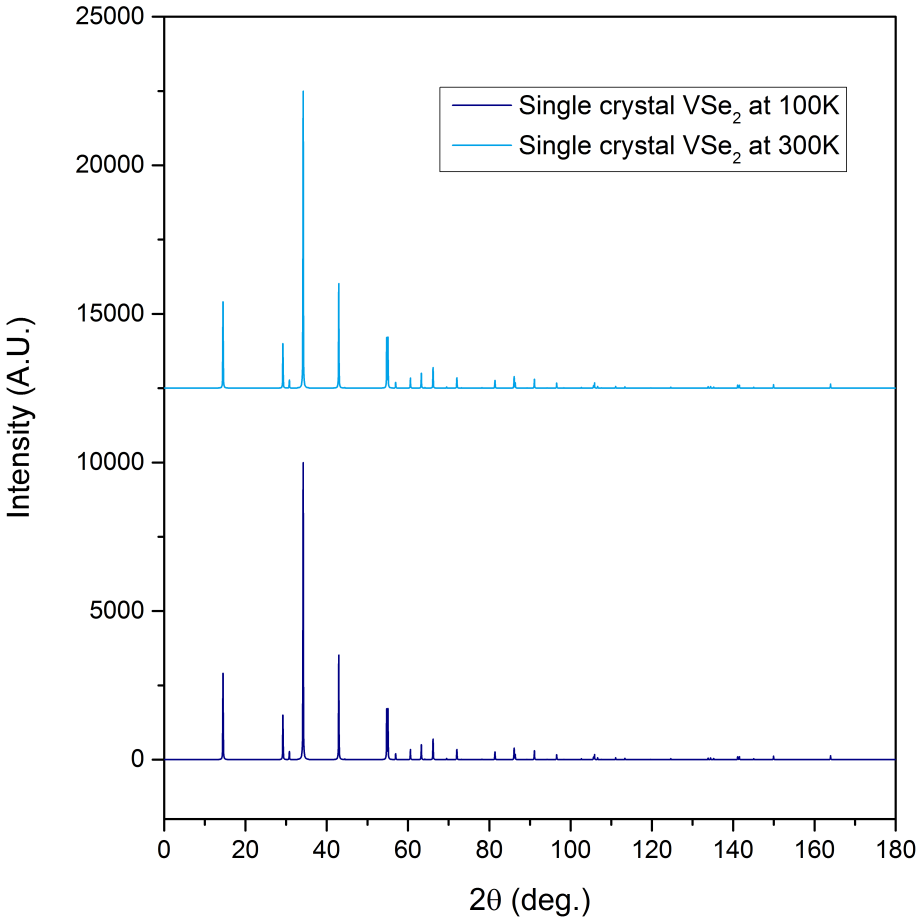

Figure 3.3: Simulated XRD patterns of single-crystalline VSe_2.

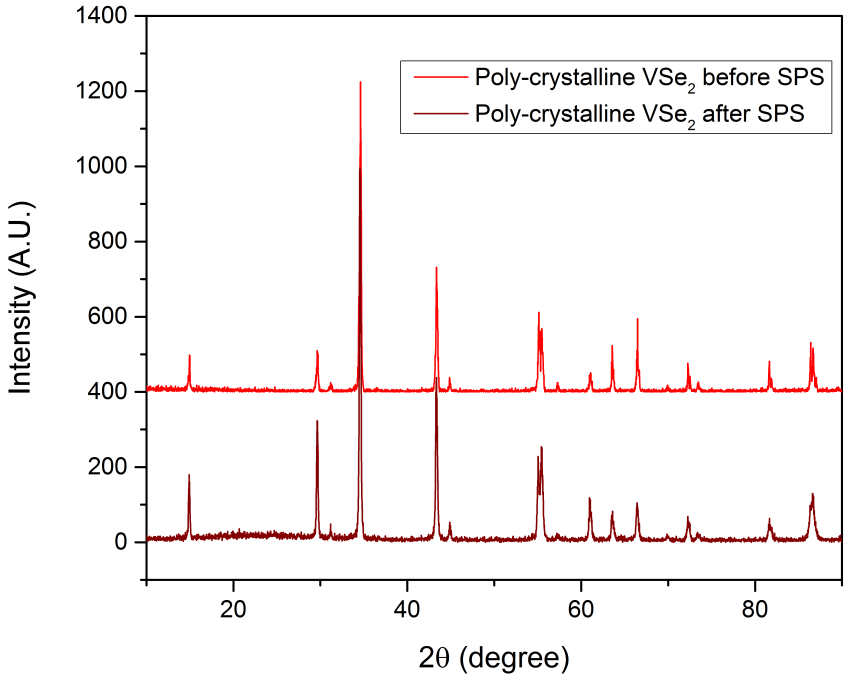

Figure 3.4: XRD patterns of poly-crystalline VSe_2 before and after SPS at room temperature.

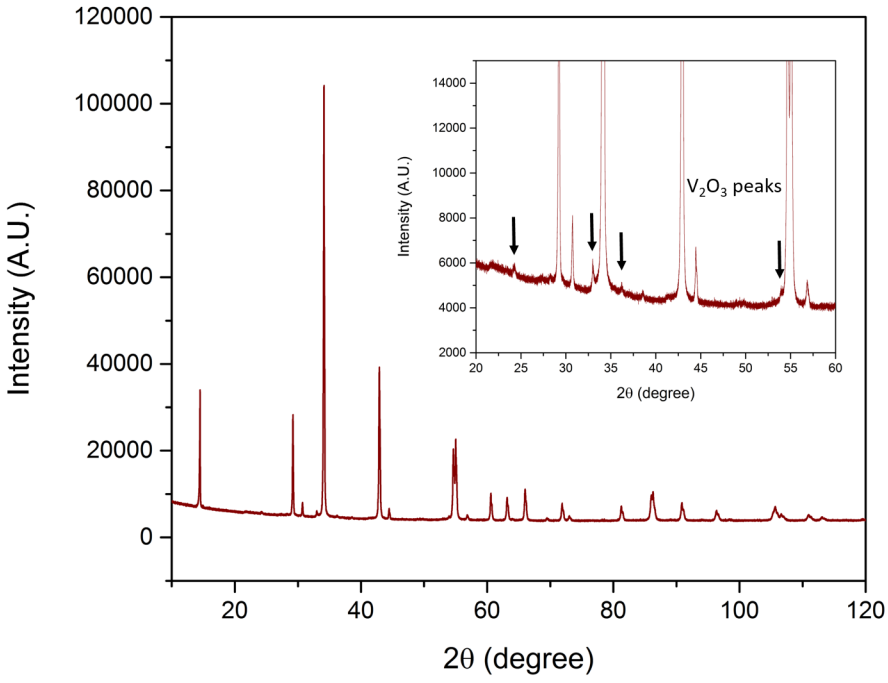

Figure 3.5: XRD pattern of poly-crystalline VSe_2 after SPS, at a better resolution.

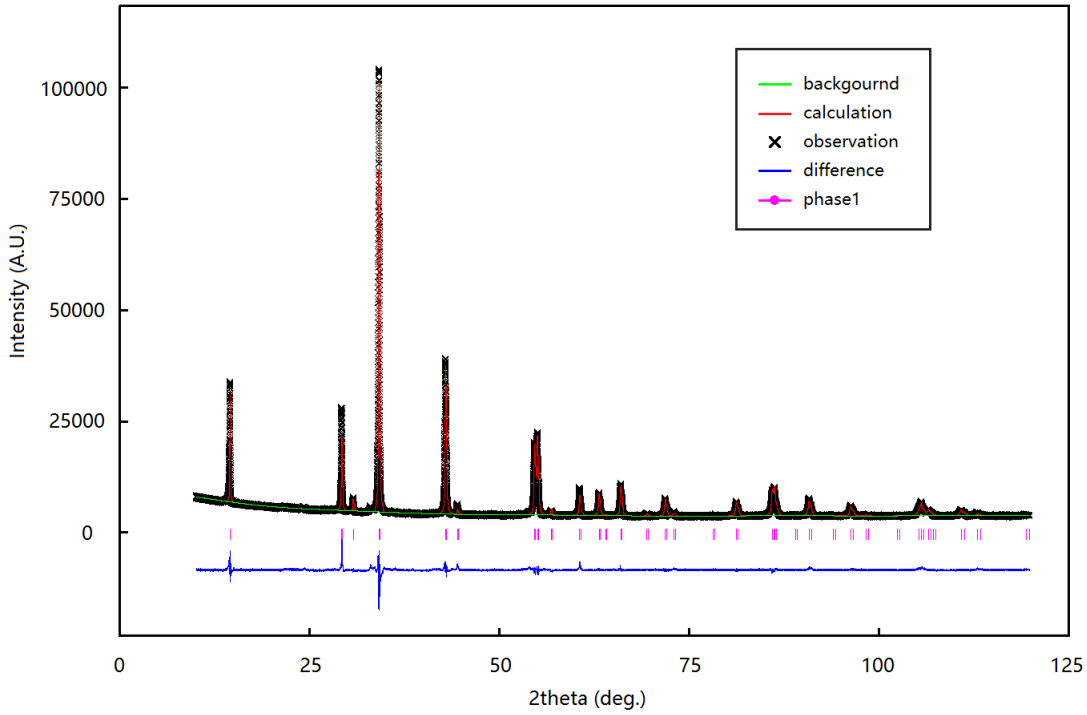

Figure 3.6: Rietveld refinements using GSAS software package: pattern fitting with high resolution XRD results of poly-crystalline VSe_2 after SPS.

at 73.1°) that are very weak in simulated XRD pattern based on single crystal structure parameters, are more intense in polycrystal XRD results. However, in the high-resolution XRD results, weak peaks at 24.15°, 33.00°, 36.25°, 53.94° are detected, attributed to trace amount of V_2O_3 phase.

Based on the results of high resolution XRD, Rietveld refinement [89] for poly-crystalline VSe_2 was performed using General Structure Analysis System (GSAS) software package [90] with the EXPGUI interface [91]. The agreement factors [92] of the refinement are $R_{wp} = 3.76\%$, $R_p = 2.42\%$, $\chi^2 = 7.205$ and $R_{F^2} = 8.23\%$, respectively. The pattern fitting is presented in Fig. 3.6, and the refinement results are summarized in Table 3.3, which shows no significant difference comparing with solved single crystal single crystal results. The off-one site occupancies seem to suggest V vacancies from the original V sites.

3.2.2 Scanning electron microscope (SEM)

SEM image of one of the single crystal flakes from the same batch of the crystals that all measurements were performed on is shown in Fig. 3.7. The surface looks smooth and layered texture

Space Group $P\bar{3}m1$										
$a = b = 3.3571\mathring{A}, c = 6.1085\mathring{A}$										
$\alpha = \beta = 90°, \gamma = 120°$										
	x	y	z	Occupancy	U11	U22	U33	U12	U13	U23
Se	2/3	1/3	0.24753	1.0186	0.02347	0.02347	0.00200	0.01263	0	0
V	0	0	1/2	0.9540	0.01256	0.01256	0.00532	0.00497	0	0

Table 3.3: Rietveld refinement results of poly-crystalline VSe_2.

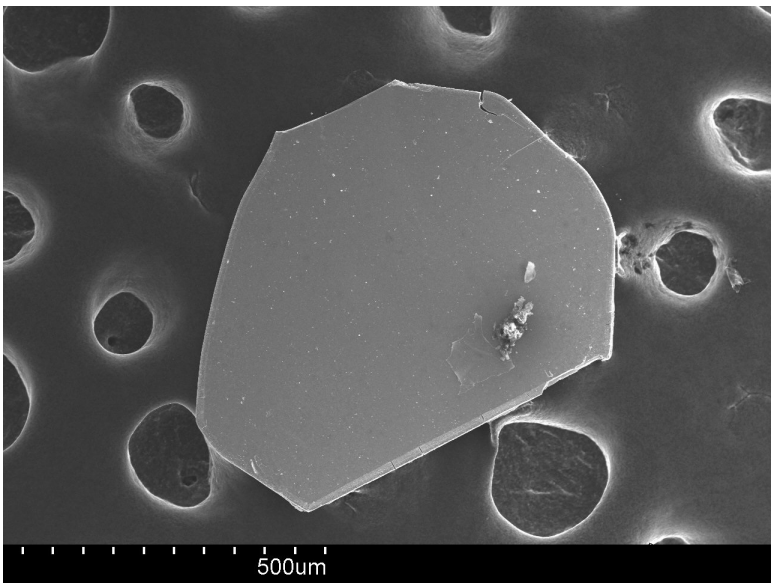

Figure 3.7: SEM image of a single crystal VSe_2 flake.

could be seen at certain spots.

Anisotropic morphology is demonstrated in the poly-crystalline VSe_2 disk by SEM. When poly-crystalline VSe_2 powder was densified into a disk in the SPS, current and pressure were applied along the axis of the disk. Combined with the layer-structure nature of VSe_2, it is expected that the in-plane direction of VSe_2 crystal will tend to align more with the upper/lower surfaces of the disk, and it is confirmed by the SEM images. It could be seen that, in the SEM images taken on a cross-section perpendicular to the axis of disk (Fig. 3.8), higher amount of VSe_2 crystal pieces (with average size around $100\mu m$) are with their ab-plane face up. In contrast, in a cross-section along the axis of disk (Fig. 3.9), more crystal pieces are inclined or with their edges up.

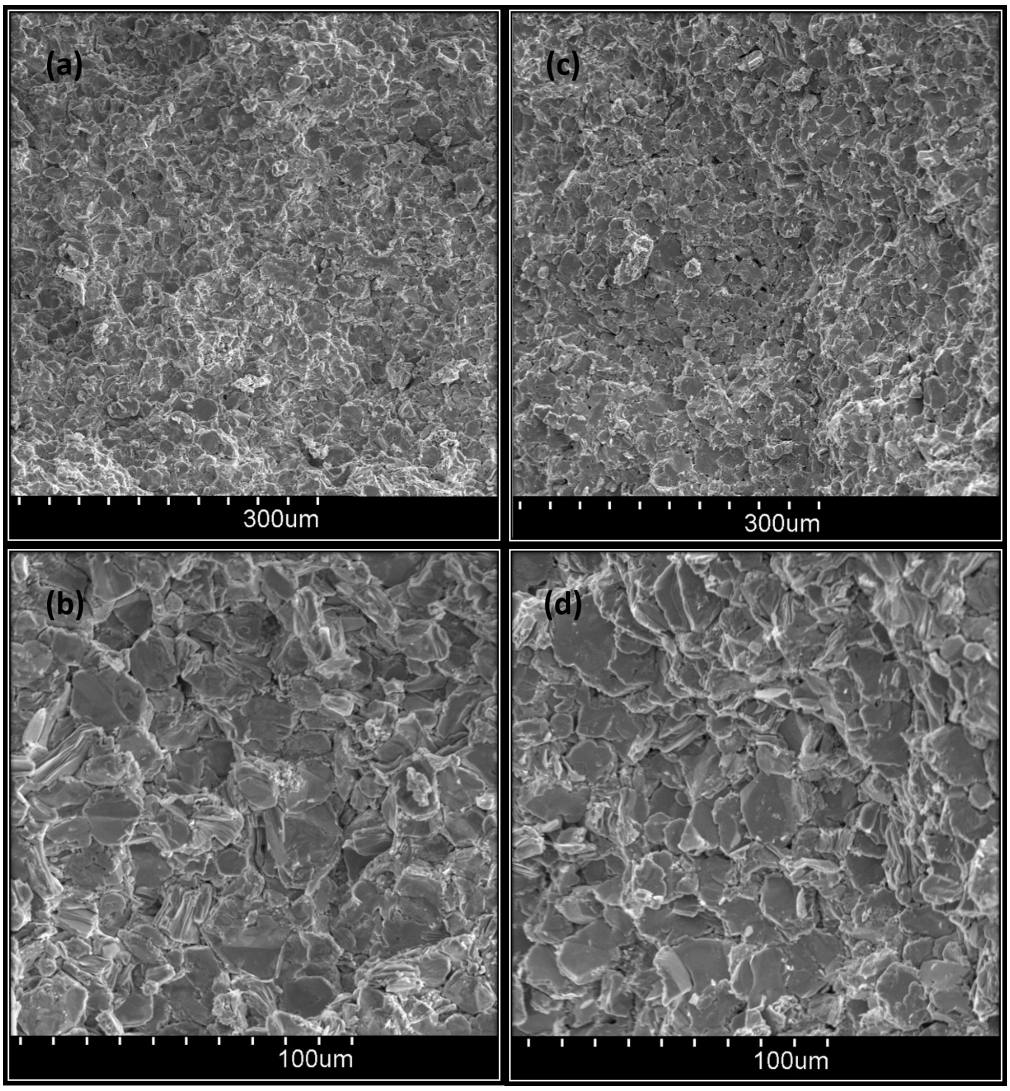

Figure 3.8: A cross-section of poly-crystalline VSe_2 disk, in the direction that is perpendicular to the axis of the disk. (a)(b) and (c)(d) are the SEM images at two different spots.

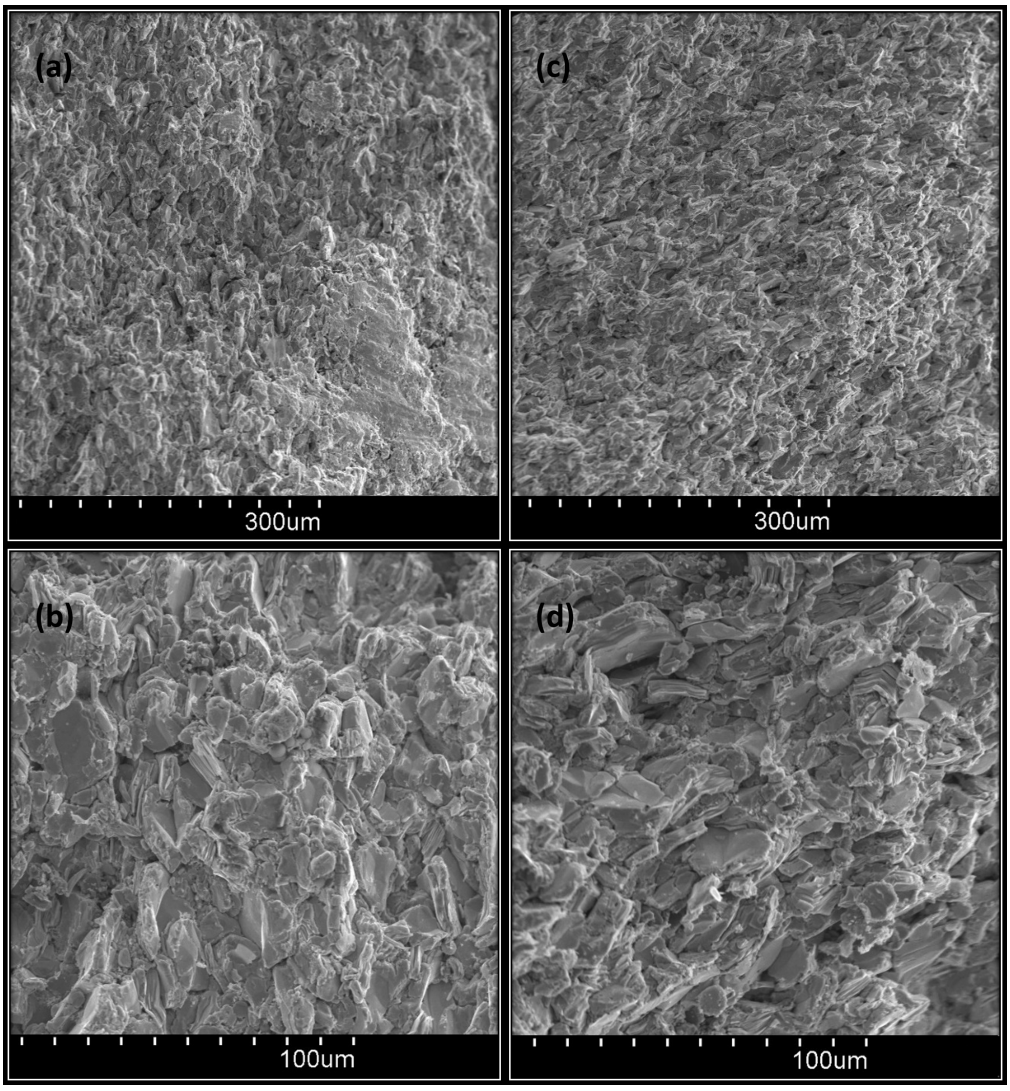

Figure 3.9: A cross-section of poly-crystalline VSe_2 disk, in the direction that is parallel to the axis of the disk. (a)(b) and (c)(d) are the SEM images at two different spots.

Chapter 4

Results and Discussions

In this chapter, the experimental studies on both single- and poly-crystalline VSe_2 will be presented, by means of electrical resistivity, Seebeck coefficient, Hall coefficient/carrier concentration/mobilility/Hall angle, magnetic susceptibility, heat capacity and thermal conductivity measurements. The studies are mainly focused on the influences of the CDW transition on magnetic and transport properties of VSe_2. Additionally, low temperature ($< 10K$) anomalies in electrical resistivity and heat capacity are firstly reported, and they will be discussed in Section 4.8.

In section 4.7, experimental results conducted on VSe_2 will be compared to other CDWs, mainly including $NbSe_3$, $NbSe_2$, and $TaSe_2$. The goal is to help us have a comprehensive understanding of how CDW transition behaves in different systems, and what properties VSe_2 shares with, and differs from, its neighbors.

4.1 Electrical Resisitivity

Electrical resistivity is one of the transport properties that are directly affected by CDW. For VSe_2, earlier reports [64,80,83–88] showed a kink like anomaly in resistivity that is attributed to the CDW phase transition. The onset transition temperature (judged by the point where the resistivity starts to deviate from its original trend at higher temperature) varies depending on the sample used, which is reported to be near 110 K [83–85], 100K [86–88], 110 K-144 K [80] and 85K [64].

In this work, the electrical resistivity of VSe_2 single crystal was measured between 2 K and 400 K on a Quantum Design PPMS-6000 along the in-plane direction, while the electrical resistivity

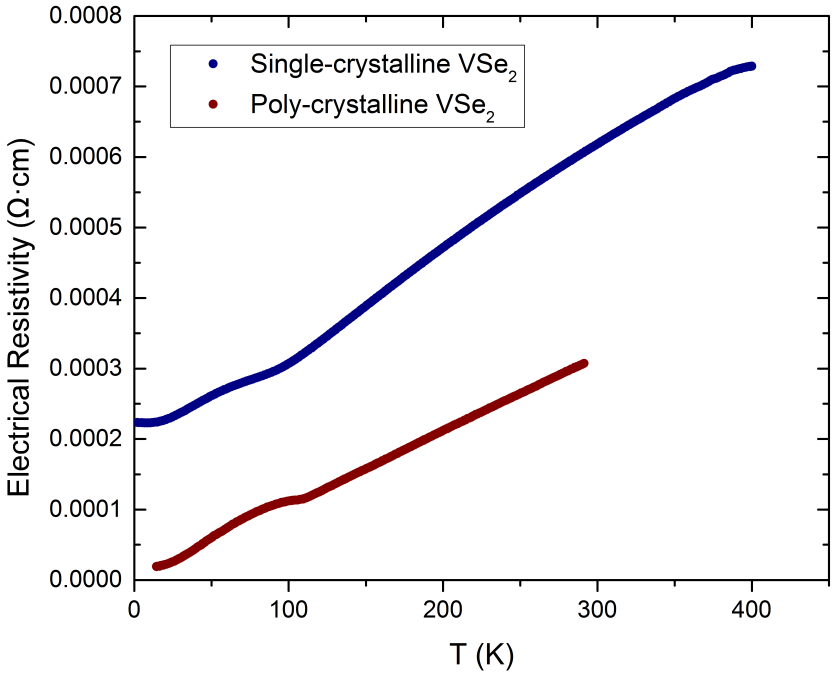

Figure 4.1: The electrical resistivity of single- and poly-crystalline VSe_2.

of poly-crystalline VSe_2 was measured between 14 K and 292 K on a homemade resistivity/Seebeck-coefficient ($R\&S$) apparatus [78]. Resistivity measurements on poly-crystalline VSe_2 were all along the direction perpendicular to the disk axis.

As shown in Fig. 4.1, the temperature dependencies of resistivity for both single- and poly-crystalline VSe_2 are very similar to each other. Metallic behavior is observed on both samples in a wide temperature range, which is consistent with the results of DFT calculations (cf. Chapter 2). It is worth noting that the large uncertainty in determining the sample thickness of VSe_2 single crystal makes the magnitude of resistivity less accurate, while its temperature dependence remains reliable, which is considered to be the reason of higher electrical resistivity found in VSe_2 single crystal. On the other hand, the residual-resistivity ratios (RRR) of single- and poly-crystalline VSe_2 are very different: for single-crystalline VSe_2, the RRR = 2.8; and for polycrystalline VSe_2, the RRR = 16. Standard RRR is the ratio of electrical resistivity at 300 K and 0 K, but as 0 K data is not feasibly accessible, in this calculation the measured resistivities at 2 K (for single-crystallline VSe_2) and 14 K (for poly-crystalline VSe_2) are used instead, which are the lowest temperatures the samples were measured. A higher RRR indicates a higher sample purity, so the single crystal is considered to

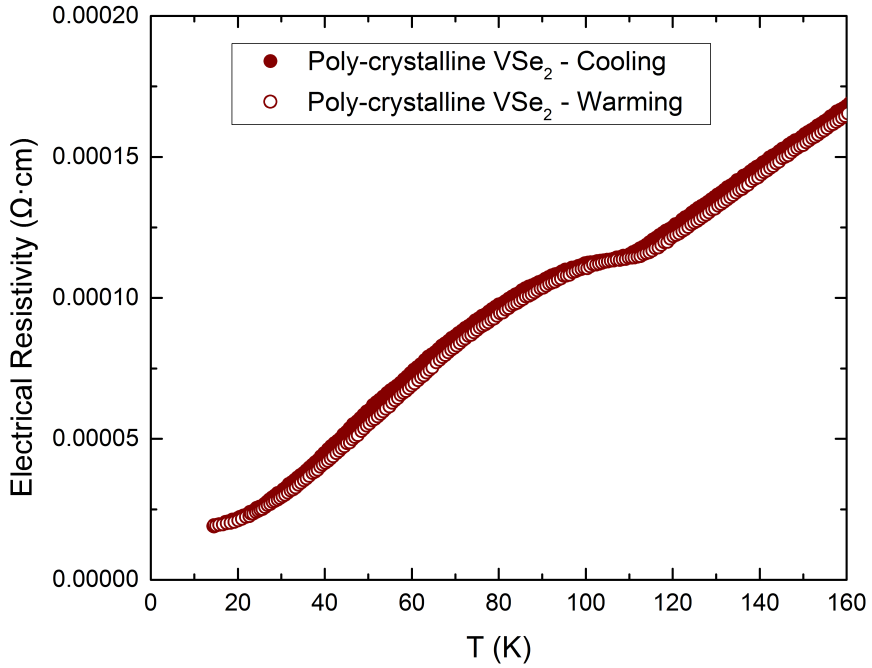

Figure 4.2: The electrical resistivity of poly-crystalline VSe_2 measured during cooling and warming. No discernible temperature hysteresis is found.

have more impurities, possibly due to the large temperature gradient applied during single crystal growth.

At around 110 K, the electrical resistivity of poly-crystalline VSe_2 shows a kink, and its temperature dependence noticeably changes from a linear behavior between 110 K and 300 K to a mild hump which ranges from 26 K to 100 K. This ∼110 K kink resembles the electrical resistivity anomaly induced by the CDW transition, as the CDW transition is accompanied with gap formation in the electronic structure. Below T_{CDW} the resistivity remains metallic, thus only a small fraction of conduction electrons are affected by the CDW gap.

Temperature dependence of resistivity of single crystal VSe_2 shows similar trend, but with a slightly lower transition temperature (∼100 K). It is known that T_{CDW} is dependent upon impurity concentration in materials. For instance, in 2H-$NbSe_2$, NMR measurement shows higher T_{CDW} on samples with higher RRR [93]. However, in 1T-VSe_2, the relation of T_{CDW} and RRR has been quite controversial, possiblily because the CDW in VSe_2 has a totally different pressure dependence comparing to other 1T and 2H polytypes, as the CDW transition moves to higher temperature when the pressure applied is increased [54]. Mutka and Molinie [88] reported that the CDW in VSe_2 is

suppressed (with lower T_{CDW}) in samples with lower RRR when defects were induced by electron-irradiation. In contradiction, in the study from Yadav et al. [80], highest T_{CDW} (∼144K) was found on samples with the lowest RRR (∼8), while the T_{CDW} in samples with higher RRR (15,16 and 28) is much lower (∼109 K-115 K). Their results seemed to indicate that impurities would facilitate the CDW transition like the effect of pressure [54]. In this work, T_{CDW} of single crystal VSe_2 (which has lower RRR compared to poly-crystalline sample) is about 10 K lower than the ∼110 K T_{CDW} of poly-crystalline VSe_2. This result supports the work from Mutka and Molinie [88], but is in contradiction with the conclusion made by Yadav et al. [80].

In addition, as shown in Fig. 4.2, there is no discernible temperature hysteresis under the CDW state found in the electrical resistivity of poly-crystalline VSe_2, between the values measured during cooling and warming. This result agrees with earlier reports, in which the hysteresis seems to appear only when the VSe_2 samples are heavily doped (with Fe) [85], of higher RRR (28) [80] or under higher pressure [54].

4.2 Seebeck Coefficient

Seebeck coefficient, whose definition and detailed explanations will be given in Appendix C, was also measured on both single- and poly-crystalline VSe_2 with the homemade R&S system [78], at temperature ranges of 10 K - 330 K and 14 K - 292 K, respectively. The single crystal was measured in the direction parallel to the ab-plane, while the poly-crystalline VSe_2 was measured along the direction perpendicular to disk axis. As Seebeck coefficient measurement is independent of the dimensions of sample, the measured result is not affected by the inaccuracy in single crystal size measurement.

As shown in Fig. 4.3, the observed Seebeck coefficients on single- and poly-crystalline VSe_2 are generally in good agreement with each other, and the results also agree well with previous reports from Yadav et al. [80,85,94], except that the Seebeck coefficient in their works were $8\% - 25\%$ smaller than that in this work. The magnitude and temperature dependence (except the anomaly around CDW transition temperature) of Seebeck coefficient are typical for metals, and the sign of Seebeck coefficient is positive in both single- and poly-crystalline VSe_2, indicates that hole conducting is dominant in the system. The fact that signs of Seebeck coefficient and Hall coefficient (cf. section 4.3) are opposite to each other is an indication of multi-band conducting behavior in VSe_2, which agrees

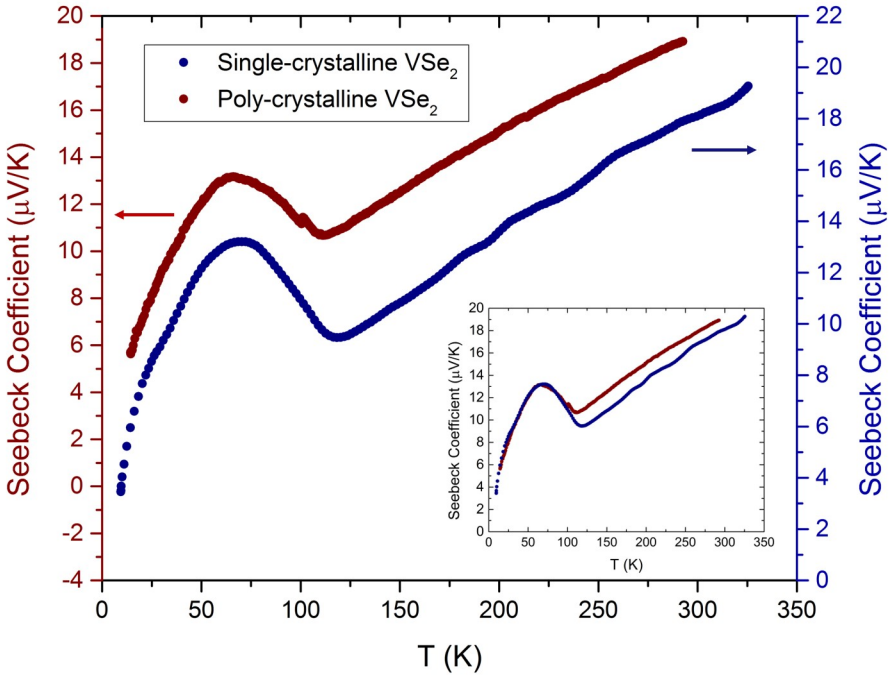

Figure 4.3: Seebeck coefficient of single- and poly-crystalline VSe_2.

well with the results of the DFT calculations (cf. Chapter 2).

The Seebeck coefficient of poly-crystalline VSe_2 reaches a local minimum at around 110 K, which is the same temperature of electrical resistivity anomaly. As temperature further decreases, the Seebeck coefficient starts to upturn, and subsequently reaches a local maximum at $\sim$ 66 K. At lower temperatures, it decreases again with temperature, but the slope of decreasing is sharper than it is above 110 K. As shown in Fig. 4.4, a distinct thermal hysteresis appears in the Seebeck coefficient between 60 K and 115 K, with the values measured during warming up to 1 $\mu V/K$ larger than that measured during cooling. The discontinuity observed in the cooling data around 100 K is artificial and of less importance.

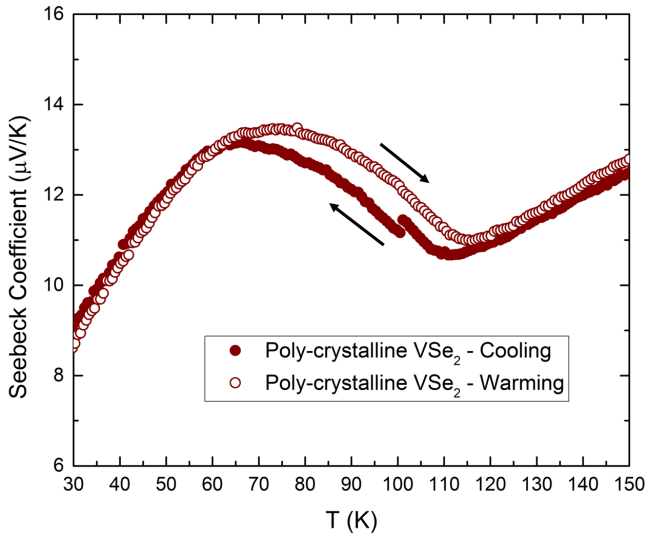

Figure 4.4: Temperature hysteresis found in the Seebeck coefficient of poly-crystalline VSe_2.

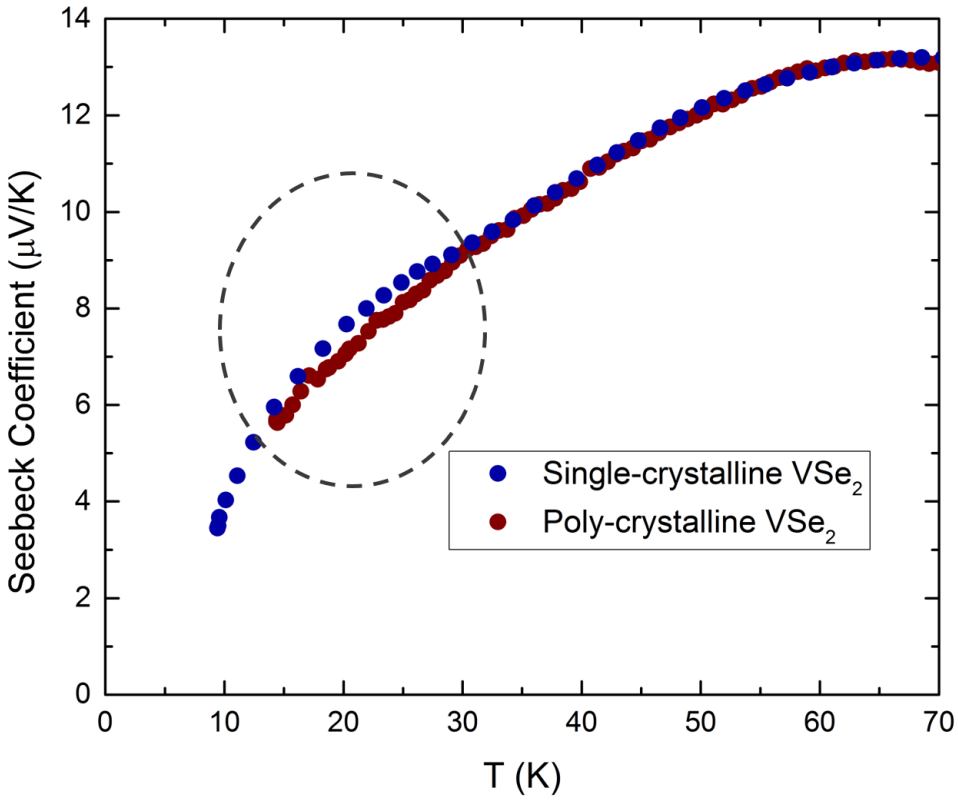

Figure 4.5: A hump presumably due to the phonon drag appears in the Seebeck coefficient of poly-crystalline VSe_2 below 35 K.

The behavior of Seebeck coefficient in VSe_2 single crystal is very similar to that in the poly-crystalline sample, but with the local temperature minimum $\sim$ 8 K higher than 110 K, and there is also an additional weak hump centered around 20 K in VSe_2 single crystal, as shown in Fig. 4.5. In contrast, in the Seebeck coefficient of poly-crystalline VSe_2, the hump is either non-existed/much weaker or shifted to much lower temperature that hasn't been measured. Similarly, in a previous report from Yadav et al. [80], a similar hump has been observed in the Seebeck coefficient of VSe_2 single crystal, but not in the poly-crystalline VSe_2. This hump might be attributed to the phonon drag effect. Generally, the phonon drag effect is weaker in poly-crystalline materials comparing to their single crystal counterparts, due to the fact that phonon drag effect is sensitive to the electronic mean free path, which is limited by the grain boundaries [95]. The phonon drag hump observed in VSe_2 indicates the strong electron-phonon coupling in the system, which is considered as the prerequisite for CDW transition.

The increase of Seebeck coefficient between 118 K/110 K (for single-/poly-crystalline VSe_2) and $\sim$66 K, along with the rapid drop of Seebeck coefficient below $\sim$66 K, are regarded as the results of partially gapped Fermi surface. As mentioned in Appendix C, the sliding density wave mode carries no entropy, analogous to the situation in superconducting system where Cooper pair has zero entropy. However, in CDW materials, sliding density wave mode rarely exists, and the CDW condensates still carry entropy. The impact of CDW on Seebeck coefficient include: (1) The energy gap formed by Fermi surface nesting introduces gapped excitation into charge transportation. (2) Electronic band structure change caused by lattice distortion can affect Seebeck coefficient via multiple channels, e.g., change in DOS, change in the energy dependence of DOS, etc. (3) Possible change in scattering mechanisms. The increase in Seebeck coefficient below 118 K/110 K is presumably caused by the gap formed in the electron-like band, which is the V $3d_{z^2}$ band in VSe_2. Besides, the rapid drop of Seebeck coefficient below $\sim$66 K can be regarded as due to the gap formed in the hole-like band, which is the Se 4p band in VSe_2. The crossover in the Seebeck coefficient across $\sim$66 K and the thermal hysteresis between cooling and warming found in the Seebeck coeffient starting at almost the same temperature, are both indications of a possible lock-in CDW phase transition in VSe_2 at $\sim$66 K, even though the underling origin of the transition is still unclear.

4.3 Hall Measurements

Temperature dependent Hall coefficient measurement was conducted on the single-crystalline VSe_2 using the Quantum Design PPMS-9, and the result is shown in Fig. 4.6. As VSe_2 is a metal with high carrier concentration, its Hall coefficient is quite small, which makes it more difficult to be measured, and the accuracy of results is largely affected by the uncertainties in measurements. Precise Hall coefficient of poly-crystalline VSe_2 is even harder to obtain, owing to its larger sample thickness and a multitude of grain boundaries comparing with single crystal. So in this work, only the Hall coefficient measured on the single-crystalline VSe_2 is represented.

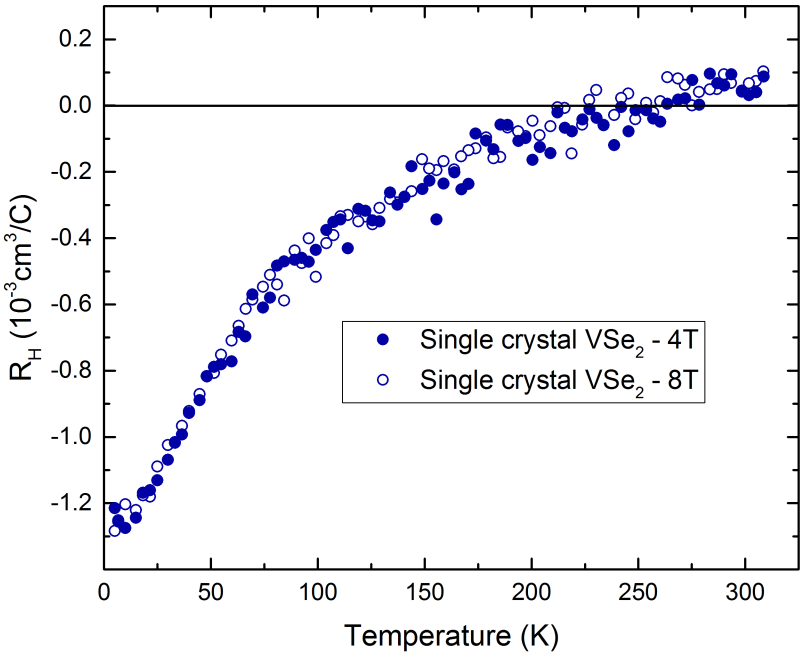

Figure 4.6: Hall coefficient of single- and poly-crystalline VSe_2.

For the VSe_2 single crystal, the applied external magnetic field was 4 T and 8 T, and the corresponding results are almost identical to each other. As temperature goes up to around 225 K, the sign of Hall coefficient R_H changes from negative to positive, indicating the primary charge carrier changes from electrons (V $3d$) to holes (Se $4p$). This observation also confirms that

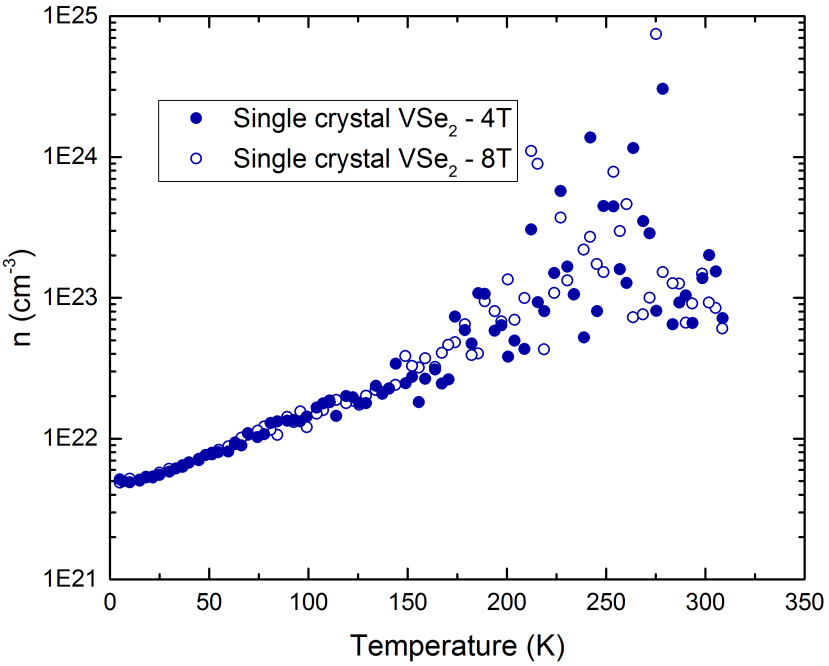

Figure 4.7: Carrier concentration of single- and poly-crystalline VSe_2.

VSe_2 is a multi-band conductor, which agrees with the calculated electronic band structure (cf. Chapter 2). Unlike the previous literature results [64, 80, 86, 88], the decrease of Hall coefficient of single-crystalline VSe_2 when entering the CDW state is much less sharp, and the temperature with the most significant change of slope is about 80 K, which is much lower than the temperatures of observed anomalies in the resistivity and Seebeck coefficient. This inconsistency is likely due to the off-stoichiometry of samples, which is rather difficult to avoid in VSe_2.

The sign of Hall coefficient in VSe_2 is opposite to the sign of Seebeck coefficient. The difference in the sign can be attributed to the presence of two types of carriers with very different mobility [96, 97], as the Hall coefficient is more significantly dependent on mobilities of the carriers. The change in the sign of the Hall coefficient at ~225 K is possibly due to the different temperature dependence of electrons and holes. A similar sign change has also been observed in other CDW materials.

Fig. 4.7 and 4.8 show the corresponding carrier concentration and mobility of single-

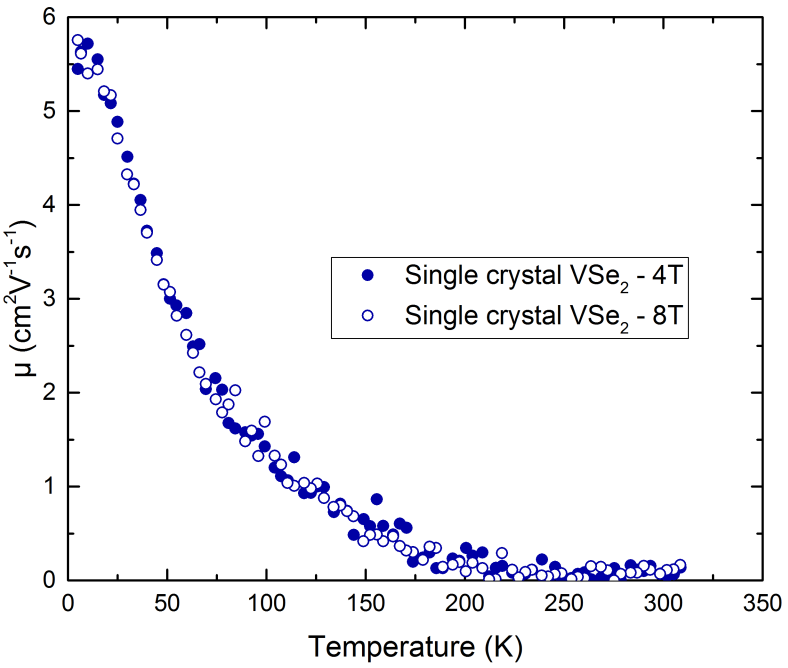

Figure 4.8: The Hall mobility of single- and poly-crystalline VSe_2.

crystalline VSe_2, calculated from the equations $n = \frac{1}{R_H q}$ and $\sigma = n|q|\mu$. It is worth noting that the carrier concentration was calculated with a single band model, thus the calculated carrier concentration is merely a semi-quantitative result. As temperature increases, more phonons modes are excited, resulting in a reduction in the carrier mobility. The dominant scattering mechanism can be obtained from the temperature dependence of mobility: mobility due to acoustic phonon scattering behaves as $T^{-3/2}$, while optical phonon scattering has a mobility of $T^{-1/2}$ dependence, and charged defects gives a $T^{3/2}$ dependence [98, 99]. In this work, the carrier mobility of single-crystalline VSe_2 decreases with increasing temperature in almost all temperature range measured, indicating the dominance of phonon scattering even at very low temperatures.

Hall angle was also calculated based on the Hall coefficient measured (under magnetic field of 8 T) and the electrical conductivity of single-crystalline VSe_2. Hall angle is defined as

$$\theta_H = \arctan\left(\frac{E_y}{E_x}\right),$$

where

$$E_x = \frac{RI}{L} = \frac{\left(\frac{1}{\sigma}\frac{L}{tw}\right)(jtw)}{L} = \frac{1}{\sigma} j_x$$

and

$$E_y = R_H j_x B_z.$$

Here R, I, σ, L, t, w, R_H, j_x, B_z are electrical resistivity, current, electrical conductivity, length, thickness, width, Hall coefficient, current density, and magnetic field strength, respectively. Thus, $tan\theta_H$ is directly proportional to external magnetic field strength and carrier mobility [100, 101], as

$$\tan\theta_H = \frac{R_H j_x B_z}{j_x/\sigma} = \sigma R_H B_z = \mu B_z.$$

Below 145K, $cot(\theta_H)$ changes almost linearly with temperature squared. Fit $cot(\theta_H)$ with equation

$$\cot(\theta_H) = {\omega_c}^{-1}\tau_H = \alpha T^2 + C,$$

where $\omega_c = \frac{eB}{m_s}$ and m_s is the effective mass. Here α sets the energy scale for the spinon-spinon scattering, and C describes in-plane impurity scattering rate [100,102]. In a system with no impurity, C should be zero. From the fitting result, $\alpha = 0.0729K^{-2}$ and $C = 2.14$, indicating the sample

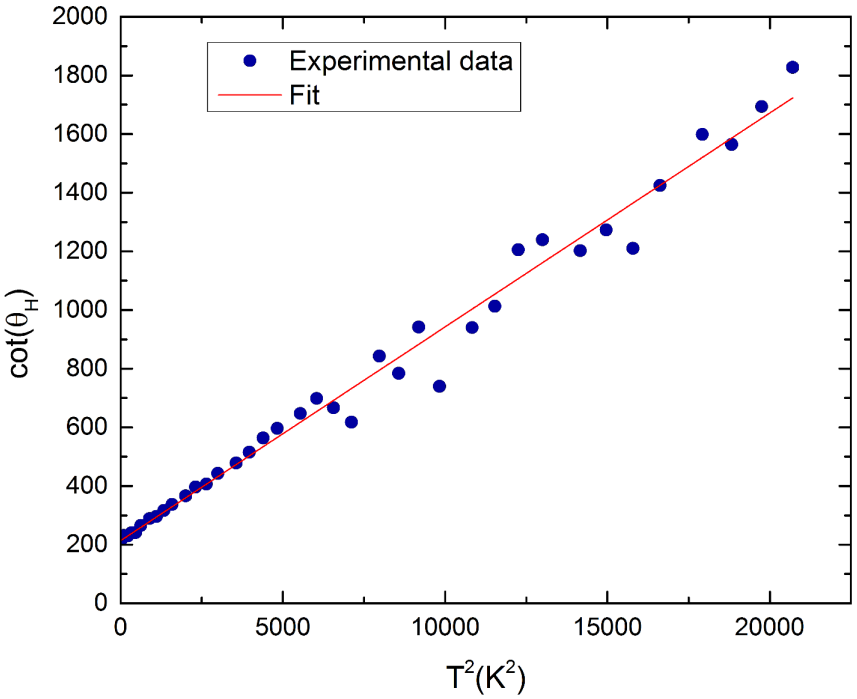

Figure 4.9: $cot\theta_H$ vs. T^2 plot derived from Hall coefficient and electrical conductivity measurements of single-crsytalline VSe_2, showing a linear relationship

contains a certain amount of impurities.

Due to the difficulty and uncertainty of the Hall measurement in VSe_2, it is hard to quantitatively study the CDW phase transition. Nonetheless, the fact that carrier concentration has no evident anomaly near 110 K is still consistent with the conjecture that only a small portion of Fermi surface is involved in the CDW transition.

4.4 Magnetic Susceptibility

VSe_2 is an interesting candidate for magnetic study. It has a natural tendency to grow V rich, with excess V taking sites in the van der Waals gap [54], and its macroscopic magnetic properties is sensitive to the amount of V interstitials. Despite that VSe_2 in the monolayers [103], T-nanotubes/H-nanotubes [104] and nanosheets [105] forms are regarded as ferromagnetic, bulk 1T-VSe_2 is generally considered as non-magnetic, with the energy of ferromagnetic state slightly lower [75]. In addition, the concentration of V excess can be estimated by the magnetic susceptibility measurements [54], thus magnetic measurement also provides information about the off-stoichiometry of the material.

In this work, magnetic susceptibility χ of VSe_2 single crystals was measured on Quantum Design MPMS from 2 K to 300 K, under an external magnetic field of 1 T applied both parallel with and perpendicular to the c-axis of VSe_2. Measurement was also seperately performed under magnetic fields of 0.1 T, but there is hardly any difference found in the magnetic susceptibility when magnetic field varies.

Temperature dependent magnetic susceptibility χ is illustrated in Fig. 4.10, in directions parallel to ab-plane and c-axis, respectively. The values measured when the exteranl magnetic field is along the ab-plane are lower, and the anistropy of susceptibility doesn't seem to be strong, which is good agreement with the result from Bruggen and Haas [87]. As suggested in previous reports [61, 83, 88, 106], low temperature magnetic susceptibility can be adequately fitted as

$$\chi = \chi_0 + \frac{C}{T - \Theta}$$

Here the $\frac{C}{T-\Theta}$ is the Curie paramagnetism contribution, where C is the Curie constant and Θ is the effective interaction temperature indicating interactions between local moments. The χ_0 is a term that can be approximately treated as temperature independent, which consists of three

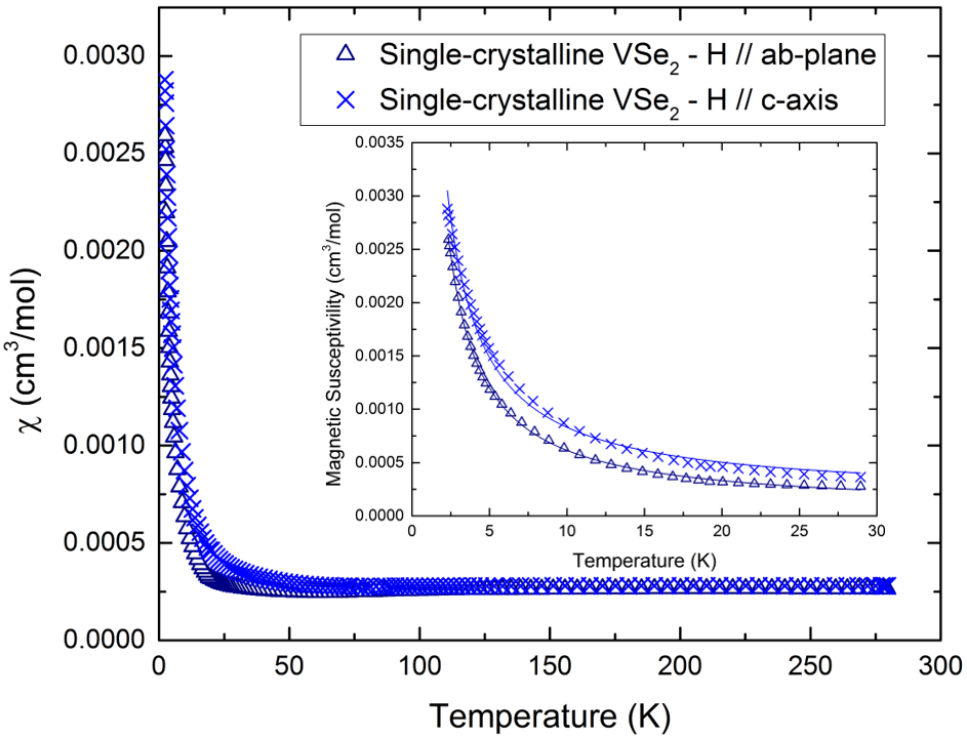

Figure 4.10: Magnetic susceptibility of single-crystalline VSe_2. Triangle and cross are the measured magnetic susceptibility measured with magnetic field applied along the ab-plane and c-axis, respectively. The insect shows the low temperature Curie tail, fitted with a Curie-like term (contributed to free paramagnetic V interstitials) and a temperature independent term.

	C (cm^3K/mol)	Θ (K)	χ_0 ($10^{-4}cm^3/mol$)
$H \parallel ab-plane$	0.0055	0.2	0.53
$H \parallel c-axis$	0.00655	0	1.8

Table 4.1: Calculated Curie constant C, effective interaction temperature Θ and temperature independent term χ_0 of VSe_2.

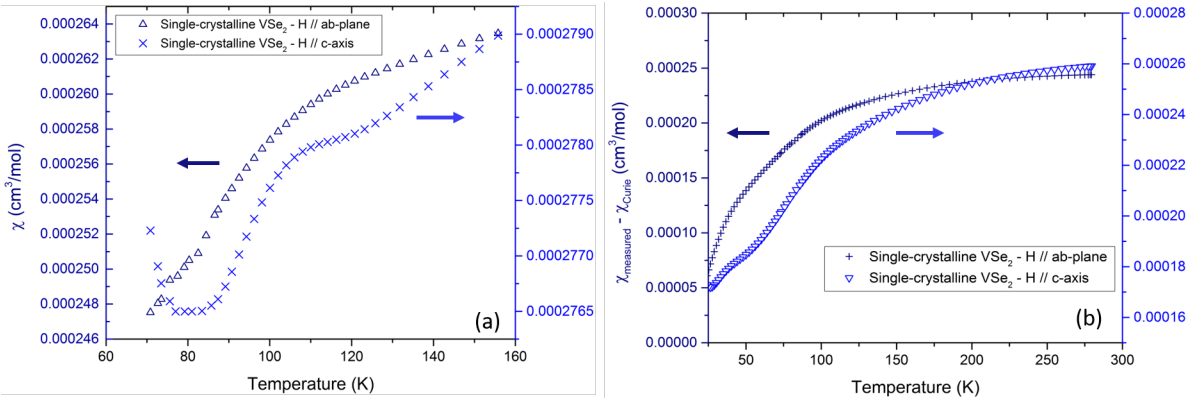

Figure 4.11: Magnetic susceptibility anomaly of single-crystalline VSe_2 near the CDW transition. (a) The measured magnetic susceptibility shows a bump near 110 K. (b) The magnetic susceptibility contributed by the layeres (reflected by $\chi_{measured} - \chi_{Curie}$) drops smoothly at 110 K.

terms: the Pauli paramagnetic term that arises from the conduction electrons, the Landau and core diamagnetism term, and the van Vleck term [107]. Parameters derived from the fitting are summarized in table 4.1.

The small and neglible Θ values indicate almost no inter-local magnetic moment coupling, as such, spontaneous magnetism phase transition to ferromagnetic state is hardly attainable. The Curie constant can be used as an indicator to the amount of excess V (the value of x in $V_{1+x}Se_2$). Assuming the effective moment per interstitial V is $2.5\mu_B$ [64, 108], $x = 0.6\%$ and 0.8% can be calculated out from the C values with magnetic field along the ab-plane and c-axis, respectively, following the calculations introduced by Friend and Jerome [54].

The Curie term is assumed to be unaffected by the CDW transition. On the other hand, the Pauli paramagnetism term is generally regarded as temperature independent, and it is proportional to the DOS at the Fermi surface, thus it can be stongly affected by the CDW wave transition [106]. As illustrated in Fig. 4.11(a), a bump is observed in the measured magnetic susceptibility when the temperature decreases to the onset CDW transition temperature 110 K (and the bump is more obvious when the external magnetic field is applied along the c-axis). Contributions from the Pauli

paramagnetism, the Landau diamagnetism and the van Vleck paramagnetism are difficult of be clearly separated, but the difference between the measured susceptibility $\chi_{measured}$ and the Curie tail χ_{Curie} can be used as an indicator to the susceptibility without the contribution from the V interstitials. As shown in Fig. 4.11(b), the $\chi_{measured} - \chi_{Curie}$ drops smoothly across the CDW transition, while in earlier reports [64, 88, 106], the drop is much sharper. The decrease can be attributed to the change in DOS at Fermi surface due to CDW gap. The small change also indicates the weak CDW in VSe_2.

4.5 Heat Capacity

The heat capacity of VSe_2 single crystals were measured from 2 K to 200 K with the Quantum Design PPMS-6000, and heat capacity of poly-crystalline VSe_2 was measured at 0.3 K-15 K, 2 K-300 K and 350 K-600 K using NETZSCH-DSC 404, Quantum Design PPMS-9 (at Wuhan University of Technology, Wuhan) and a ^{3}He cryostat with thermal relaxation method (at Institute of Physics, Academia Sinica, Taipei), respectively. The molar heat capacity c *vs.* temperature data are ploted in Fig. 4.12. In general, the values of heat capacity of both single- and poly-crystalline VSe_2 coincide well with each other and the only previous report from Yadav et al [80].

The measured high temperature c (only taken on poly-crystalline VSe_2) exceeds the Dulong-Petit limit 74.8 $Jmol^{-1}K^{-1}$ starting from ∼250 K. The ∼500 K peak in heat capacity of poly-crystalline VSe_2 is considered to be attributed to residual Se, as the melting point of Se is 494 K, even though there are no Se peaks found in XRD results. Repeating the measurement shows peak at the same temperature, confirming the existence of residual Se in the sample.

As shown in inset plot in Fig. 4.12, poly-crystalline VSe_2 shows a very weak kink in heat capacity across the CDW phase transition. However, the kink in the heat capacity of VSe_2 single crystal is even weaker, and the position of the hump seems to be shifted down to ∼ 95 K. This is generally in good agreement with the measurement taken on single crystal flake(s) by Yadav et al. [80], but the kink in their measurement is more noticeable.

4.5.1 Calculating the Amount of Residual Selenium

The amount of residual selenium inside the poly-crystalline VSe_2 sample can be estimated by calculating the enthalpy change across the 500 K peak of molar heat capacity. As shown in

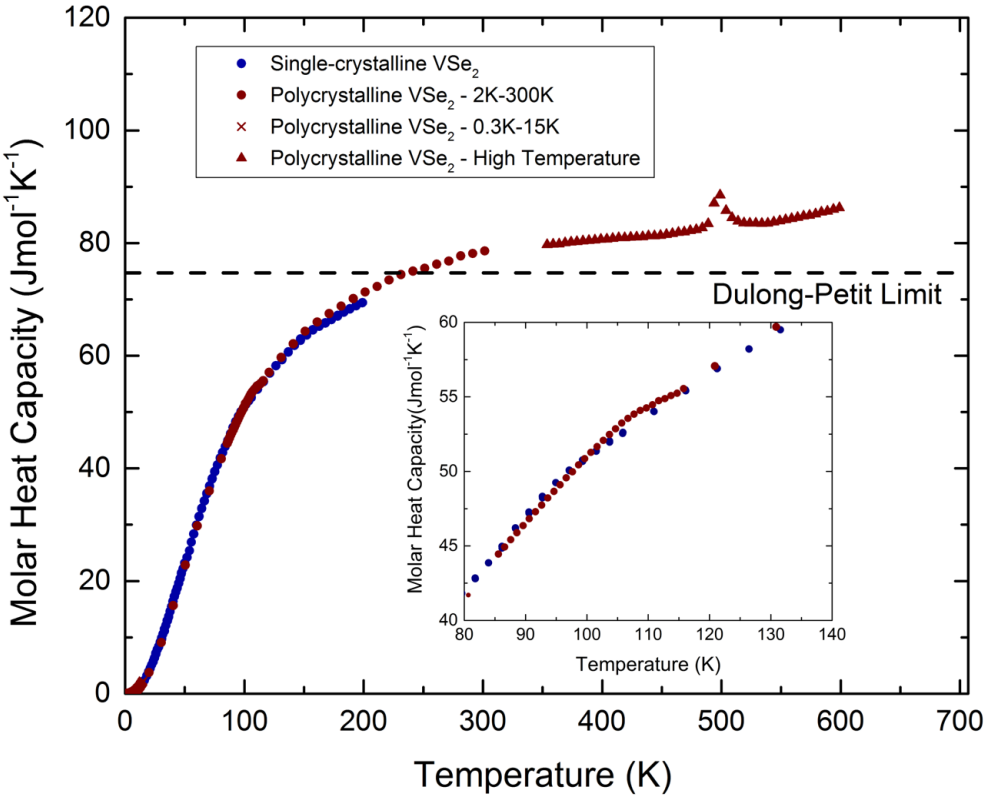

Figure 4.12: Molar heat capacity of single- and poly-crystalline VSe_2.The dashed line indicates Dulong-Petit limit.

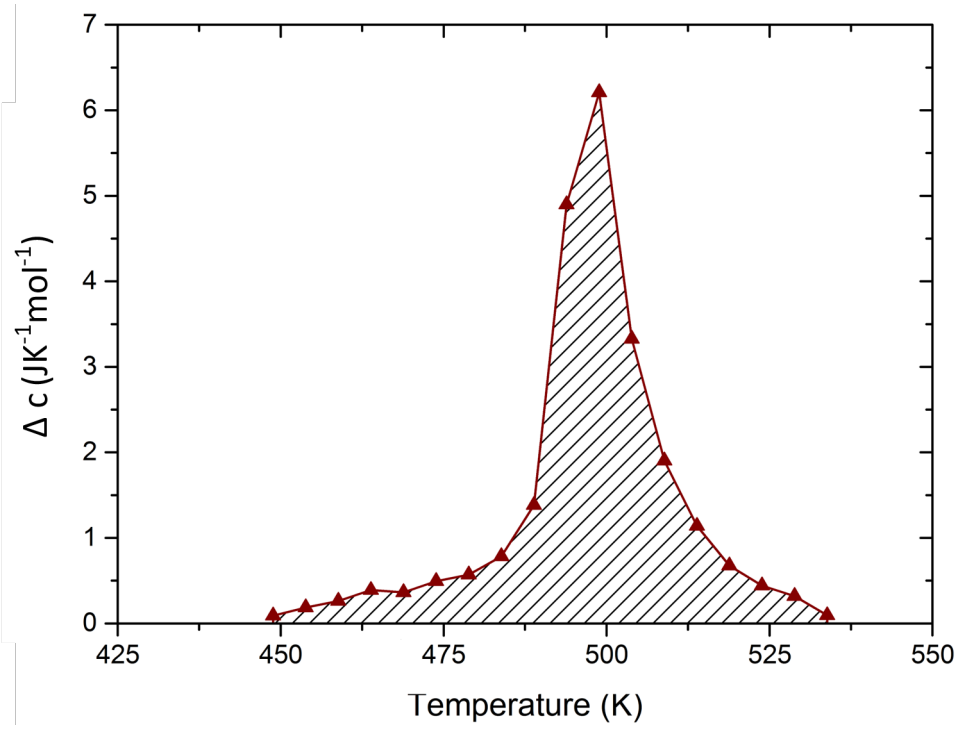

Figure 4.13: The heat capacity peak centered at ∼500 K, extracted from Fig. 4.12. The peak is due to selenium melting, and the shaded area is used to calculate the enthalpy change across the selenium melting point.

Fig. 4.13, the extracted peak, which is derived by subtracting the fitted baseline without considering the peak from the measured values, covers an area of 117.2 J/mol, which corresponds to the enthalpy change of selenium. The latent heat of selenium is 61 kJ/kg, which is 4818 J/mol. Thus the molar concentration of selenium in poly-crystalline VSe_2 is around 2%.

4.5.2 Low Temperature Heat Capacity Fitting

To investigate the electronic contribution to molar heat capacity, the linear part of molar heat capacity at low temperatures was fitted using Debye-Sommerfeld expression $c = c_{electronic} + c_{lattice} = \gamma T + \beta T^3$, where the first and second term represent the electronic and phononic specific heat, respectively. The fitting results for single- and poly-crystalline VSe_2 are close to each other, as shown in Fig. 4.14. The upturn in c/T at ultra-low temperature region, which is observed in both single- and poly-crystalline VSe_2, deviates from the Debye-Sommerfeld model, and is not considered in the fitting. The possible origin of this behavior will be further discussed in details in section 4.8.

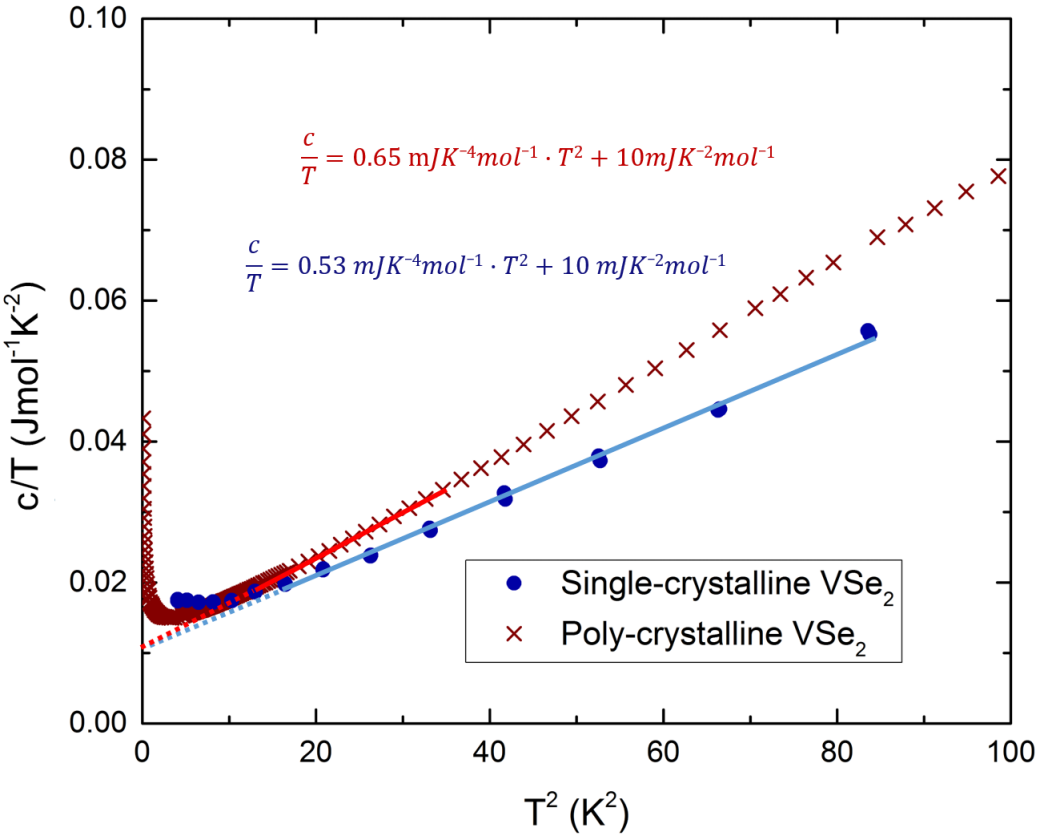

Figure 4.14: c/T vs. T^2 for both single- and poly-crystalline VSe_2 at low temperatures. The solid lines are the fitting trendlines using Debye-Sommerfeld equation, and the dashed lines are their extensions showing almost the same γ value.

For poly-crystalline VSe_2, the γ and β derived from the fitting are 10 $mJK^{-2}mol^{-1}$ and 0.65 $mJK^{-4}mol^{-1}$, respectively. With equation $\beta = \frac{12\pi^4}{5} nN_A k_B \Theta_D^{-3}$, where n is the number of atoms in a molecule, the Debye temperature Θ_D was found to be 210 K. Similarly, γ, β and Θ_D for VSe_2 single crystals are 10 $mJK^{-2}mol^{-1}$, 0.53 $mJK^{-4}mol^{-1}$ and 220 K, respectively.

4.5.3 Heat Capacity Anomaly Near T_{CDW}

As shown in Fig. 4.12, a weak but discernible hump is found in the heat capacities of single- and poly-crystalline VSe_2, near the CDW transition temperature. In the single-crystalline sample, the hump appears to be weaker and at lower temperature ($\sim 95K$), and the entropy change across the CDW transtion is difficult to be obtained. In poly-crystalline VSe_2, the hump is more distinct. The heat capacity change Δc is derived by subtracting the fitting baseline (illustrated as a red spline

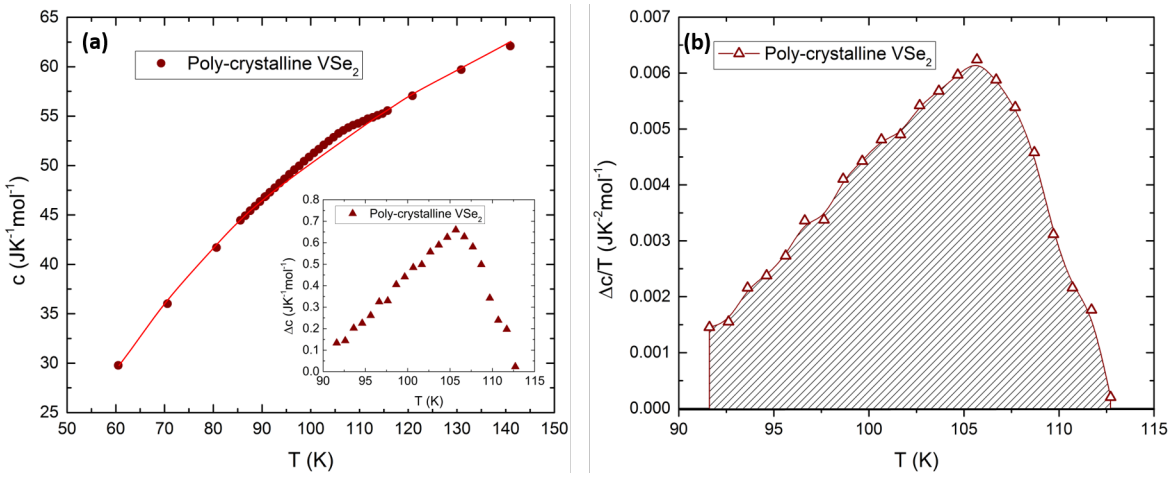

Figure 4.15: Excess molar heat capacity around 95K.

in Fig. 4.15(a)) from the measured heat capacity. The Δc features a wide hump centered at $\sim$ 106 K, as illustrated in the inset of Fig. 4.15(a), which is consistent with the conclusion of second-order phase transition of VSe_2 from the normal state to the incommensurate CDW state [57, 59, 62, 63]. $\Delta c/T$ vs. T is plotted in Fig. 4.15(b), in which the shaded area is regarded as the entropy change ΔS involved in the CDW transition. The derived ΔS is $\sim 0.081\ JK^{-1}mol^{-1}$. On the other hand, with the obtained γ value, the expected entropy change is $S = \gamma T \sim 1.1\ Jmol^{-1}K^{-1}$. Thus there is about $\Delta S/(\Delta S + S) \sim 7.6\%$ of the total Fermi surface involved in the CDW phase transition, and this value is relatively very small in CDWs. Nonetheless, the heat capacity measurements of both single- and poly-crystalline VSe_2 show that the CDW in VSe_2 is very weak.

4.6 Thermal Conductivity

The total thermal conductivity of single crystal VSe_2 measured along the ab-plane, at temperatures from 10 K to 305 K, by the custom designed parallel thermal conductance (PTC) apparatus [79]. Correspondingly, total thermal conductivity of poly-crystalline VSe_2 from 26 K to 322 K was measured in a direction perpendicular to the disk axis, by a custom designed thermal conductivity measurement system [81]. Both systems are based on a steady state method.

The total thermal conductivity κ is contributed by both lattice and electrons, which could be expressed as $\kappa = \kappa_l + \kappa_e$, where κ_l and κ_e are the lattice and electron parts of thermal con-

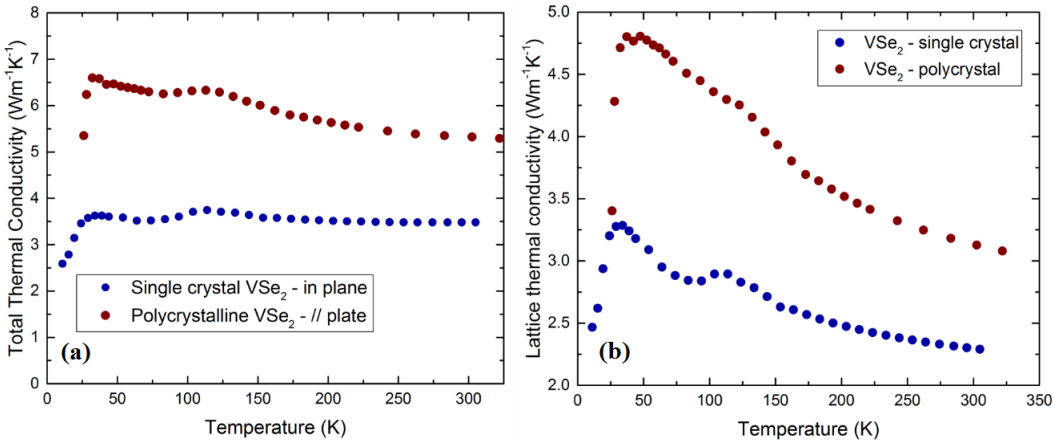

Figure 4.16: (a) Total thermal conductivity and (b) lattice thermal conductivity of single- and poly-crystalline VSe_2 below room temperature.

ductivity, respectively. The electronic contribution of thermal conductivity κ_e was estimated using Wiedemann-Franz relation $\kappa_e = L\sigma T$, where the Lorenz number $L = \frac{\pi^2}{3}(\frac{k_B}{e})^2$, and σ is the electrical conductivity, which is the inverse of electrical resistivity that was introduced in section 4.1. The Wiedemann-Franz relation was originally used to describe the electronic thermal conductivity in Fermi liquids, and is violated in various materials such as optimally electron-doped cuprate [109]. Despite that VSe_2 shows a metallic behavior, the validation of Wiedemann-Franz relation in such system still needs to be justified. Nonetheless, the estimated lattice thermal conductivity was derived by subtracting the electron contribution from the observed total thermal conductivity. To eliminate the radiation effect, corrections were conducted on the total thermal conductivity and lattice thermal conductivity presented, following procedures given in ref. [79, 81].

The total thermal conductivity and lattice thermal conductivity of both single- and poly-crystalline VSe_2 are shown in Fig. 4.16. Some noteworthy features are: (1) Poly-crystalline VSe_2 shows a higher thermal conductivity for both total and lattice. (2) Both samples exhibit low thermal conductivity, comparing with typical metals. (3)In the total/lattice thermal conductivity of both samples, there is a very asymmetric peak at 35K, which is a characterization of crystalline materials, caused by crossover of dominant scattering mechanisms. (4) Around 110 K, both the total and lattice thermal conductivity show anomalies at around 118 K, which could be possibly due to the phonon softening caused by Kohn anomaly effect. This behavior resembles other CDWs, as will be discussed in section 4.7.

4.7 In Comparison with Other CDW Materials

In this section, the experimental results of 1T-VSe_2 will be compared with three other selected materials: $NbSe_3$, 2H-$NbSe_2$, and 2H-$TaSe_2$. The goal is to develope a comprehensive understanding of how CDW transition behaves in different systems, and what properties VSe_2 shares with, and differs from, its neighbors. These three materials are selected owing to the facts that: (1) $NbSe_3$ is one of the most intensively studied quasi-1-D CDW materials, while the other three are all 2-D structured; (2) $NbSe_2$ and $TaSe_2$, together with VSe_2, are the only three in chemical table group VB di-selenide materials. All these three materials have CDW transitions below room temperature, and have been intensively studied. It is worth noting that $NbSe_3$ and $TaSe_2$ both have two CDW transitions (for $NbSe_3$, $T_{CDW} = 58$ K, $T_{lock-in} = 142$ K; for $TaSe_2$, $T_{CDW} = 90$ K and $T_{lock-in} = 120$ K), so both transitions will be taken into account. Here the $T_{lock-in}$ indicates the temperature for lock-in CDW transition. Also, for $NbSe_3$, it was found that about 20% of the Fermi surface at room temperature is destroyed by the 142 K CDW transition and approximately 60% of the remaining part by the 58 K transition [110].

From all comparisons in electrical resistivity, Seebeck coefficient, Hall coefficient, heat capacity and thermal conductivity, it can be seen that the CDW transition in TMDC materials behaves quite differently from $NbSe_3$, which is a typical quasi-1-D CDW material. Moreover, among the three group VB di-selenides, the behavior of CDW transition in VSe_2 is very different from the other two compounds.

4.7.1 Electrical Resistivity

Fig. 4.17 compares the change in electrical resistivity near CDW transitions in the selected materials. It can be clearly seen that the quasi-1-D CDW material $NbSe_3$ has a much more distinct anomaly across transition point, while in the other three quasi-2-D materials, the hump below T_{CDW} is either very mild, or even not discernible. Similar phenomena have been observed in other CDW materials. Moreover, among the three group VB di-selenides, VSe_2 seems to have the more distinct anomaly than the other two materials. From the results it is plausible to argue that the mechanism of CDW transition in the three group VB TMDCs might be different from that in $NbSe_3$, which is a typical quasi-1-D CDW. Indeed, X. Zhu et. al. [35] suggested to classify CDW into at least three types: Type-I is quasi-1-D systems originating from Peierls instability (Fermi surface nesting); type

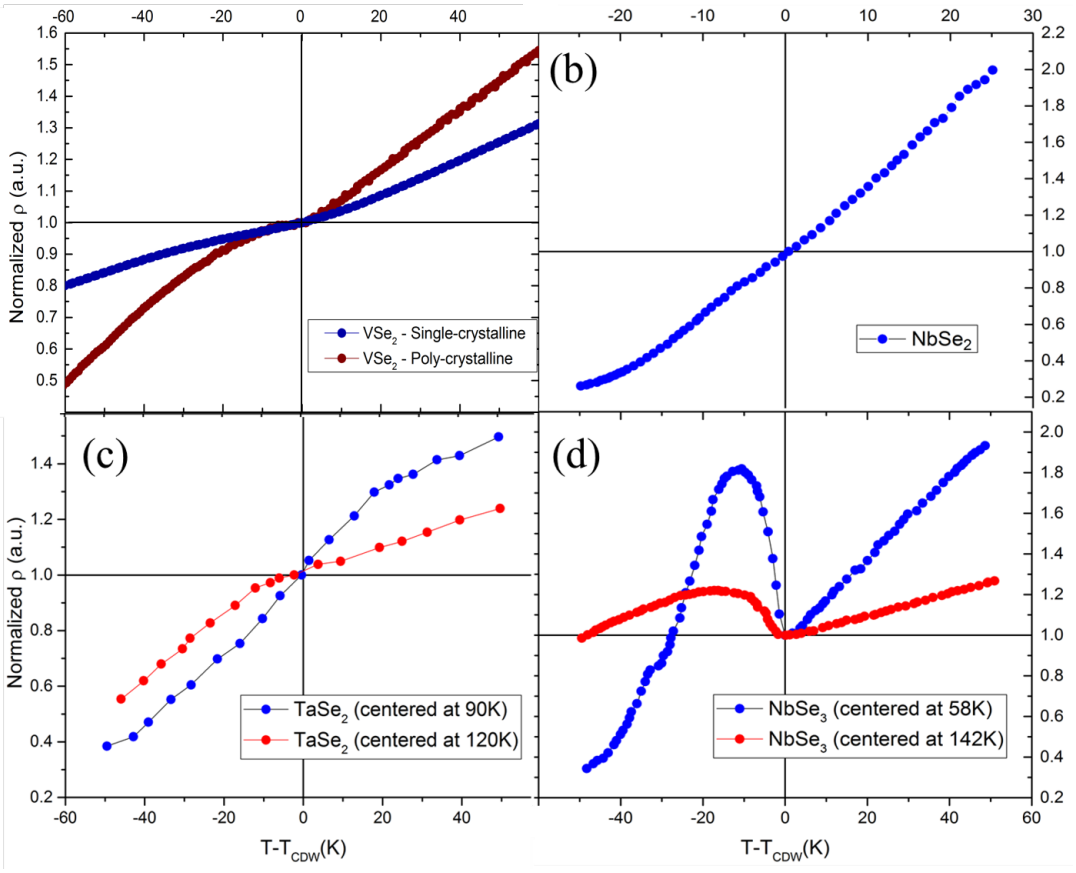

Figure 4.17: Electrical resistivity near CDW transition temperature of (a) single and poly-crystalline 1T-VSe_2, (b) 2H-$NbSe_2$ [111], (c) 2H-$TaSe_2$ [111] and (d) $NbSe_3$ [112]. Note that $TaSe_2$ and $NbSe_3$ both have two CDW transitions at different temperatures.

II CDWs are driven by electron-phonon coupling, and $NbSe_2$ was used as an example in their paper; type III CDWs are systems with no indication of Fermi surface nesting or electron phonon coupling, such as cuprates which exhibit charge modulation phenomena. While there are still controversies over the origin of CDW transitions, the resistivity results may suggest the different mechanisms in quasi-2-D (Nb,V,Ta)Se_2 and some quasi-1-D CDWs.

4.7.2 Seebeck Coefficient

Fig. 4.18 shows the Seebeck coefficients of the four CDW materials near their transition temperatures. There are several differences between VSe_2 and the other three systems.

Firstly, among the three group VB TMDCs, VSe_2 has the highest Seebeck coefficient, about

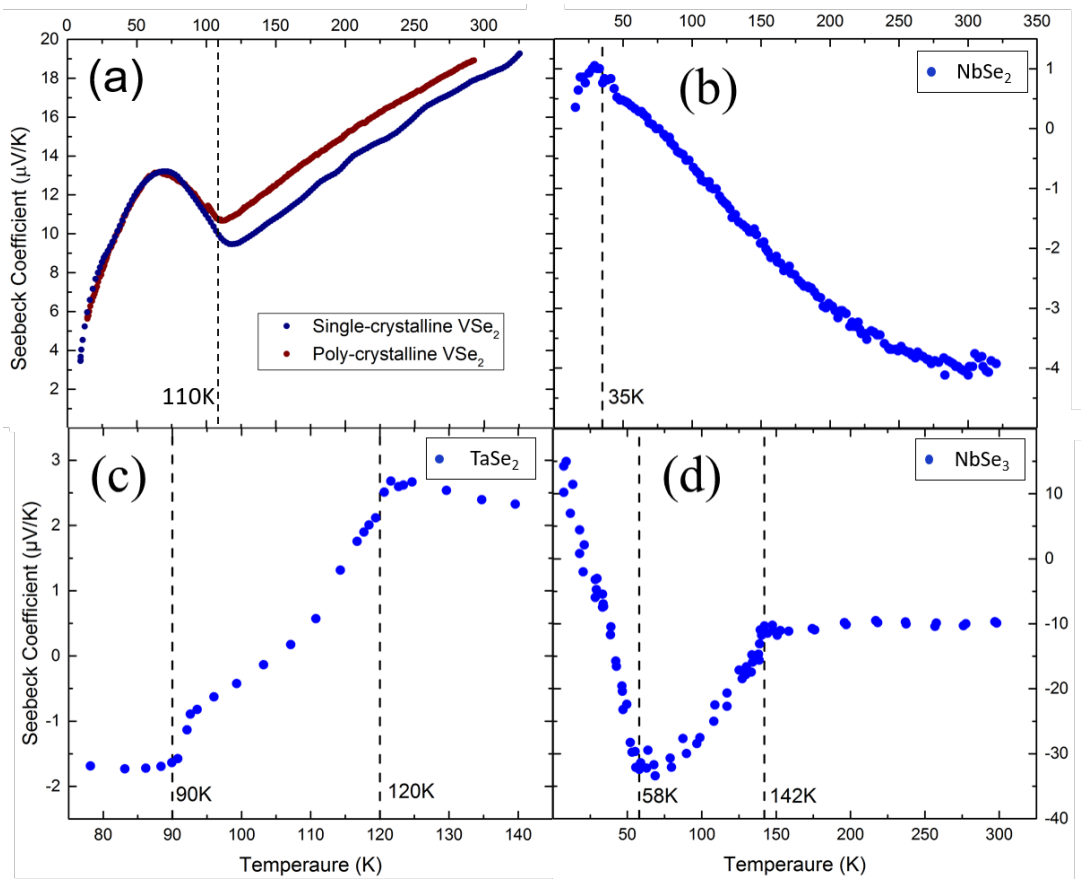

Figure 4.18: Seebeck coefficient near the CDW transition temperature of (a) single- and poly-crystalline VSe_2, (b) $NbSe_2$ [113], (c) $TaSe_2$ [114] and (d) $NbSe_3$ [115]. The vertical dashed lines indicate CDW transition temperatures.

ten times greater than $NbSe_2$ and $TaSe_2$, and is close to that in $NbSe_3$. As the Seebeck coefficient usually indicates heavier electron effective mass (see Appendix C), so the carriers in VSe_2 are likely much heavier. Another possibility is that the holes in VSe_2 are predominant, while in $NbSe_2$ and $TaSe_2$, the contribution from electrons is nontrivial, as the signs of Seebeck coefficient for electrons and holes are opposite. This can be also seen from the fact that only VSe_2 doesn't show a sign change below room temperature. Additionally, all three materials (Fig. 4.18(a)(c)) show a quasi-linear temperature dependence, consistent with the metallic nature of the systems.

More importantly, the behaviors of the CDW anomaly of the four materials are quite different. For CDW transitions in VSe_2 and $NbSe_3$ (the one at 142K), there is an upturn followed by a hump below T_{CDW} (note that Seebeck coefficient of $NbSe_2$ is negative). For CDW transitions in

$NbSe_2$, $TaSe_2$ (the one at 120 K) and $NbSe_3$ (the one at 58 K), Seebeck coefficient reaches a local maximum at T_{CDW}. This could be interpreted by the fact that during CDW transitions, part of the charge carriers are gapped, leading to a increase in Seebeck coefficient in the type of the gapped carriers. The mechanism resembles the Seebeck coefficient in semiconductors, the details can be found in Appendix C. For instance, as elaborated by P.M. Chaikin et al. [115], the increase at 142 K in $NbSe_3$ (Fig. 4.18 (d)) is due to a gap with hole-like carriers, while the drop at 58 K is the result of a gap with electron region on Fermi surface. The anomaly of Seebeck coefficient change in the other three materials could be explained similarly.

4.7.3 Hall Coefficient

Fig. 4.19 shows the comparison of Hall coefficients of the four selected CDWs. It can be seen that: (1) Group VB TMDCs have similar order of magnitude in Hall coefficient, much lower than that of $NbSe_3$. This agrees with the metallic nature of these three materials. (2) There is a sign change in all three TMDCs Hall coefficients (even though the sign change in VSe_2 is less convincing due to the small magnitude of Hall coefficient near room temperature), but is not observed in $NbSe_3$. The change in sign is consistent with the presence of multi-band conducting in the three TMDCs. (3) The change in VSe_2 is similar to the 120 K CDW in $TaSe_2$, and is less distinct the others.

4.7.4 Heat Capacity

Fig. 4.20 compares the heat capacity of the four CDW materials. For $NbSe_3$, only the specific heat data around $T_{CDW} = 58K$ was reported. Nonetheless, it is clear that the anomalies across transition temperature among the other three CDW materials are more abrupt than VSe_2, which indicates that fewer electrons are involved in the CDW transition in VSe_2 than the other three CDW materials.

Indeed, Fig. 4.21 gives a summary of the anomaly across CDW transitions in $NbSe_2$, TaS_2, $TaSe_2$, and VSe_2, reported by J.M.E. Harper et al. in 1977 [117]. It can be clearly seen that the changes in entropy during the transition, ΔS, in the other TMDCs are higher than in VSe_2(see section 4.5). Moreover, in the original paper of Fig. 4.21 [117], it was claimed that the measurements of 3 mg VSe_2 crystals found no thermal anomaly to a level of $\Delta c/c = 1\%$. Although an anomaly in the specific heat of VSe_2 was observed in this work, the fact that the CDW transition in VSe_2 is

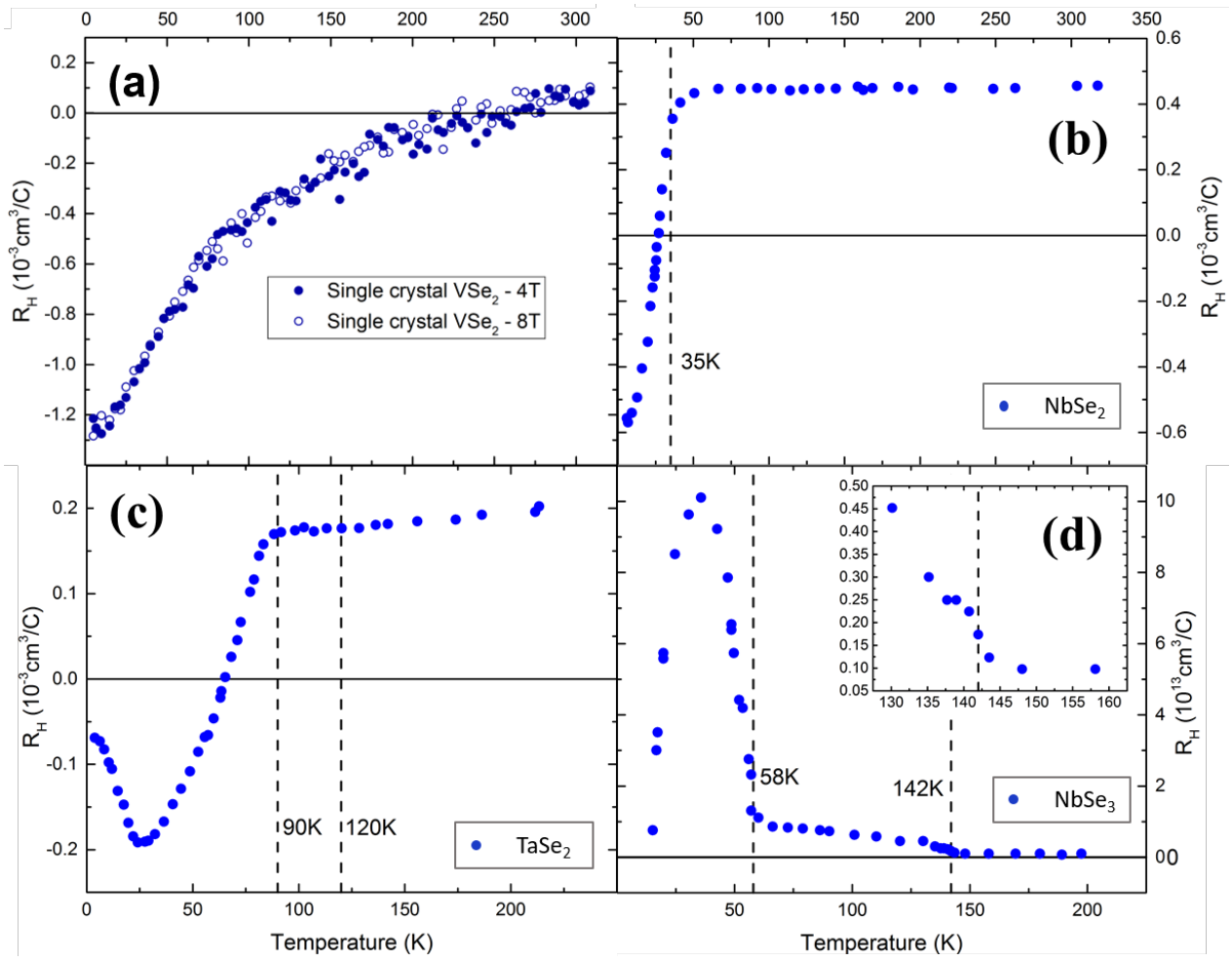

Figure 4.19: Hall coefficient of (a) single- and poly-crystalline 1T-VSe_2, (b) 2H-$NbSe_2$ [111], (c) 2H-$TaSe_2$ [111] and (d) $NbSe_3$ [116]. The dashed vertical lines indicate CDW temperatures.

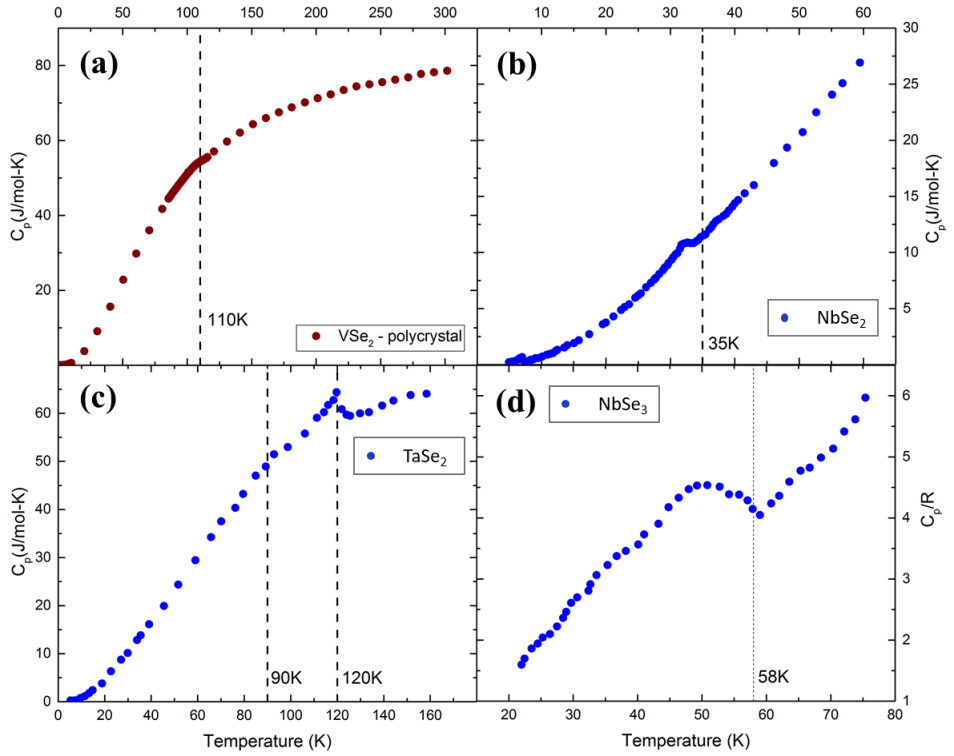

Figure 4.20: Heat capacity of (a) 1T-VSe_2, (b) 2H-$NbSe_2$ [117], (c) 2H-$TaSe_2$ [117] and (d) $NbSe_3$ [118].

Material	T_c (K)	γ mJ/mole K^2	β mJ/mole K^4	Θ_D (K)	T_0 (K)	Order	$\Delta C/C$ (%)	$\Delta\rho/\rho$ (%)	ΔH (J/mole)	ΔS (J/mole K)
2*H*-$NbSe_2$	7.2	16.0	0.55	222	33.5	Second	6.5	3	1.9	0.059
2*H*-TaS_2	0.8 (Ref. 1)	7.5	0.44	236	78.0	Second	5.6	0.3 [a]	4.0	0.052
2*H*-$TaSe_2$	0.15 (Ref. 1)	4.5	0.71	202	121	Second	22	1.5	55	0.460
					90	First	< 0.1	< 0.1 [c]	•••	•••
4*Hb*-TaS_2	< 1.1 (Ref. 1)	3.0	0.45	234	317	First	•••	••• [b]	440.0	1.40
					22	First	•••	••• [b]	1.3	0.059
4*Hb*-$TaSe_2$	< 1.1 (Ref. 1)	4.5	0.83	192	≈75	No anomaly observed				
1*T*-VSe_2	< 1.1 (Ref. 7)	•••	•••	•••	110	No anomalies observed				
					≈80					

Figure 4.21: Analysis of specific heat anomaly near CDW transition in different TMDC materials [117]. γ and β are the two coefficients of low tempereature c_p; Θ_D is the Debye temperature; T_0 is the onset of CDW transition; order stands for the thermodynamic order of the transition; $\Delta c/c$ and $\Delta\rho/\rho$ are the fractional heights of the specific heat anomaly and resistivity anomaly, respectively; ΔH is the integrated heat of the transition; ΔS is the entropy of the transition.

much weaker than other TMDCs is unambiguous.

4.7.5 Thermal Conductivity

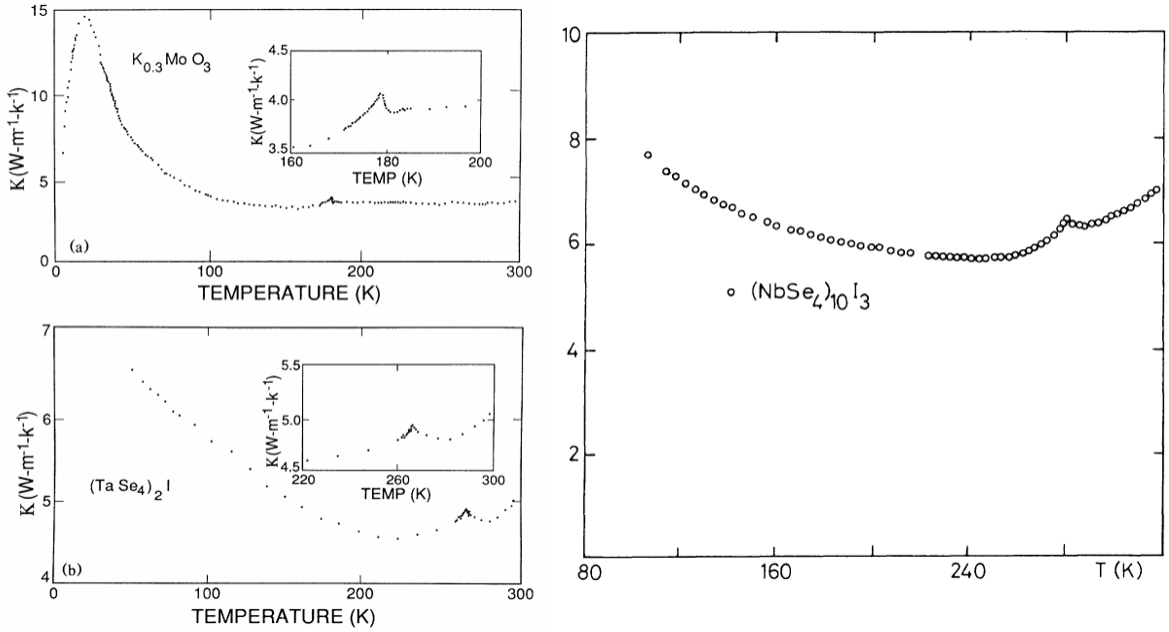

Figure 4.22: Thermal conductivity in typical CDW materials: $K_{0.3}MoO_3$ [119], $(TaSe_4)_2I$ [119] and $(NbSe_4)_{10}I_3$ [120].

Due to the lack of previous measurements of the thermal conductivity in TMDCs, results of this work will be compared with some typical CDW materials, including $K_{0.3}MoO_3$, $(TaSe_4)_2I$ and $(NbSe_4)_{10}I_3$. As shown in Fig. 4.22, similar anomalies in thermal conductivity were found in those materials near the CDW transition temperatures. However, in VSe_2, the anomaly is less prominent than the sharp peaks in the thermal conductivity of conventional CDW materials. This weak anomaly is consistent with the smaller specific heat kink measurement at the transition, which is discussed in section 4.7.4. Basically, the enhanced thermal conductivity could be attributed to the extra heat carried by soft phonons, due to Kohn anomaly effect [121].

4.8 Anomalies at Very Low Temperatures

In this section, investigations on the electrical resistivity and specific heat of VSe_2 at very low temperatures will be presented. Despite not directly related to the CDW transition, the properties

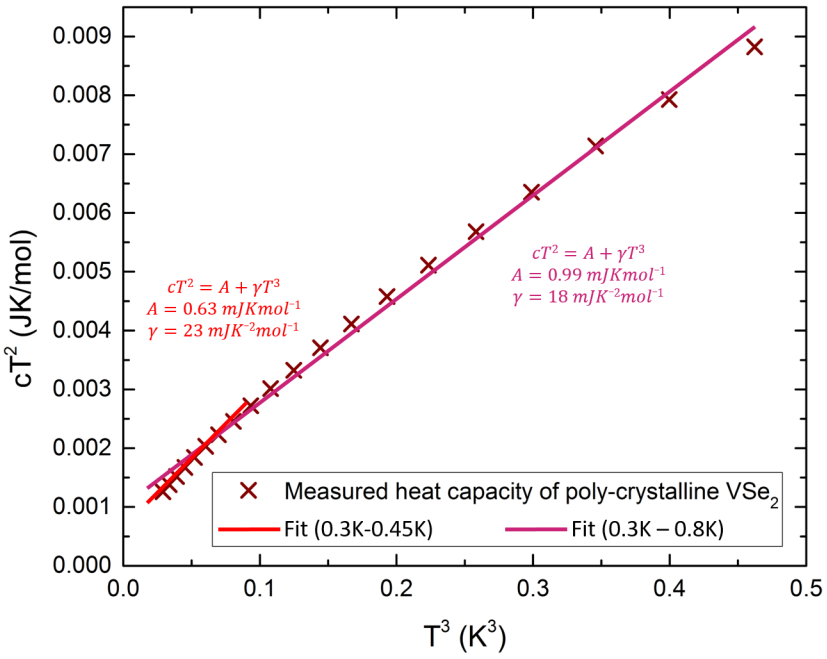

Figure 4.23: Plot of cT^2 vs. T^3 at very low temperatures, showing a sub-linear relationship.

at a few Kelvins can help us understand the ground state of VSe_2. Surprisingly, VSe_2 exhibits some interesting properties at very lower temperatures, which haven't been reported before: the heat capacity of both sinlge- and poly-crystalline VSe_2 deviates from the expected $c = \gamma T + \beta T^3$ relation. Besides, the electrical resistivity measurement shows an weak upturn below 10 K.

The results of low temperature heat capacity measurements are shown in Fig. 4.14 as a diagram of c/T vs. T^2, which show distinct derivation from the the common $c = \gamma T + \beta T^3$ behavior. A sharp upturn is found in the the c/T of poly-crystalline VSe_2 below $\sim 1.5K$. Similarly, an upturn is also present in the single-crystallien VSe_2 below $\sim 5K$, even though the sample was only measured down to 2 K so the majority of the anomaly is actually positioned below the temperature region measured.

The anomalous heat capacity of VSe_2 is most likely to be due to Schottky heat capacity, which is the most widly found origin of heat capacity anomaly. The schottky heat capacity anomaly occurs when there are two or multiple energy levels separated by energy on the same order of $k_B T$. The Schottky anomaly may arise from different origins, such as the interactions of crystal field of paramagnetic ions on the electron magnietic dipoles, and the coupling between nucleus spins and electron dipoles [122]. The Schottky anomaly is featured by a sharp peak in heat capacity, which is

sometimes at very low temperatures (especially for those caused by nucleus spin) that only the high temperature tail ($\propto T^2$) could be experimental observed. Details of the the Schottky heat capacity are given in Appendix D.

Therefore, taking the Schottky heat capacity into consideration, the low temperature molar heat capacity could be written as $c = AT^{-2} + \gamma T + \beta T^3$, where A is the parameter of T^{-2} Schottky term. In the heat capacity of poly-crystalline VSe_2, data at higher temperature (3.5 K - 6 K) is fitted assuming the Schottky term could be neglected in this tempearture range, and the resulting coefficients are $\gamma = 10 mJK^{-2}mol^{-1}$ and $\beta = 0.65$ (shown in Fig.4.14). The heat capacity at very low temperatures is ploted as cT^2 vs. T^3, which is shown in Fig. 4.23. Assuming the βT^3 term is negligible at such a low temperatures, the cT^2 is supposed to be linear depend of T^3, with γ and A the slope and y-intercept of the plot, respectively. The measured values, however, look sub-linear, with $\gamma = 23\ mJK^{-2}mol^{-1}$ and $A = 0.63\ mJK/mol$ at 0.3 K - 0.8 K, and are $\gamma = 18\ mJK^{-2}mol^{-1}$ and $A = 0.99\ mJK/mol$ at 0.3 K - 0.8 K. This derivation from linear behavior could be of different sources. It is possible that there is additional unknown term in heat capacity that is involved, or the heat capacity anomaly found in the VSe_2 is not exactly Schottky-like, so it doesn't obey the T^{-2} temperature dependent.

The contribution from V_2O_3 impurities in the poly-crystalline VSe_2 sample should also be taken into consideration. From the results of XRD measurements done at Wuhan University of Technology (Fig.3.5), there is a small amount of V_2O_3 impurities in the poly-crystalline VSe_2 sample. V_2O_3 is an insulator at low temperatures (it has a metal-insulator transition at $\sim$ 150 K), and there is a Schottky anomaly in its heat capacity peaked at $\sim$ 10 mK [123–125], which is due to nuclear spin of ^{51}V atom. However, the amount of V_2O_3 impurity in the poly-crystalline VSe_2 sample is very small: the highest V_2O_3 peak is about 1% the intensity of the highest VSe_2, which is a roughly reflection of the low concentration of V_2O_3. The parameter of the T^{-2} term in the heat capacity of V_2O_3 is reported as $3.7 - 9.0 mJK/mol$ from different groups [123–126]. In that case, assuming the heat capacity anomaly found at very low temperatures is contributed all to V_2O_3 instead of VSe_2, at least 7 molar percent V_2O_3 is needed to produce such an intense anomaly, which is totally in contradict with the weak V_2O_3 peaks found in the XRD patterns. Besides, the VSe_2 single crystal also shows an similar trend of deviation from the $c = \gamma T + \beta T^3$ behavior, but there is no evidence that V_2O_3 impurity is involved in the single crystal sample. However, it is worth noting that at least a minority portion of the heat capacity anomaly found in poly-crystalline VSe_2 sample

is indeed from the nuclear spin of V atom in V_2O_3 impurities.

Besides the Schottky heat capacity, there are other sources that could give rise to an anomaly in heat capacity. Firstly, non Fermi liquid behavior in heavy fermion systems can also have an upturn in low temperature heat capacity [127]. For instance, in both $CeNi_4Cu$ and $YbNi_4Cu$, an upturn in Cp was found, and external magntiec field can suppress the anomaly [128]. But most heavy fermion systems have 4f or 5f atoms (such as Ce or U), while V has an electron configuration of $3d^3 4s^2$. Hence the anomaly in V is unlikely due to the non-Fermi liquid behavior. On the other hand, many quantum spin liquid materials feature a 2-D triangular lattice. In 1950, G.H. Wannier calculated the spin configuration in a 2-D infinite trigangular set of Ising spins, and found out the system is disordered at all temperatures and possesses no Curie point [129]. In 1973, P.W. Anderson proposed a so-called resonating valence bond (RVB) model to describe the ground state, which is the superposition of all possible pairing between the spins. There are a few candidates of this type of material. One example is $EtMe_3Sb[Pd(dmit)_2]_2$, the specific heat of which at low temperatures shows a sharp upturn [130]. Another example is $NiGa_2S_4$, in which a hump in specific heat was observed [131]. It is worth mentioning that $NiGa_2S_2$ adopts the same $P\bar{3}m1$ symmetry as VSe_2. In the former crystal, Ni atoms form a triangular 2-D lattice while in VSe_2, a similar layer consists of V atoms, as shown in Fig. 4.24.

Nonetheless, to identify the anomaly in the specific heat of VSe_2, further experiments are needed. For example, magnetic susceptibility at lower temperatures, and magnetic field dependence of specific heat can help us understand the nature of the upturn. Specific heat measurement to even lower temperature is also helpful, as the entropy calculation is feasible if the whole peak could be measured.

On the other hand, there is also a weak but distinct upturn in the electrical resistivity of VSe_2 single crystal. As it is shown in (Fig. 4.25, the resistivity increases about 0.2% when the temperature decreases from 10 K to 2 K. The origin of this upturn is still to be determined.

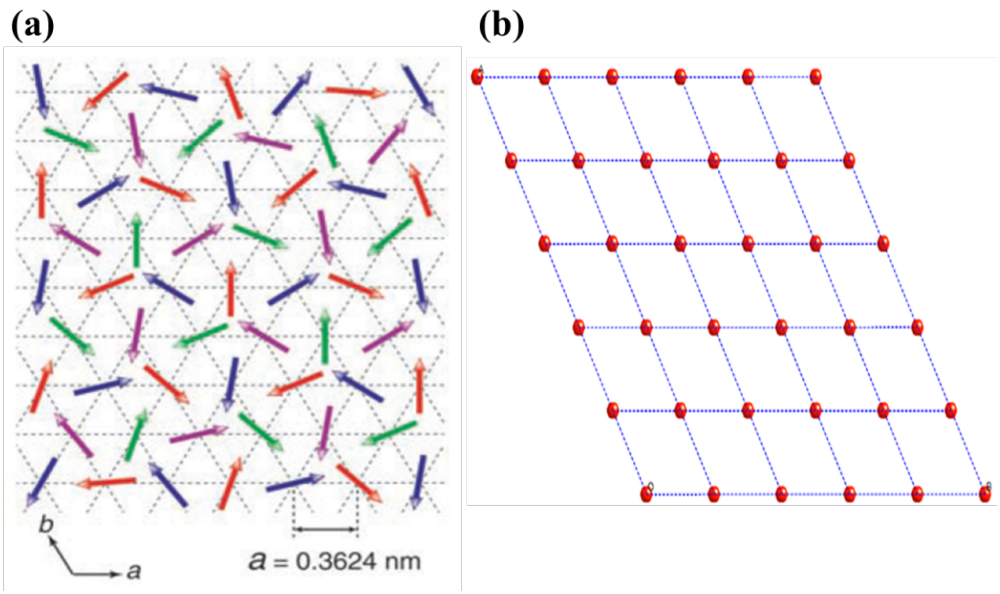

Figure 4.24: 2-D triangular lattice plane formed by (a) Ni atoms in $NiGa_2S_4$ (b) V atoms in VSe_2 [131].

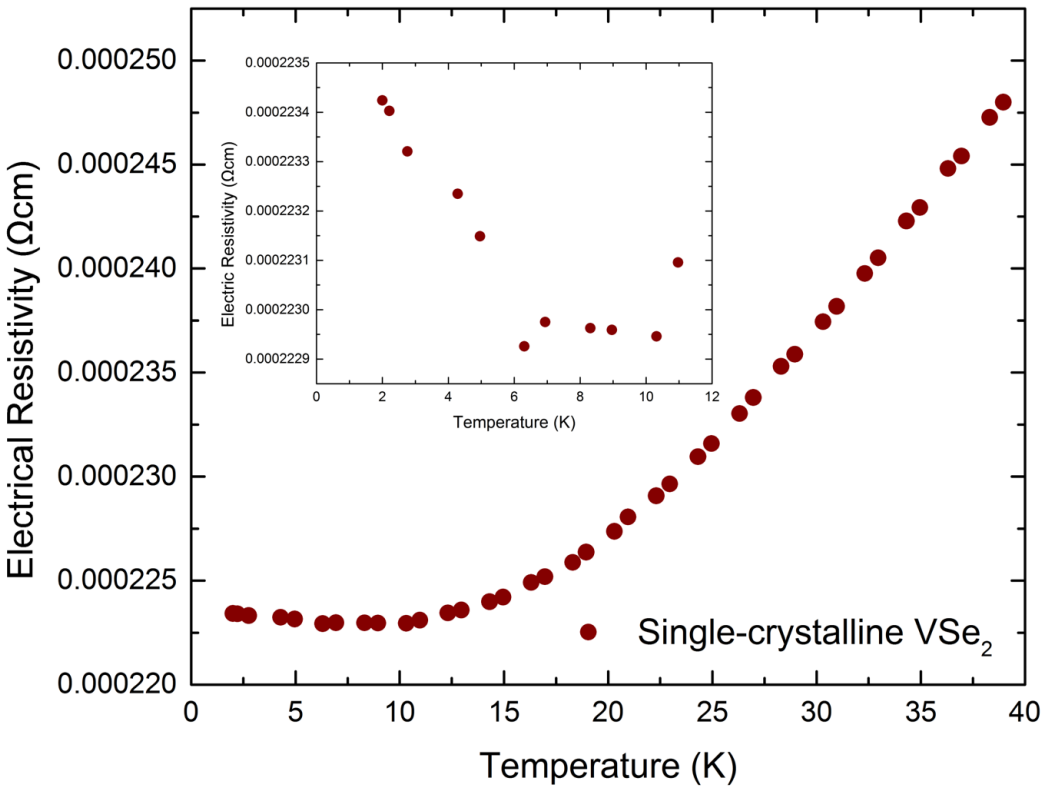

Figure 4.25: Low temperature electrical resistivity of VSe_2 single crystal. The inset shows the upturn below 10 K.

Chapter 5

Conclusions and Future Works

5.1 Conclusions

The first conclusion we can make is that 1T-VSe_2 has relatively strong electron-phonon coupling, which could be confirmed from the experimental results: (1) In electrical resistivity measurement, the slope of ρ/T is large, indicating a strong e-ph interaction; (2) also, in the Seebeck coefficient of single-crystalline 1T-VSe_2, the weak hump centered $\sim$20 K is possibly due to phonon drag effect, which also implies the coupling between electrons and phonons is indispensable. Thus, VSe_2 is a quasi-2-D material with strong electron-phonon coupling, which favors the formation of CDW state in the system. In addition, the correlation map of Fermi surface nesting and wave vector derived from DFT calculations doesn't show a maximum at the observed $\mathbf{q}_{CDW}$, implying that the CDW formation in 1T-VSe_2 may not be solely contributed to Fermi surface nesting.

Besides, it is suggested that the CDW formation only gaps a small portion of Fermi surface, and the CDW is very weak. It is deduced from the facts that: (1) Electrical resistivity, Seebeck coefficient, thermal conductivity and heat capacity measurements all show anomalies at around T_{CDW}, similar to other CDW materials, but with a much weaker magnitude; (2) calculation of the entropy change derived from specific heat measurement indicates that only a small amount of Fermi surface is involved in the CDW transition.

The comparison of CDW in VSe_2 and some other CDWs indicates that the mechanisms of the CDW in these materials might not be the same. Even in one material, there could be multiple driving forces that lead to the CDW formation.

Other than the CDW phase transition, there are some other notable features at very lower temperatures. The heat capacity of VSe_2 deviates from the Debye-Sommerfeld equation at temperatures < 10 K for single-crystalline VSe_2 and < 1.5 K for poly-crystalline VSe_2, and the deviation is very significant in poly-crystalline VSe_2 as it was measured down to lower temperatures. In the electrical resistivity measurement of VSe_2 single crystal (while polycrystalline VSe_2 was not measured down to that low temperatures), a weak upturn is also found at temperatures below 10 K. The nature of the anomaly in heat capacity is considered to be related with the Schottky heat capacity, which is most likely to be caused by nuclear spin in V atoms. Real origin of the low temperature anomalies still needs to be clarified in the future work.

5.2 Future Works

More works are needed to further investigate the CDW and low temperature anomalies in VSe_2. Here are some proposed future works:

(1) Growth of a larger single crystal with less defects.

(2) Measuring electrical resistivity (at lower temperature) and magnetic susceptibility of polycrystalline VSe_2. Applying external magenetic field when measuring the resistivity and heat capacity, and see if there is any change in the low temperature anomalies.

(3) Most of experiments in this work are about the transport properties. Other techniques that can directly probe the lattice symmetry are suggested, e.g., electron diffraction, TEM, with which we can directly observe the super-lattice formed during CDW transition, if there is.

(4) Also, we can probe the band structure and DOS, for both electrons and phonons. Techniques to be adopted include: neutron scattering, STM, ARPES, etc. With these measurements, we can understand the change in band structure of the CDW transition, so as to determine the shape and direction of nested Fermi surface, also to determine whether it is commensurate or incommensurate.

Although the results in this work suggests that the CDW transition in VSe_2 is weak, the conclusion is merely qualitative, and more experimental and theoretical works are needed to further clarify the nature of CDW in VSe_2.

Appendices

Appendix A Characterization of CDW

There are various techniques to experimentally probe the CDW state in the material, including: (i) X-ray, electron scattering, neutron scattering to determine the lattice distortion; (ii) angle-resolved photoemission, scanning tunneling and optical spectroscopy to probe the electronic band structure; (iii) specific heat and transport measurements to characterize the change in electronic and phononic properties during CDW transition. In this section, we give some examples of CDW characterization with different techniques.

A.1 Scanning Tunneling Microscopy (STM)

As most CDW transitions involve lattice distortion, the most intuitive method we can adopt is observe the image of the structures directly, as shown in Fig. 1. Moreover, STM can also detect the gap opening in CDW state. An example is shown in Fig. 2.

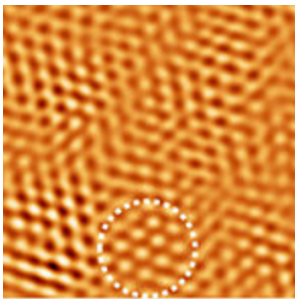

Figure 1: STM topographic image of 2H-$NbSe_2$. The dash-dotted circle shows the patch with well-defined CDW structure in the sample [132].

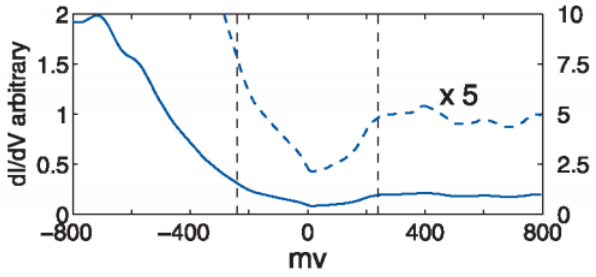

Figure 2: STM spectrum of CDW material $TbTe_3$. A depressed density of states is found at zero bias [133].

A.2 X-Ray Diffraction and Electron Diffraction

Instead of imaging, XRD and electron diffraction can probe the formation of super lattice via diffraction. Fig. 3 shows two examples of detecting superlattice in CDW state. In electron diffraction, CDW peaks are weaker and away from Bragg peaks.

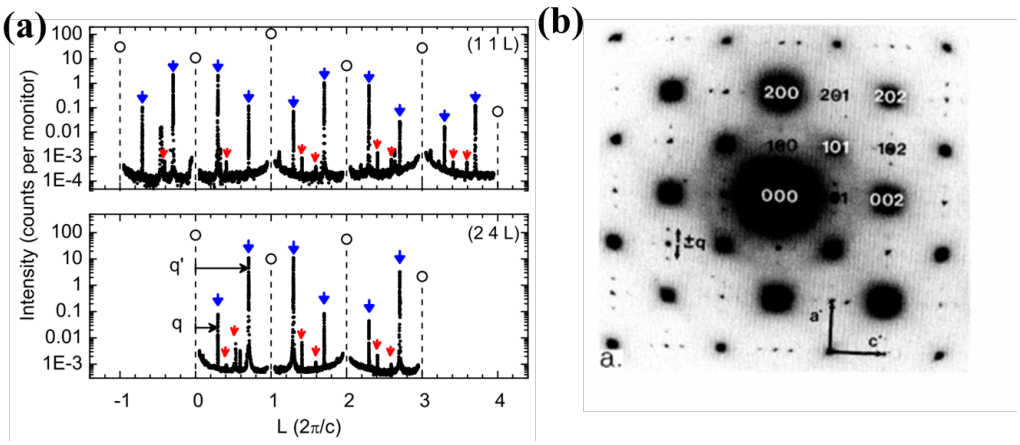

Figure 3: (a) Representative X-ray Diffraction Patterns for $TbTe_3$ along (11L) and (24L) at room temperature. Open circles are Bragg peaks and are scaled down by a factor of 1000; CDW modulation is marked by blue and red arrows [29]. (b) TEM image of $SmTe_3$, the weak satellite peaks correspond to CDW phase [134].

A.3 Angle Resolved Photoemission Spectroscopy (ARPES)

ARPES can be used to directly probe the electron band structure and thus the Fermi surface nesting vector can be directly measured.

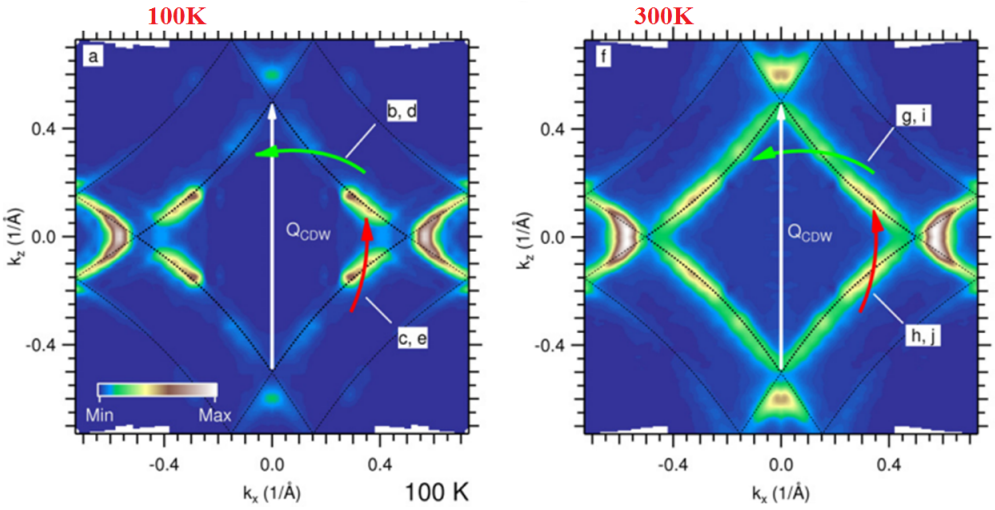

Figure 4: Fermi surface measured of $TbTe_3$ with ARPES at 100K and 300 K. The segments of Fermi surface that are gapped by CDW are shown [135].

A.4 Transport Measurements

Most transport properties can be affected by CDW, including resistivity, Seebeck coefficient, thermal conductivity, etc.. In most CDW materials, anomalies can be observed when entering CDW state, e.g., an increase in resistivity with decreasing temperature. Despite the fact that the cause of these anomaly could be different, in some systems, especially low dimensional materials with strong e-ph coupling, the possibility of CDW cannot be excluded without further investigation.

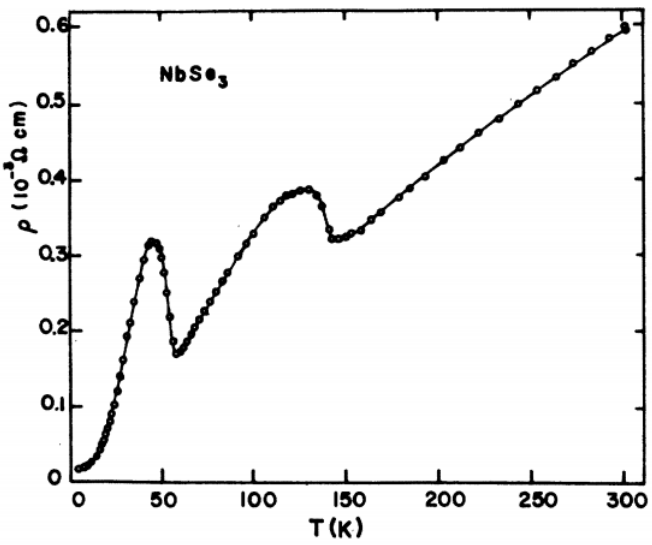

Figure 5: Temperature dependence of resistivity of $NbSe_3$. Two CDW transitions are found at 59K and 145K [110].

Appendix B The Nature of Seebeck coefficient

The Seebeck coefficient, also called thermopower, is defined as $S = -\frac{\Delta V}{\Delta T}$. When a temperature difference ΔT is applied to the two ends of a material, an electrical voltage difference ΔV will be observed, and the ratio of voltage and temperature differences is Seebeck coefficient of this material. A negative sign is added here so that the sign of Seebeck coefficient can also represents the sign of charge carrier, i.e., the type of the conductor. The Seebeck coefficient is a 3×3 tensor, as the action, the temperature difference, and the reaction, the voltage difference, could be in different directions in a material. However, in most cases, the main concern is the diagonal value of the Seebeck tensor, which means the directions of ΔT and ΔV are the same. The typical Seebeck coefficient of metal ranges from 1 to 10 $\mu V/K$, whereas for semiconductors, it is around hundreds of $\mu V/K$. One of the most popular applications of Seebeck effect is thermal couple.

Other than from the definition equation, there is another way to understand Seebeck coefficient: the entropy carried per charge carrier. In 1990, P. M. Chaikin [136] pointed out that the

Seebeck coefficient can be expressed as

$$S = \frac{\text{"}heat\text{" } per\ carrier}{charge\ per\ carrier} or S = \frac{entropy\ per\ carrier}{q}.$$

The idea is simple and intuitive, but reveals very important information of the charge carrier: the characteristic energy associated with it. For example, in metals, the heat per carrier is $\approx c_{el}T$, where c_{el} is the electronic specific heat, which is proportional to the temperature and the density of states at the Fermi level:

$$c_{el} = \frac{\phi^2}{3}\frac{{k_B}^2 T N(\varepsilon_F)}{n} \sim \frac{{k_B}^2 T}{\varepsilon_F}.$$

Thus,

$$S \sim \frac{c_{el}}{q} \sim \frac{k_B}{e}\frac{k_B T}{\varepsilon_F},$$

while in semiconductors with only one type of carrier. The heat carried by a particle is the difference in the energy from the chemical potential, as

$$\text{"}heat\text{"} =< E - \mu > \sim E_g - \mu \sim E_g/2$$

$$S \sim \frac{E_g/2}{eT} \sim \frac{k_B}{e}\frac{E_g}{2k_B T}.$$

For semiconductors, the Seebeck coefficient is inversely proportional to temperature, and directly proportional to the energy gap. With the presence of disorder, however the Seebeck coefficient could behave quite differently. Disorder can lead to localization effect which can be described by variable range hopping model [137]. P.M. Chaikin pointed out that in such case, there is a finite density of states at the Fermi level, but the energy spread of the carriers is the energy difference between adjacent sites δE, not $k_B T$:

$$\text{"}heat\text{"} \sim c_{el}T \sim {k_B}^2 T^2 N(\varepsilon_F) \rightarrow N(\varepsilon_F){k_B}^2 \delta E^2$$

$$S \sim \frac{N(\varepsilon_F){k_B}^2 \Delta E^2}{eT} \propto T^{\frac{d-1}{d+1}},$$

where d is the dimension of the material. Therefore, from Seebeck coefficient one can distinguish between a mobility gap and an energy gap [138].

Fig. 6 gives a summary of Seebeck coefficient behaviors in different systems. It is worth

General	$\frac{c_{el}}{q}$ or $\frac{\text{"heat"}}{qT}$
Classical	$\frac{k_B}{q}$
Metals	$\frac{k_B}{q}\frac{k_B T}{\epsilon_F}$
Semiconductors	$\frac{k_B}{q}\frac{E_g}{2k_B T}$
Variable Range Hoping	$\frac{k_B}{q}\left(\frac{T}{T_0}\right)^{\frac{d-1}{d+1}}$
Hubbard Large U Hopping	$\frac{k_B}{q}(\ln 2 + \ln\frac{1-\rho}{\rho})$
Polarons	$\frac{k_B}{q}\ln\rho$
Phonon Drag	$\frac{k_B}{q}\frac{1}{\rho}\left(\frac{T}{\theta_D}\right)^3$ Low T $\frac{k_B}{q}\frac{1}{\rho}\left(\frac{\theta_D}{T}\right)$ High T
Superconductor	0
Sliding Density Wave	0
Quantum Hall	0 filled level $\frac{k_B}{e}\frac{\ln 2}{(N+1/2)}$ $\frac{1}{2}$ filled

Figure 6: Summary of Seebeck coefficient behaviors [136].

noting that the sliding density wave has a zero Seebeck coefficient. Therefore, in charge density wave materials, the sliding conduction mode carries no entropy.

In a crystalline material with band conduction, the Seebeck coefficient is closely related to the electronic band structure of the material. If the relaxation process is much faster than the transport process, and if local deviation from equilibrium is very small, the Boltzmann equation can be linearized [139]. The general expression of Seebeck coefficient is given by

$$S = \frac{k_B}{e}\frac{\int \sigma(E)\frac{E-E_F}{k_B T}(-\frac{\partial f_{eq}}{\partial E})dE}{\int \sigma(E)(-\frac{\partial f_{eq}}{\partial E})dE},$$

where $\sigma(E)$ is energy-dependent electrical conductivity, f_{eq} is Fermi-Dirac distribution function. The $\sigma(E)$ is given by

$$\sigma(E) = q^2\tau(E)\int\int {v_x}^2(E,k_y,k_z)\,dk_y dk_z \cong q^2\tau(E)\,\bar{v}_x^2(E)\,D(E),$$

where q is the unit charge, $v(k)$ is the carrier shift velocity, and $D(E)$ is the density of states. $\tau(E)$ is the energy dependence of electronic relaxation time, which strongly depends on the scattering

mechanism. The two equations above clearly elaborate the two origins of the entropy flow: (i) different DOS between the initial and final state, and (ii) scattering through different intermediate states (i.e., the entropy created).

Furthermore, in a system where charge carriers are independent with each other, i.e. weak electron-electron interaction, the linear response conductance σ and Seebeck coefficient S were given by Mott and his coworkers [140, 141] as

$$\sigma = \int \sigma(E) \left(-\frac{df(E)}{dE} \right) dE$$

$$S = \frac{\pi^2}{3} \left(\frac{{k_B}^2 T}{e} \right) \left(\frac{d \ln \sigma(E)}{dE} \right)_{E=E_F},$$

which are also known as Mott relations. The equations also indicate that Seebeck coefficient is sensitive to the asymmetry of band structure in the vicinity of Fermi level. It is worth noting that, similar to the Wiedemann-Franz relation, Mott relations are only valid in the systems of weak interactions. Thus if the Wiedemann-Franz relation fails in a material, the Mott relations are usually also no longer valid [142].

With Mott relations, an estimate can be made for the Seebeck coefficient in different materials. The two most intuitive situations are (1) metals, where the conduction occurs near the Fermi level, and (2) semiconductors, where thermal excitations facilitate electrical transport. To understand the behaviors of the Seebeck coefficient in these two systems, we can first rewrite the expression of Seebeck coefficient as

$$S = -\frac{k_B}{e} \left(\eta - \frac{\left(r + \frac{5}{2}\right) F_{r+\frac{3}{2}}(\eta)}{\left(r + \frac{3}{2}\right) F_{r+\frac{1}{2}}(\eta)} \right),$$

where

$$F_n(\eta) = \int \frac{\xi^n}{1 + e^{\xi - \eta}} \mathrm{d}\xi$$

is the Fermi-Dirac integral, $\eta = \mu / k_B T$, and r describes scattering mechanism as $\tau = \tau^0 E^r$.

In metals, the energy of charge carriers is in the range of $\mu \pm k_B T$. The Fermi-Dirac integral can be expressed in the form of series:

$$F_n(\eta) = \frac{\eta^{n+1}}{n+1} + \frac{\pi^2}{6} n \eta^{n-1} + ...,$$

where the higher order terms are omitted. Hence the Seebeck coefficient can be expressed by

$$S_{metal} = -\frac{\pi^2 k_B}{3e}\left(\frac{k_B T}{\mu}\right)\left(\frac{3}{2}+r\right).$$

Some important features can be obtained from the above expression. Firstly, the $(3/2+r)$ term, i.e. the energy dependence of scattering rate, determines the sign of Seebeck coefficient in metals, which explains why some metals exhibit positive Seebeck coefficient. Secondly, in metals usually μ is much greater than $k_B T$, thus the Seebeck coefficients of metals are relatively small. Last but not least, the Seebeck coefficient in a metal is linearly proportional to temperature.

In semiconductors, however, the Seebeck coefficient behaves much differently. Now μ is inside the band gap between conduction and valence bands. In this case, if we assume $E-\mu \gg 1$, the Fermi-Dirac integral becomes

$$F_n(\eta) = \int \frac{\xi^n}{1+e^{\xi-\eta}}\mathrm{d}\xi \approx \int \frac{\xi^n}{e^{\xi-\eta}}\mathrm{d}\xi = e^{\eta}\Gamma(n+1),$$

where the gamma function is

$$\Gamma(n+1) = \int_0^{\infty} e^{-x}x^n \mathrm{d}x = n\Gamma(n).$$

Now the Seebeck coefficient equals

$$S = -\frac{k_B}{q}\left(\eta - \left(r+\frac{5}{2}\right)\right) = -\frac{1}{qT}\left(\mu - k_B T\left(r+\frac{5}{2}\right)\right).$$

Here q is the unit charge of the material, and it can be either positive or negative. And μ is negative for electrons and positive for holes. For electrons and holes, the Seebeck coefficients are

$$\begin{array}{l} S_e = -\frac{1}{eT}\left(E_C - \mu + k_B T\left(r+\frac{5}{2}\right)\right) \\ S_h = \frac{1}{eT}\left(\mu - E_V + k_B T\left(r+\frac{5}{2}\right)\right) \end{array},$$

where E_C and E_V are the band edge of conduction band and valence band, respectively. If both electrons and holes are involved in electrical transport, the total Seebeck coefficient is given by

$$S_{tot} = \frac{\sigma_e S_e + \sigma_h S_h}{\sigma_e + \sigma_h}.$$

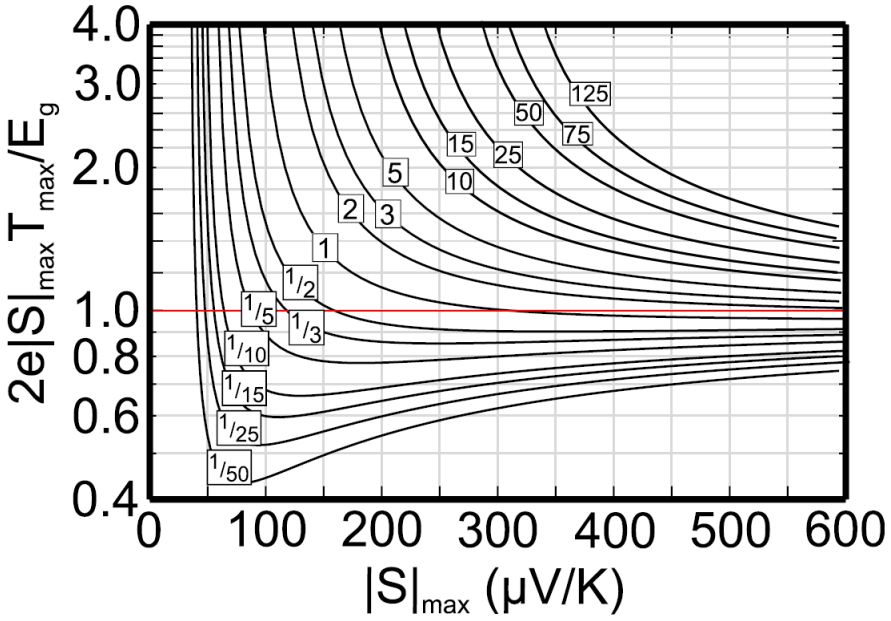

Figure 7: The relationship between the accuracy of Goldsmid-Sharp estimation and the maximum value of Seebeck coefficient [143].

Therefore, unlike in metals, the behavior of Seebeck coefficient in semiconductors is more complicated. The temperature dependence is not linear, and both electron and hole can contribute to the total Seebeck coefficient.

In semiconductors, the Seebeck coefficient is related to the carrier concentration n and the electron effective mass m^* by the Pisarenko relation [144]

$$S = \frac{8\pi^2 k_B^2 T}{3qh^2} m^* \left(\frac{\pi}{3n}\right)^{2/3},$$

where k_B is the Boltzmann constant, T is absolute temperature, q is carrier charge, h is the Plank constant, m^* is the effective at Fermi level, and n is the carrier concentration. The equation indicates that in single band semiconductors, S is inversely proportional to $n^{2/3}$.

Another important feature in semiconductors is the bipolar effect. In doped semiconductors, the total Seebeck coefficient is largely determined by the energy level of the dopant. But as the temperature goes higher, the intrinsic band gap of the host semiconductor matrix can be overcomed by thermal excitation, thus the other type of charge carrier starts to play a role. As electron and

hole have opposite signs of the Seebeck coefficient, the total Seebeck coefficient will degrade, and experimentally, we will observe a maximum in S vs. T plot. Evidently, the position and magnitude of the peak depends on the band gap of the material. The relationship is given by the Goldsmid-Sharp formula [145]

$$E_g = 2e|\mathrm{S}|_{\max} T_{\max}.$$

One can thus estimate the band gap width from the Seebeck coefficient peak. Note that this equation is only a rough estimation, and in some materials the calculated result deviates from the experiments, as shown in Fig. 7 [143].

Another notable effect in the Seebeck coefficient is phonon drag. Phonon drag is an effect where an increase in Seebeck coefficient is observed as temperature goes down. As electron/holes move along the lattice, the effective mass of charge carriers will increase due to electron-phonon interaction. Thus phonon drag often occurs in a material where e-ph coupling is predominant. The magnitude of Seebeck increase is usually weak, and it happens at temperatures close to $\sim \frac{1}{5}\theta_D$ [95].

Appendix C The Schottky Anomaly

In some materials, the heat capacity shows a hump at low temperatures. Such an anomalous behavior is presumably due to the Schottky anomaly, named after Walter H. Schottky. The Schottky anomaly usually occurs when an ion in the crystal consists of two or more energy levels, and the energy splitting is very small [122]. At zero temperature, lowest energy levels are occupied, and there is no further excitation. As temperature gets higher, the probability of excitation to higher energy levels increases, and so does the specific heat. But at high temperatures, all energy levels are evenly populated and there is no further excitation. Hence the maximum in C_p occurs at the temperature T' that satisfies $k_B T' \sim \Delta$, where k_B is Boltzmann constant, Δ is the energy gap between two levels. For a two level system, the Schottky anomaly contribution to the specific heat has the form [146]:

$$c_{Schottky} = R(\frac{\Delta}{T})^2 \frac{e^{\Delta/T}}{[1+e^{\Delta/T}]^2}$$

.

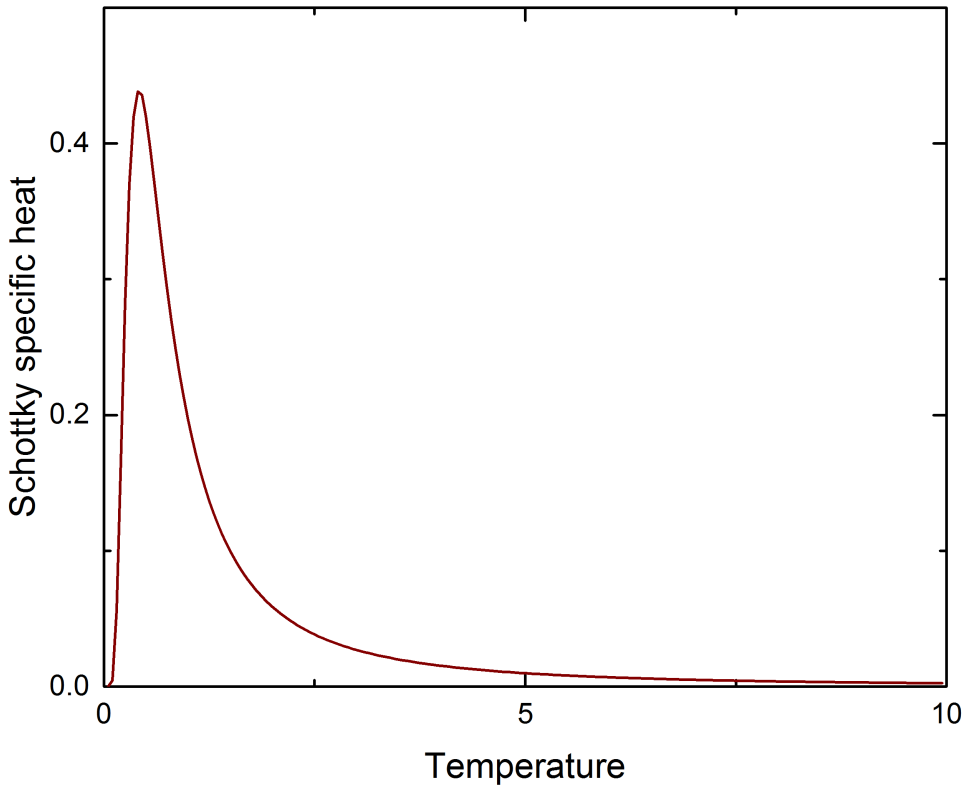

Figure 8: Theoretical calculated temperature dependence of Schottky specific heat. Specific heat and temperature here are in arbitary unit.

From the equation, it can be seen that at low temperatures where $\Delta \gg k_B T$, the Schottky term reduces to $c_{Schottky} = R(\frac{\Delta}{T})^2 e^{-\Delta/T}$. And at high temperatures where $\Delta \ll k_B T$, the term takes the form $c_{Schottky} = R(\frac{\Delta}{T})^2$. Therefore, at very low temperatures, Schottky specific heat increases exponentially with temperature, and at high temperatures, it decreases with a T^{-2} dependence. The calculated result is shown in Fig. 8.

Although the concept of Schottky anomaly of multiple energy levels with small gaps is not complicated, in real materials several mechanisms can cause the splitting. The most common scenario is paramagnetic ions interacting with the surrounding crystal electrical field. At low temperatures, the interaction between the electron magnetic dipole of the paramagnetic ion and its crystal field

will cause a preferential alignment which lowers the energy. The magnitude of the energy splitting gap is very small and the excitations can occur at very low temperatures.

The Schottky anomaly has been found in various systems. One example is antiferromagnetic (AFM) phase transition, such as $Ca_3Mn_2Ge_3O_{12}$ at $\sim 14K$ [147], and $EuNi_5P_3$ at $\sim 8K$ [148]. In such systems, specific heat forms a λ-anomaly at Neel point, and the peak can be smeared by applying external magnetic field.

Bibliography

[1] G. Grüner. The dynamics of charge density waves. *Reviews of Modern Physics*, 60:1129–1181, 1988.

[2] W.L. McMillan. Theory of discommensurations and the commensurate-incommensurate charge-density-wave phase transition. *Physical Review B*, 14:1496, 1976.

[3] H.Fröhlich. "on the theory of superconductivity: The one-dimensional case. *Proceedings of the Royal Society A*, 223:296–305, 1954.

[4] J.A. Wilson, F.J. DiSalvo, and S. Mahajan. Charge-density waves and superlattices in the metallic layered transition metal dichalcogenides. *Advances in Physics*, 24:117–201, 1975.

[5] A.W. Overhauser. Spin density waves in an electron gas. *Physical Review*, 128:1437–1452, 1962.

[6] A.W. Overhauser. Giant spin density waves. *Physical Review Letters*, 4:462–465, 1960.

[7] J. Kondo. Resistance minimum in dilute magnetic alloys. *Progress of Theoretical Physics*, 32:37–49, 1964.

[8] H.K. Onnes. The resistance of pure mercury at helium temperatures. *Communications From The Laboratory Of Physics At The University Of Leiden*, 12:120, 1911.

[9] W. Meissner and R. Ochsenfeld. Ein neuer effekt bei eintritt der supraleitfhigkeit. *Naturwissenschaften*, 21:787–788, 1933.

[10] F. London and H. London. The electromagnetic equations of the supraconductor. *Proceedings of the Royal Society of London A*, 149:71–88, 1935.

[11] J. Bardeen, L.N. Cooper, and J.R. Schrieffer. Theory of superconductivity. *Physical Review*, 108:1175–1205, 1957.

[12] B.T. Matthias, T.H. Geballe, and V.B. Compton. Superconductivity. *Review of Modern Physics*, 35:1–22, 1963.

[13] L. Landau. Uber die bewegung der elektronen im kristalgitter. *Physikalische Zeitschrift der Sowjetunion*, 3:644–645, 1933.

[14] S.I. Pekar. Research in electron theory of crystals (Russian edition 1951, German edition 1954). *US Atomic Energy Commission*, AEC-tr-555, 1963.

[15] K.B. Tolpygo. Physical properties of a rock salt lattice made up of deformable ions. *Zhurnal Eksperimentalnoi i Teoreticheskoi Fiziki*, 20:497–509, 1950.

[16] K. Huang. Lattice vibrations and optical waves in ionic crystals. *Nature*, 167:779–780, 1951.

[17] K. Huang. On the interaction between the radiation field and ionic crystals. *Proceedings of the Royal Society of London A*, 208:352–365, 1951.

[18] G. Grüner. *Density waves in solids*. Addison-Wesley, 1994.

[19] R.E. Peierls. *Quantum theory of solids*. Oxford University Press, 1955.

[20] C.G. Kuper. On the thermal properties of frohlich's one-dimensional superconductor. *Proceedings of the Royal Society of London. Series A, Mathematical and Physical Sciences*, 227:214, 1955.

[21] S.-K. Chan and V. Heine. Spin density wave and soft phonon mode from nesting Fermi surfaces. *Journal of Physics F: Metal Physics*, 3:795, 1973.

[22] K. Rossnagel. On the origin of charge-density wave in select layered transition-metal dichalcogenides. *Journal of Physics: Condensed Matter*, 23:213001, 2011.

[23] W. Kohn. Image of the fermi surface in the vibration spectrum of a metal. *Physical Review Letters*, 2:393, 1959.

[24] S. Brown and G. Gruner. Charge and spin density waves. *Sci. Am.*, April:50–56, 1994.

[25] S.N. Artemenko and A.F. Volkov. On the theoroy of frohlich conductivity of a conductor with a commensurable charge density wave. *Z. Eksp. Teor. Fiz.*, 81:1872–1981, 1981.

[26] R.M. Fleming and C.C. Grimes. Sliding-mode conductivity in nbse3: observation of a threshold electric field and conduction noise. *Physical Review Letters*, 42:1423, 1979.

[27] G. Grüner. Nonlinear conductivity and noise due to charge-density-wave depinning in $NbSe_3$. *Physical Review Letters*, 46:511, 1981.

[28] T.M. Tritt, D.J. Gillespie, A.C. Ehrlich, and G.X. Tessema. Charge-density-wave carrier concentration in $NbSe_3$ as a function of magnetic field and temperature. *Physical Review Letters*, 61:1776, 1988.

[29] N. Ru, C.L. Condron, G.Y. Margulis, K.Y. Shin, J. Laverock, S.B. Dugdale, M.F. Toney, and I.R. Fisher. Effect of chemical pressure on the charge density wave transition in rare-earth tritellurides RTe_3. *Physical Review B*, 77:035114, 2008.

[30] V. Brouet, W.L. Yang, X.J. Zhou, Z. Hussain, N. Ru, K.Y. Shin, I.R. Fisher, and Z.X. Shen. Fermi surface reconstruction in the CDW state of $CeTe_3$ observed by photoemission. *Physical Review Letters*, 93:126405, 2004.

[31] D.S. Inosov, V.B. Zabolotnyy, D.V. Evtushinsky, A.A. Kordyuk, B. Bchner, R. Follath, H. Berger, and S.V. Borisenko. Fermi surface nesting in several transition meatal dichalcogenides. *New J. Phys*, 10:125027, 2008.

[32] M.D Johannes, I.I. Mazin, and C.A. Howells. Fermi-surface nesting and the origin of the charge-density wave in $NbSe_2$. *Physical Review B*, 73:205102, 2006.

[33] M.D Johannes and I.I. Mazin. Fermi surface nesting and the origin of charge density waves in metals. *Physical Review B*, 77:165135, 2008.

[34] D.E. Moncton, J.D. Axe, and F.J. DiSalvo. Study of superlattice formation in 2H-$NbSe_2$ and 2H-$TaSe_2$ by neutron-scattering. *Physical Review Letters*, 34:734–737, 1975.

[35] X. Zhu, Y. Cao, J. Zhang, E.W. Plummer, and J. Guo. Proceedings of the national academy of sciences. *Proceedings of the National Academy of Sciences*, 112:2367–2371, 2015.

[36] T.M. Rice and G.K. Scott. New mechanism for a charge-density wave instability. *Physical Review Letters*, 35:120, 1975.

[37] J.A. Wilson. Charge-density wave in the 2H-$TaSe_2$ family: action on the Fermi surface. *Physical Review B*, 15:5748, 1977.

[38] N.J. Doran, G. Wexler, V. Heine, and B. Ricco. The origin of charge density waves in the 2H-polytypes of the group-v layer compounds. *Nuovo Cimento B*, 38:544–551, 1977.

[39] C.M. Varma and A.L. Simons. Strong-coupling theory of charge-density-wave transitions. *Physical Review Letters*, 51:138–141, 1983.

[40] H.P. Hughes. Structural distortion in tise2 and related materials a possible jahn-teller effect? *Journal of Physics C: Solid State Physics*, 10:L319, 1977.

[41] M. Calandra and F. Mauri. Charge-density wave and superconducting dome in $TiSe_2$ from electron-phonon interaction. *Physical Review Letters*, 106:196406, 2011.

[42] M.H. Whangbo and E. Canadell. Analogies between the concepts of molecular chemistry and solid-state physics concerning structural instabilities. electronic origin of the structural modulations in layered transition-metal dichalcogenides. *J. Am. Chem. Soc.*, 114:9587, 1992.

[43] J.A. Wilson. Concerning the semimetallic characters of TiS_2 and $TiSe_2$. *Solid State Commun*, 22:551, 1977.

[44] H. Cercellier, C. Monney, F. Clerc, C. Battaglia, L. Despont, M. G. Garnier, H. Beck, P. Aebi, L. Patthey, H. Berger, and L. Forro. Evidence for an excitonic insulator phase in 1T$TiSe_2$. *Physical Review Letters*, 99:146430, 2007.

[45] W.C. Tonjes, V.A. Greanya, R. Liu, C.G. Olson, and P. Molinie. Charge-density-wave mechanism in the 2H$NbSei_2$ family:angle-resolved photoemission studies. *Physical Review B*, 63:235101, 2001.

[46] J. van Wezel, P. Nahai-Williamson, and S.S. Saxena. Exciton-phonon interactions and superconductivity bordering charge order in $TiSe_2$. *Physical Review B*, 83:024502, 2011.

[47] A. Taraphder, S. Koley, N. S. Vidhyadhiraja, and M. S. Laad. Preformed excitonic liquid route to a charge density wave in 2H$TaSe_2$. *Physical Review Letters*, 106:236405, 2011.

[48] B. Zenker, H. Fehske, H. Beck, C. Monney, and A.R. Bishop. Chiral charge order in 1T-$TiSe_2$: Importance of lattice degrees of freedom. *Physical Review B*, 88:075138, 2013.

[49] J. He, K. Yang, J. Reppert, M. Skove, and A.M. Rao. Superconductivity in carbon nanotubes: Limitations, competition, and implementation toward higher Tc. In J. Haruyama, editor, *Carbon-based superconductors: Towards High-Tc Superconductivity*, pages 116–117. Pan Standford Publishing, 2014.

[50] B. Jamtveit and P. Meakin. *Growth, Dissolution and Pattern Formation in Geosystems*. Springer, 1999.

[51] M. Chhowalla, H.S. Shin, G. Eda, L.-J. Li, K.P. Loh, and H. Zhang. The chemistry of two-dimensional layered transition metal dichalcogenide nanosheets. *Nature Chemistry*, 5:263–275, 2013.

[52] Q.H. Wang, K. Kalantar-Zadeh, A. Kis, J.N. Coleman, and M.S. Strano. Electronics and optoelectronics of two-dimensional transition metal dichalcogenides. *Nature Nanotechnology*, 7:699–712, 2012.

[53] M. Kertesz and R. Hoffmann. Octahedral vs. trigonal-prismatic coordination and clustering in transition-metal dichalcogenides. *Journal of the American Chemical Society*, 106:3453–3460, 1984.

[54] R.H. Friend and D. Jerome. Pressure enhancement of charge densitywave formation in VSe2; The role of Coulomb correlations. *Solid State Communications*, 27:169–173, 1978.

[55] C. Gong, H. Zhang, W. Wang, L. Colombo, R.M. Wallace, and K. Cho. Band alignment of two-dimensional transition metal dichalcogenides: Application in tunnel field effect transistors. *Applied Physics Letters*, 103:053513, 2013.

[56] P.M. Williams. Phase transitions and charge density waves in the layered transition metal dichalcogenides. In F. Levy, editor, *Crystallography and crystal chemistry of materials with layered structures*, volume 2. Reidel, 1976.

[57] D.E. Moncton, F.J. DiSalvo, and S.C. Davey. X-ray-diffraction study of incommensurate charge-density waves in 1T-VSe_2. *Bulletin of the American Physical Society*, 24:446–446, 1979.

[58] K. Tsutsumi, T. Sambongi, A. Toriumi, and S. Tanaka. Incommensurate periodic lattice distortion perpendicular to the layer in 1T-VSe_2. *Journal of the Physical Society of Japan*, 49:837–838, 1980.

[59] K. Tsutsumi. X-ray-diffraction study of the periodic lattice distortion associated with a charge-density wave in 1T-VSe_2. *Physical Review B*, 26:5756–5759, 1982.

[60] V.N. Strocov, M. Shi, M. Kobayashi, C. Monney, X. Wang, and J. Krempasky. Three-dimensional electron realm in VSe_2 by soft-X-ray photoelectron spectroscopy: origin of charge-density waves. *Physical Review Letters*, 109:086401, 2012.

[61] F. J. DiSalvo and J. V. Waszczak. Magnetic studies of VSe_2. *Physical Review B*, 23:457–461, 1981.

[62] D.J. Eaglesham, R.L. Withers, and D.M. Bird. Charge-density-wave transitions in 1T-VSe_2. *Journal of Physics C: Solid State Physics*, 19:359, 1986.

[63] B. Giambattista, C.G. Slough, W.W. McNairy, and R.V. Coleman. Scanning tunneling microscopy of atoms and charge-density waves in 1T-TaS_2, 1T-$TaSe_2$, and 1T-VSe_2. *Physical Review B*, 41:10082–10103, 1990.

[64] A.H. Thompson and B.G. Sibernagel. Correlated magnetic and transport properties in the charge-density-wave states of VSe_2. *Physical Review B*, 19:3420–3426, 1979.

[65] T. Tsuda, Y. Kitaoka, and H. Yasuoka. NMR strudies of the CDW state in 1T-VSe_2. *Physica*, 105B:414–418, 1981.

[66] A.M. Woolley and G. Wexler. Band structures and fermi surfaces for 1T-TaS_2, 1T-$TaSe_2$ and 1T-VSe_2. *Journal of Physics C: Solid State Physics*, 10:2601–2616, 1977.

[67] C. Monney, E.F. Schwier, M.G. Garnier, N. Mariotti, C. Didiot, H. Cercellier, J. Marcus, H. Berger, A.N. Titov, H. Beck, and .P Aebi. Probing the exciton condensate phase in 1T-$TiSe_2$ with photoemission. *New Journal of Physics*, 12:125019, 2010.

[68] K. Terashima, T. Sato, H. Komatsu, and T. Takahashi. Charge-density wave transition of 1T-VSe_2 studied by angle-resolved photoemission spectroscopy. *Physical Review B*, 68:155108, 2003.

[69] Y. Yoshida and K. Motizuki. Electron-lattice interactions and lattice instabilities of 1T-VSe_2, 1T-$CrSe_2$ and 1T-TiS_2. *Journal of the Physical Society of Japan*, 51:2107–2115, 1982.

[70] P. Giannozzi, S. Baroni, N. Bonini, M. Calandra, R. Car, C. Cavazzoni, D. Ceresoli, G.L. Chiarotti, M. Cococcioni, I. Dabo, A. Dal Corso, S. de Gironcoli, S. Fabris, G. Fratesi, R. Gebauer, U. Gerstmann, C. Gougoussis, A. Kokalj, M. Lazzeri, L. Martin-Samos, N. Marzari, F. Mauri, R. Mazzarello, S.Paolini, A. Pasquarello, L. Paulatto, C. Sbraccia, S. Scandolo, G. Sclauzero, A.P. Seitsonen, A. Smogunov, P. Umari, and R.M Wentzcovitch. QUANTUM ESPRESSO: a modular and open-source software project for quantum simulations of materials. *Journal of Physics: Condensed Matter*, 21:395502, 2009.

[71] J.P. Perdew, K. Burke, and M. Ernzerhof. Generalized gradient approximation made simple. *Physical Review Letters*, 77:3865–3868, 1996.

[72] T. Bucko, J. Hafner, S. Lebegue, and J.G. Angyan. Improved description of the structure of molecular and layered crystals: Ab initio DFT calculations with van der Waals corrections. *The Journal of Physical Chemistry A*, 114:11814–11824, 2010.

[73] M. Methfessel and A.T. Paxton. High-precision sampling for Brillouin-zone integration in metals. *Physical Review B*, 40:3616–3621, 1989.

[74] H.J. Monkhorst and J.D. Pack. Special points for Brillonin-zone integrations. *Physical Reveiw B*, 13:5188–5192, 1976.

[75] C.M. Fang, C.F. van Bruggen, R.A. Bruggen, R.A. de Groot, G.A. Wiegers, and C. Haas. The electronic structure of the metastable layer compound 1T-$CrSe_2$. *Journal of Physics: Condensed Matter*, 9:10173–10184, 1997.

[76] A.A. Mostofi, J.R. Yates, Y.-S. Lee, I. Souza, D. Vanderbilt, and N. Mazari. Wannier90: a tool for obtaining maximally-localised Wannier functions. *Computer Physics Communications*, 178:685–699, 2008.

[77] S. Baroni, S. de Gironcoli, A. Dal Corso, and P. Giannozzi. Phonons and related crystal properties from density-functional perturbation theory. *Reviews of Modern Physics*, 73:515–562, 2001.

[78] A.L. Pope, R.T. Littleton IV, and Terry M. Tritt. Apparatus for the rapid measurement of electrical transport properties for both needle-like and bulk materials. *Review of Scientific Instruments*, 72:3129–3131, 2001.

[79] S. Piscanec, M. Lazzeri, F. Mauri, A.C. Ferrari, and J. Robertson. Description of the parallel thermal conductance technique for the measurement of the thermal conductivity of small diameter samples. *Physical Review Letters*, 93:185503, 2004.

[80] C.S. Yadav and A.K. Rastogi. Electronic transport and specific heat of 1T-VSe_2. *Solid State Communications*, 150:648–651, 2010.

[81] A.L. Pope, B. Zawilski, and T.M. Tritt. Description of removable sample mount apparatus for rapid thermal conductivity measurements. *Cryogenics*, 41:725–731, 2001.

[82] G.M. Sheldrick. A short history of SHELX. *Acta Crystallographica*, A64:112–122, 2008.

[83] F.J. DiSalvo and J.V. Waszczak. The effect of fe substitution on the charge density wave in VSe_2. *Journal De Physique*, 37:C4–157, 1976.

[84] M. Sarma, A. Ghorayeb, S. Nulsen, and R.H. Friend. Transport properties of VSe_2 intercalated with hydrazine. *Journal of Physics C: Solid State Physics*, 14:L1055–L1060, 1981.

[85] C.S.Yadav and A.K. Rastogi. Transport and magnetic properties of Fe_xVSe_2(x=0-0.33). *Journal of Physics: Condensed Matter*, 20:465219, 2008.

[86] M Bayard and M.J. Sienko. Anomalous electrical and magnetic properties of vanadium diselenide. *Journal of Solid State Chemistry*, 19:325–329, 1976.

[87] C.F. van Bruggen and C. Haas. Magnetic susceptibility and electrical properties of VSe_2 single crystals. *Solid State Communications*, 20:251–254, 1976.

[88] H.Mutka and P. Molinie. Irradiation-induced defects in layered dichalcogenides: the case of VSe_2. *Journal of Physics C: Solid State Physics*, 15:6305–6319, 1982.

[89] H.M. Rietveld. A profile refinement method for nuclear and magnetic structures. *Journal of Applied Crystallography*, 2:65–71, 1969.

[90] A.C. Larson and R.B. Von Dreele. General structure analysis system (GSAS). *Los Ala National Laboratory Report LAUR*, 86-748, 2000.

[91] B.H. Toby. EXPGUI, a graphical user interface for GSAS. *Journal of Applied Crystallography*, 34:210–213, 2001.

[92] B.H. Toby. R factors in Rietveld analysis: How good is good enough? *Powder Diffraction*, 21:67–70, 2006.

[93] J.A.R. Stiles, D.Ll Williams, and M.J. Zuckermann. Dependence of the critical temperature for the formation of charge density waves in 2hnbse2 upon impurity concentration. *Journal of Physics C: Solid State Physics*, 9:L489–L493, 1976.

[94] C.S.Yadav and A.K. Rastogi. Transport and magnetic properties of $Fe_{1/3}VSe_2$. *Journal of Physics:Condensed Matter*, 20:415212, 2008.

[95] C. Kittel. *Introduction to Solid State Physics*. John Wiley and Sons, 2004.

[96] J.H. Becker and H.P.R. Frederikse. Electrical properties of nonstoichiometric semiconductors. *Journal of Applied Physics*, 33:447, 1962.

[97] H. Putley. *The Hall Effect and Semi-Conductor Physics*. Dover Publications Inc., 1968.

[98] H. Ibach and H. Luth. *Solid-State Physics: an Introduction to Principles of materials Science*. Springer, 2009.

[99] H. Ibach and H. Luth. *Semiconductor Optoelectronic Devices*. Prentice Hall, 1997.

[100] T.R. Chien, Z.Z. Wang, and N.P. Ong. Effect of Zn impurities on the normal-state Hall angle in single-crystal $YBa_2Cu_{3-x}Zn_xO_{7-\delta}$. *Physical Review Letters*, 67:2088–2091, 1991.

[101] P.W. Anderson. Hall effect in the two-dimensional Luttinger liquid. *Physical Review Letters*, 67:2092–2094, 1991.

[102] A. Carrington, A.P. Mackenzie, C.T. Lin, and J.R. Cooper. Temperature dependence of the hall angle in single-crystal $YBa_2(Cu_{1-x}Co_x)_3O_{3-x}$. *Physical Review Letters*, 69:2855–2858, 1992.

[103] Y. Ma, Y. Dai, M. Guo, C. Niu, Y. Zhu, and B. Huang. Evidence of the existence of magnetism in pristine VX_2 monolayers (X=S,Se) and their strain-induced tunable magnetic properites. *ACS Nano*, 6:1695–1701, 2012.

[104] F. Li, K. Tu, and Z. Chen. Versatile electronic properties of VSe_2 bulk, few-layers, monolayere, nanoribbons and nanotubes: a computational exploration. *The Journal of Physical Chemistry*, 21264:21264–21274, 2014.

[105] K. Xu, P. Chen, X. Li, C. Wu, Y. Guo, J. Zhao, X. Wu, and Y. Xie. Ultrathin nanosheets of vanadium diselenide: a metallic two-dimensional material with ferromagnetic charge-density-wave behavior. *Angewandte Chemie International Edition*, 52:10477–10481, 2013.

[106] L.F. Schneemeyer, A. Stacy, and M.J. Sienko. Effect of nonstoichiometry on the periodic lattice distortion in vanadium diselenide. *Inorganic Chemistry*, 19:2659–2662, 1980.

[107] G. Gruner, A. Zawadowski, and P.M. Chaikin. The role of exchange interaction in paramagnetic absorption. *Physical Review*, 72:1128–1129, 1947.

[108] L.F. Schneemeyer. *The effect of niobium substitution on charge density wave anomalies in vanadium diselenide*. PhD thesis, Cornell University, Ithaca, 1978.

[109] R.W. Hill, C. Proust, L. Taillefer, P. Fournier, and R.L. Greene. Breakdown of fermi-liquid theory in a copper-oxide superconductor. *Nature*, 414:711, 2001.

[110] N.P. Ong and P. Monceau. Anomalous transport properties of a linear-chain metal: $NbSe_3$. *Physical Review B*, 16:3443, 1977.

[111] H.N.S. Lee, M. Garcia, H. McKinzie, and A. Wold. The low-tempereatue electrical and magnetic properties of $TaSe_2$ and $NbSe_2$. *Journal of Solid State Chemistry*, 1:190–194, 1970.

[112] M. Jamei. *Electronic Properties of Low-Dimensional Materials Under Periodic Potential*. PhD thesis, University of California, Berkeley, 2015.

[113] I. Naik and A.K. Rastogi. Charge density wave and superconductivity in 2H- and 4H-$NbSe_2$: a revisit. *Pramana-journal of physics*, 76:957–963, 2011.

[114] T. Tani and S. Tanaka. Thermoelectric power observation of nearly-commensurate charge-density wave phase in 1T-TaS_2. *Journal of the Physical Society of Japan*, 53:1790–1796, 1984.

[115] P.M. Chaikin, W.W. Fuller, and R. Lacoe. Thermopower of doped and damaged $NbSe_3$. *Solid State Communications*, 39:553–557, 1981.

[116] N.P. Ong and P. Monceau. Hall effect of a linear-chain metal: $NbSe_3$. *Solid State Communication*, 26:487–491, 1978.

[117] J.M.E. Harper, T.H. Geballe, and F.J. DiSalvo. Thermal properties of layered tarnsition-metal dichacogenides at charge-density-wave transition. *Physical Review B*, 15:2943–2951, 1977.

[118] J. Chaussy, P. Haen, J.C. Lasjaunias, P. Monceau, and G. Waysand. Phase transitions in $NbSe_3$. *Solid State Communications*, 20:759–763, 1976.

[119] R.S. Kwok and S.E. Brown. Thermal conductivity of the charge-density-wave systems $K_{0.3}MoO_3$ and $(TaSe_4)_2I$ near the Peierls transition. *Physical Review Letters*, 63:895–898, 1989.

[120] A. Smontara and K. Biljakovic. Contribution of charge-density-wave phase exitations to thermal conductivity below the Peierls transition. *Physical Review B*, 48:4329, 1993.

[121] C.S. Lue, Y.-K. Kuo, F.H. Hsu, H.H. Li, H.D. Yang, P.S. Fodor, and L. E. Wenger. Thermal hysteresis in the charge-density-wave transition of $Lu_5Rh_4Si_{10}$. *Cryogenics*, 41:725–731, 2001.

[122] H.M. Rosen. *Low temperature solid state physics: some selected topics.* Oxford University Press, 1963.

[123] H. Ando, T. Yokoya, K. Ishizaka, S. Tsuda, T. Kiss, S. Shin, T. Eguchi, M. Nohara, and H. Takagj. Observation of nuclear specific heat in V_2O_3. *Physical Review B*, 2:3768–3771, 1970.

[124] D.B. McWhan and J.P. Remeika. Heat capacity of metallic V_2O_3 at high pressure. *Physical Review B*, 7:3079–3083, 1973.

[125] L.E. Wenger and P.H. Keesom. Low temperature specific heat of $(V_{1-x}Cr_x)_2O_3$ and $(V_{1-x}Al_x)_2O_3$. *Physical Review B*, 12:5288–5296, 1975.

[126] H. Yasuoka, H. Nishihara, and Y. Nakamura. Observation of ^{15}V NMR in antiferromagnetic state of V_2O_3. *Physics Letters A*, 37:299–300, 1971.

[127] H. von Lohneysen. Non-Fermi-lilquid behaviour in the heavy-fermion system $CeCu_{6-x}Au_x$. *Journal of Physics: Condensed Matter*, 8:9689–9706, 1996.

[128] T. Tolinski, A. Kowalczyk, A. Szewczyk, and M. Gutowska. Specific heat in $CeNi_4Cu$ and $YbNi_4Cu$. *Jouranl of Physics: Condensed Matter*, 18:3435–3441, 2006.

[129] G.H. Wannier. Antiferromagnetism. the triangular Ising net. *Physical Review*, 79:357–364, 1950.

[130] S. Yamashita, T. Yamamoto, Y. Nakazawa, M. Tamura, and R. Kato. Gapless spin liquid of an organic triangular compound evidenced by thermodynamic measurements. *Nature Communications*, 2:275, 2011.

[131] S. Nakatsuji, Y. Nambu, H. Tonomura, O. Sakai, S. Jonas, C. Broholm, H. Tsunetsugu, Y. Qiu, and Y. Maeno. Spin disorder on a triangular lattice. *Science*, 309:1697–1700, 2005.

[132] U. Chatterjee, J. Zhao, M. Lavarone, R. Di Capua, J.P. Castellan, G. Karapetrov, C.D. Malliakas, M.G. Kanatzidis, H. Claus, J.P.C. Ruff, F. Weber, J. van Wezel, J.C. Campuzano, R. Osborn, M. Randeria, N. Trivedi, M.R. Norman, and S. Rosenkranz. Emergence of coherence in the charge-density-wave state of 2H-$NbSe_2$. *Nature Communications*, 6:6313, 2015.

[133] A. Fang, N. Ru, I.R. Fisher, and A. Kapitulnik. STM studies of $TbTe_3$: Evidence for a fully incommensurate charge density wave. *Physical Review Letters*, 99:046401, 2007.

[134] E. DiMasi, M.C. Aronson, J.F. Mansfield, B. Foran, and S. Lee. Chemical pressure and charge-density waves in rare-earth tritellurides. *Physical Review B*, 52:14516, 1995.

[135] F. Schmitt, P.S. Kirchmann, U. Bovensiepen, R.G. Moore, J.-H. Chu, D.H. Lu, L. Rettig, M. Wold, I.R. Fisher, and Z.-X. Shen. Ultrafast electron dynamics in the charge density wave material $TbTe_3$. *New Journal of Physics*, 13:063022, 2011.

[136] P.M. Chaikin. An introduction to thrmopower for those who might want to use it to study organic conductors and superconductors. In V.Z. Kresin and W.A. Little, editors, *Organic Superconductivity*. Plenum Press, 1990.

[137] N.F. Mott. Conduction in non-crystalline materials. *Philosophical Magazine*, 19:835–852, 1969.

[138] M. J. Burns and P.M. Chaikin. Interaction effects and thermopower in low temperature hopping. *Journal of Physics C: Solid State Physics*, 18:L743–L749, 1985.

[139] A. Shakouri. Recent developments in semiconductor thermoelectric physics and materials. *Annual Review of Materials Research*, 41:399–431, 2011.

[140] N.F. Mott and E.A. Davis. *Electronic Processes in Non-crystalline Materials*. Oxford University Press, 2012.

[141] M. Cutler and N.F. Mott. Observation of Anderson localization in an electron gas. *Physical Review*, 181:1336, 1969.

[142] M. Jonson and G.D. Mahan. Mott's formula for the thermopower and the wiedemann-franz law. *Physical Review B*, 21:4223, 1980.

[143] Z.M. Gibbs, H.S. Kim, H. Wang, and G.F. Snyder. Band gap estimation from temperature dependent Seebeck measurement deviations from the $2eS_{max}T_{max}$ relation. *Applied Physics Letters*, 106:022112, 2015.

[144] A.F. Ioffe. *Physics of Semiconductors*. Academic Press, 1960.

[145] H.J. Goldsmid and J.W. Sharp. Estimation of the thermal band gap of a semiconductor from seebeck measurements. *Journal of Electronic Materials*, 28:869–872, 1999.

[146] A. Tari. *The specific heat of matter at low tempratures*. Imperial College Press, 2003.

[147] K.P. Belov, T.V. Valyanskaya, L.G. Mamsurova, and V.I. Sokolov. Specific heat of the antiferromagnetic garnet $Ca_3Mn_2Ge_3O_{12}$. *Soviet Physics-Journal of Experimental and Theoretical Physics*, 38:561, 1974.

[148] R.A. Fisher, P. Radhakrishna, N.E. Phillips, J.V. Badding, and A.M. Stacy. Low-temperature specific heat of antiferromagnetic $EuNi_5P_3$ and mixed-valent $EuNi_2P_2$ in magnetic fields to 7T. *Physical Review B*, 52:13519, 1995.